Quantum Illumination with Gaussian States and Detection

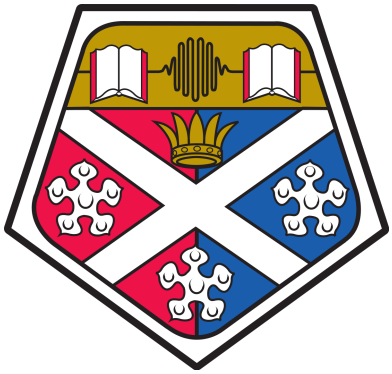

Hao Yang

CNQO, Department of Physics

University of Strathclyde

A thesis submitted for the degree of

Doctor of Philosophy

Submission Year: 2023

Abstract

Quantum illumination is a technique that uses quantum states of radiation, often quantum entangled states, for object detection. Potential applications are in the development of quantum radar or quantum rangefinding devices. This thesis investigates quantum illumination theory with photodetection. Inclusion of detection, by first measuring the idler radiation mode that is entangled with another signal radiation mode, can condition the remaining signal mode into a nonclassical radiation state with a gain in signal energy. This can leads to results showing quantum signals increasing the likelihood of successful detection events of target-reflected signals, even in situations with low signal energy and a noisy background, compared to coherent state signals. The analysis uses the Gaussian quantum information framework, which models the statistical properties of the radiation states as Gaussian distributions in quantum phase space.

Optimal measurement of object-reflected signals is presented via state discrimination theory, show that the entangled two-mode squeezed vacuum state is most effective at reducing the discrimination error between the reflected signal-plus-background noise vs. background noise alone, compared to using a classical coherent signal of the same energy or against all single-mode Gaussian states. But with a detection limited, sub-optimal measurement analysis of quantum illumination, there are certain regimes where a coherent state can outperform a two-mode squeezed vacuum in terms of raising signal detection probability. Finally, sequential detection results comparing performance of classical vs. quantum illumination were modelled by Monte Carlo simulations, in order to show estimated object presence or absence using conditional detection probabilities and Bayes' theorem.

Quantum Illumination with Gaussian States and Detection

Hao Yang

CNQO, Department of Physics

Faculty of Science

University of Strathclyde

Glasgow, Scotland, United Kingdom

A thesis submitted for the degree of

Doctor of Philosophy

Submission Year: 2023

First Supervisor: Prof. John Jeffers

Second Supervisor: Dr. Jonathan Pritchard

Declaration

This thesis is the result of the author's original research. It has been composed by the author and has not been previously submitted for examination which has led to the award of a degree.

SIGNED: HAO YANG

DATE: 14th November 2023

List of Publications

The following papers were published during the period of study:

- Hao Yang, W. Roga, J. D. Pritchard, and J. Jeffers "Quantum illumination with simple detection", Proc. SPIE 11347, Quantum Technologies 2020, 113470I (2020).

- Hao Yang, W. Roga, J. D. Pritchard, and J. Jeffers, "Gaussian state-based quantum illumination with simple photodetection", Opt. Express 29, 8199-8215 (2021).

- Hao Yang, N. Samantaray, and J. Jeffers, "Quantum illumination with multiplexed photodetection", Phys. Rev. Applied 18, 034021 (2022).

Acknowledgements

It took me a while, around a year or so, from the end of my viva to the formal submission of this thesis with corrections (which I shall perform shortly). Despite this delay, it formed essentially a period of detachment in which I have had the time to reflect, digest, get healthy, work, earn money and enjoy life outside the rather gloomy and post-modern maze of academic thinking. So that, after many moons later, when I blow the dust off a printed version of this thesis, and read these rewritten acknowledgements, I might feel a bittersweet fondness, alongside reassuring pride and comforting *warmth* from the aftermath of what was (and I might be a bit dramatic here ...) undoubtedly the greatest trial and tribulation of my young-adult epoch.

A clichéd broadstroke, but ups and downs certainly have occurred, plus a pandemic tacked onto the end of it too. During the PhD I was a fat, confused, depressed chain-smoker (with blonde hair at one point) nomadically residing in various sandstone tenements of Glasgow. Too self-conscious and distracted, I didn't know what to do with myself, and only had a passing fancy for physics, to which, I still consider myself a "dilettante" to this day. So, sorry to inform you, dear reader, that no new discoveries or revelations are present in this thesis – it's more an in-depth mishmash of the different branches of quantum physics, a branch-gathering, if you like. It's am attempt to squeeze something useful in the form of an applied theory for something called a "quantum radar".

It's not all zero-sum though: I'm very, very, extremely, *immensely* grateful for my PhD experience at Strathclyde; to QinetiQ and Quantic for their sponsorship as well. I want to thank my supervisors John and Jon, for onboarding me into this journey, and for your contrasting levels of dialectical verbosity. I want to thank

Daniel, Bill, Wojciech, and Nigam for your helpful inputs and contributions along the way. I also want to thank Alison for your reassuring light-heartedness about it all. I want to thank my fellow PhD comrades (no namelist here because I don't wanna play favourites, you are all despised equally!) Jokes aside, I really will miss our coffee break discussions in the level 7 fishbowl – in that purgatorial makeshift oblong we surveyed the expanses beyond physics and science, trekked often into the hinterlands of culture, language and politics. They were humorous, heated but overall very edifying. And lastly, I want to issue an apology to you all for my chaotic behaviour and nonsensical drivel I might have spoken at times.

Thank you, dad and granny. Thank you, Anita, for the pep talks. Thank you mum. I'm happy you're all in my life.

And thank you grandad – you would have *loved* seeing the back of this thesis as much as I did.

Hao Yang

Falkirk, 2023

Oh, what does science not
conceal today! how much, at
any rate, is it *meant* to conceal!

Nietzsche

Contents

1 Introduction **1**

1.1 Entanglement, Quantum Radar & Lidar 3

1.2 Current & Future Perspectives 7

1.3 Basic Theoretical Methods 11

1.4 Thesis Layout 14

2 Gaussian States & Phase Space Quantum Optics **16**

2.1 Brief Classical vs. Quantum Theory 18

2.1.1 Maxwell's Equations 18

2.1.2 Quantum Harmonic Oscillator 19

2.2 Gaussian States 25

2.2.1 Thermal States 25

2.2.2 Coherent States 27

2.2.3 Single-Mode Squeezed Vacuum 30

2.2.4 Two-Mode Squeezed Vacuum 33

2.3 Phase Space Quantum Optics 34

2.3.1 Characteristic & Wigner Functions 34

2.3.2 Mean Vector & Covariance Matrix 38

2.3.3 Moments of Gaussian States 40

2.3.4 Symplectic Transforms 45

2.4 Discussion 49

3 Quantum State Discrimination **51**

3.1 The Helstrom Bound 53

3.2 Overlap-Based Error Bounds . . . 57
3.2.1 Fidelity . . . 57
3.2.2 Quantum Chernoff Bound . . . 58
3.2.3 Gaussian State Expressions . . . 60
3.3 Multicopy State Discrimination . . . 62
3.4 Discussion . . . 63

4 Quantum State Measurement **65**
4.1 Photocounting . . . 67
4.2 On-Off Detection . . . 68
4.2.1 One Detector . . . 68
4.2.2 Multiple Detectors . . . 72
4.3 Measurement-Based State Engineering . . . 74
4.3.1 One Detector . . . 76
4.3.2 Multiple Detectors . . . 79
4.4 Discussion . . . 83

5 Quantum Illumination & Detection **85**
5.1 Gaussian State Quantum Illumination . . . 89
5.1.1 Single-Mode Signals . . . 89
5.1.2 Two-Mode Signals . . . 91
5.2 Quantum Illumination & Detection . . . 96
5.2.1 Conditional Probabilities of On-Off Detection . . . 96
5.2.2 Receiving Detector Probabilities . . . 97
5.2.3 Results . . . 100
5.3 Simulation of Sequential Detection . . . 106
5.3.1 Main Method . . . 106
5.3.2 Simulating Detector Clicks . . . 108
5.3.3 Results . . . 110
5.4 Discussion . . . 114

Conclusion **117**

Bibliography **118**

Chapter 1

Introduction

Illumination is an ubiquitous effect. Crucial for visual perception, our surroundings are being illuminated constantly, by ambient light sources or artificial ones. To reduce this down to a fundamental level, it is the interactions between electromagnetic (EM) radiation and atoms which facilitate this process. The atom scatters incident radiation, then the detection of such radiation allow us to deduce information about the scattering object. Our eyes and brain do this all the time. Visual information is particularly useful because it provides a lot of information quickly in order to convey a multitude of ideas, after all a picture is worth a thousand words. But our eyes are only sensitive to the visible spectrum at best and is a rather narrow region of the EM spectrum, so we need technology to illuminate things using other wavelengths. Illumination and detection at wavelengths other than the visible gives us an extra degree of freedom when trying to view distant objects.

In different situations we might require different amounts of detail; sometimes simply noticing a target is sufficient. The RADAR (RAdio Detection And Ranging) is an example of technology that uses target illumination. Its working principle requires bouncing transmitted radiation off a target, in order to notice it and determine its range r. The range is measured by detection of back-scattered radiation. As the speed of EM radiation c, in air, is an approximate constant,

the target range from the transmitter is simply

$$r = \frac{ct}{2}, \tag{1.1}$$

where t is the signal round-trip time, which has travelled twice the distance between transmitter and target. One can also measure the radial velocity v thanks to the Doppler-effect

$$v = \frac{c\Delta f}{2f}, \tag{1.2}$$

whereby Δf is the Doppler-shifted transmitted frequency f [1]. Range and radial velocity are the predominant pieces of information that a radar finds out about a target. Typically, conventional radars make use of frequencies lower than the visible spectrum, which is on the order of 10^2 THz, from radio waves to microwaves from ∼5 MHz – 130 GHz. A few examples of radar applications are in navigation, missile defence systems, weather forecasting, airport traffic control and astronomy [1]. Selection of the transmitted frequency must take into consideration the physical size of the target and desired resolution, so that only the target interacts and scatters the radiation, not other unwanted sources, thus giving radar the unique capability to "see through" obstructions.

With the advent of lasers, coherent radiation from the optical spectrum has became a viable tool for precision ranging and detection. This type of "radar" is known as LIDAR, an acronym of LIght Detection And Ranging. Laser radiation is highly directional and easily scattered, and more suited for high-resolution scanning operations such as geophysical surveying and 3D precision mapping. However as most solid objects can scatter optical radiation, lidars lack the capability to "see through" objects compared to radars.

Radar and lidar rely on the same process of illumination and detection of backscattered signal, using different parts of the EM spectrum. Without measurement of this backscatter, the target cannot be detected – such is the justification of stealth technology. For example, if a "sentient" target wishes to remain hidden, and is aware that it is being monitored (by scanning for radar-transmitted radiation) it can then deflect, disrupt, or spoof the radar signal as a countermeasure. Covert operation with radars, then, would be beneficial against such counter-

measures: by severely decreasing the power of the transmitted signal, so much so that it hides within the environmental thermal noise, unnoticeable to the target. Under such a very low power constraint, especially in the region of single to a few photons, it would be interesting to investigate and take into consideration certain quantum effects and look for potential benefits.

1.1 Entanglement, Quantum Radar & Lidar

Entanglement is a non-local quantum effect that has gathered interest for its potential application in enhancing the sensitivity of photodetection [2, 3]. In the broadest sense, bipartite entanglement indicates that there are stronger-than-classical correlations between two spatially separated physical systems [4]. If a system A is in a particular state denoted as $\hat{\rho}_A$, along with system B that is in a state $\hat{\rho}_B$, then the joint "global" state is $\hat{\rho}_{A,B}$ – the global state is considered entangled if it *cannot* be written as the following

$$\hat{\rho}_{A,B} = \hat{\rho}_A \otimes \hat{\rho}_B. \tag{1.3}$$

whereby $\otimes$ denotes the tensor product of both states [5]. If the above factorisation *is* possible, then the state $\hat{\rho}_{A,B}$ is *not entangled* and is deemed *separable*. An entangled state therefore must be described as a whole, and this, entanglement is a strictly quantum phenomenon that violates local realism. During the development of quantum theory, Einstein, Podolsky and Rosen [6] thought it was incomplete due to such non-local behaviour. Information could thus be transmitted faster-than-light via such "spooky action at a distance" between entangled systems. Attempts at resolving this paradox suggested that extra dependencies in the form of "hidden variables" that underpin entanglement, however Bell's proof showed that no such hidden-variable can exist [7]. It is now widely accepted that entanglement is a characteristic trait of quantum mechanics and it is necessary for algorithms in quantum computation such as superdense coding [8, 9] or quantum teleportation [10–14]. Quantum computation models commonly employ spin 1/2 particles as a physical resource.

Entangled radiation states such as entangled photons, are routinely produced in experiments in both optical [11, 15–18] and microwave [19–21] frequencies. This is normally achieved through spontaneous parametric down-conversion (SPDC). In the down-conversion process, a single "pump" photon of frequency ω_P is split into two daughter photons of a lower frequency ω_I and ω_S, knowns as "idler" and "signal", as it passed through a nonlinear medium. Energy conservation is obeyed by this process, which means

$$\omega_P = \omega_I + \omega_S, \tag{1.4}$$

and that the fields are phase-matched

$$k_P = k_I + k_S, \tag{1.5}$$

with k as the wave-vector of the fields involved in the down-conversion process (momentum conservation). Despite being separated spatially, output signal and idler photons can be highly-correlated in terms of frequency, intensity or polarisation [22–24]. Strong correlations from entangled photons would then enhance detection signal-to-noise ratio (SNR) in radar at low signal intensities. For example, the entangled signal can hide within the thermal background noise, unnoticeable by the target. The reflected signal would therefore contain residual correlations along with the idler photon that can be revealed through a coincidence-type detection at the transmitter – the sensitivity of a radar which uses entangled radiation would then be improved for low power operation [3, 25–27].

Illumination with quantum light, a.k.a "quantum illumination" theory was suggested for enhancing the sensitivity of photodetection. Based on Sacchi's work on optimal discrimination of quantum operations [28], Lloyd [2] compared the performance of repeatedly sending single photons vs. entangled photon pairs. The performance is evaluated using the asymptotic error probability limit under a large number of measurements, M. Overall, the model assumed that the number of distinguishable modes in the detector, d, is very large such that the number of background noise photon per mode b, is low ($db \ll 1$), so that the detector can detect at most, one noise photon per shot. In a regime where $\kappa/b > 1$, meaning

that the detected photon is more likely to be a signal photon (κ being the object reflectivity), both single and entangled photons produce the same asymptotic error bound [29]

$$p_e = \frac{1}{2}e^{-M\kappa}, \tag{1.6}$$

which is the approximation on the absolute probability of error given a large number of measurements

But for a considered "worse" scenario where $\kappa/b < 1$, the detected photon is more likely to be a noise photon: the error bound for a single photon is

$$p_e = \frac{1}{2}e^{-M\kappa^2/8b}, \tag{1.7}$$

compared to the entangled photon signal

$$p_e = \frac{1}{2}e^{-M\kappa^2 d/8b}, \tag{1.8}$$

that shows a larger reduction for $d \gg 1$. The detector is therefore less error-prone when measuring entangled photons, which implies that quantum illumination can notice low-reflective targets quicker by reducing the number of measurements by a factor of d, because the entangled idler photon (that does not interact with the target) helps reduce the effective noise from b to b/d: the idler acts as a sort of "signature" which helps pick out the signal photon [29].

Subsequent theory papers have followed this technique of comparing unentangled vs. entangled signals then minimizing the probability of error, but trying signal states with different photon statistics. Tan *et al.* investigated quantum illumination with multi-photon signals known as "Gaussian states" [30]. This work compared performance between that of a coherent state (unentangled) vs. two-mode squeezed vacuum (entangled). Analysis with Gaussian states is easier as they can be parameterised in terms of a mean photon number, $\bar{n}_s$. The coherent state probability error was found to be

$$p_e = \frac{1}{2}e^{-M\kappa\bar{n}_s(\sqrt{\bar{n}_b+1}-\sqrt{\bar{n}_b})^2}, \tag{1.9}$$

which for low background noise photon number is

$$p_e \approx \frac{1}{2}e^{-M\kappa\bar{n}_s}. \tag{1.10}$$

When $\bar{n}_s = 1$, this equals the single photon result in eq. (1.6), which is a lower error probability compared to using photon pairs in the worse regime given in eq. (1.8): classical illumination with coherent states therefore works *better* than quantum illumination in a regime with low background noise! This result was later addressed by Shapiro & Lloyd [31]. However, in the case of high noise scenarios ($\bar{n}_b \gg 1$), the coherent state bound is

$$p_e \approx \frac{1}{2} e^{-M\kappa\bar{n}_s/4\bar{n}_b}, \tag{1.11}$$

comparing with the entangled two-mode squeezed vacuum, the error bound is

$$p_e \approx \frac{1}{2} e^{-M\kappa\bar{n}_s/\bar{n}_b}, \tag{1.12}$$

in which the error exponent is improved by a factor of 4 (6 dB reduction in error). This result helped identified, in a more generalised perspective, the regime where quantum illumination using entangled states would perform better than classical illumination: high background noise, low target reflectivity and low signal energy.

To reach the theoretical and optimal results of quantum illumination is experimentally challenging, as such error bounds that characterise performance do not inform of a measurement process. Guha & Erkmen have proposed two different methods which require additional optical parametric amplification (OPA receiver) of the return signal, that can achieve a 3 dB advantage, because amplification of a quantum signal mixes in additional noise [32]. Zhuang *et al.* have proposed an even more complex method of feed-forward sum-frequency-generation receiver (FF-SHG receiver), which uses sum-frequency generation to perform the inverse of SPDC in order to reconstruct entirely the M-number of pulses that has interacted with target [33]. This detector in theory would achieve the 6 dB error reduction advantage calculated in ref. [30]. Optimal discrimination demands that the idler and return signal states are measured simultaneously, which is a very demanding task. A method to do this is via optical fibres, however inevitable losses in the optical fibre would deteriorate the signal and ultimately limit the range of the quantum radar. In Barzanjeh *et al.* [34] the authors give an example that under 0.2 dB/km losses, the range of the quantum radar would be limited to 11km under perfect ranging conditions.

1.2 Current & Future Perspectives

The theory highlighted in the previous section provides the motivation for further investigation into quantum radar & lidar: the signal can hide within the background noise. The concealed signal cannot be noticed by the target, and only the sender is able to distinguish the return signal from the background because the sender has extra information from the entangled idler photon. For a simple example, assume that the environmental noise is radiated by a black-body. The mean photon number of this noise is modelled by a Bose-Einstein distribution [35]

$$\bar{n}_b = \left(e^{\frac{\hbar\omega}{k_B T}} - 1\right)^{-1}, \tag{1.13}$$

with ω as the angular frequency, T the absolute temperature, $\hbar$ and k_B are the reduced Planck's constant and Boltzmann constant. The number of background photons plays a key factor in how distinguishable the return signal is. If it is low, such as in the optical frequencies, then by the results in ref. [31] classical illumination using the coherent state is the optimal choice for ranging and detection. Quantum illumination is potentially useful for infrared lidar to GHz radar operation because background noise is within the regimes calculated from previous works, i.e. in ref. [30], $\bar{n}_b = 20$ corresponds to approximately 300 GHz at 10°C.

A renewed interest in quantum radar was sparked by the microwave quantum illumination paper by Barzanjeh *et al.* [34]. The authors proposed an electro-optomechanical transmitter and receiver that is an optical cavity coupled to a microwave cavity by a thin membrane to facilitate frequency conversion between the microwave and optical parts of the EM spectrum [36–38].

The first proof-of-principle experiments of quantum illumination were performed using optical frequencies. The first quantum illumination experiment was performed by Lopaeva *et al.* [39], which saw down-converted photon pairs (710 nm, $\bar{n} = 0.075$) compared against two correlated thermal states for classical illumination. The object was a 50:50 beamsplitter. The detection was performed by a CCD camera, where quantum illuminated pixels showed higher SNR. The experiment does not compare results with illumination with coherent states at the

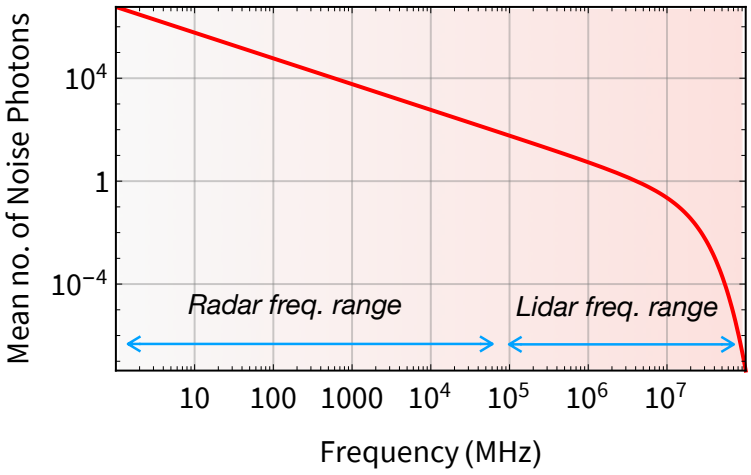

Figure 1.1: Mean number of thermal background noise photons as a function of frequency at 10°C (annual average temperature of Scotland), ranging from 1 MHz to 100 THz. Approximate frequency ranges for radar and lidar are shown in the figure. In the lower radar frequencies, the background noise is high. Lidar incorporates infrared spectrum, and visible frequencies, which begin at around 400 THz. In realistic settings the statistics of different noise sources will differ [1].

same intensity. Zhang *et al.* [40] performed a quantum illumination experiment comparing entangled (1590 nm signal and 1530 nm idler) vs. coherent state of the same intensity, using OPA receivers. The signal and idler fields were directed into optical fibres with noise and loss artificially induced. Experimental imperfections meant only 0.8 dB (20%) enhancement was obtained. The recent experiment by England *et al.* [41] used a modified setup of Lopaeva's experiment but only using single detectors instead of a CCD to directly measure entangled photons of different wavelengths (671 nm signal and 970 nm idler), with background noise added by a jamming laser. They found that down-converted photons improve SNR, but no comparison is made between a coherent state vs. two-mode squeezed vacuum.

Two examples of microwave quantum illumination experiments have been reported – these do not perform microwave-to-optical conversion with EOMs, but instead use directly generated entangled microwaves in the GHz regime from Jospheson parametric amplifiers (JPA) that require mK temperatures to facilitate

superconductivity. The experiment by Chang *et al.* [25] generated microwaves at 4.194 GHz and 6.145 GHz and measured correlations between the entangled modes, compared to separate noise modes for classical illumination. The idler is measured immediately using heterodyne detection. There is no reflection of the signal mode off a target but the authors assumes losses in transmission of the signal directly to a detector as interaction with the target. In the interesting experiment by Barzanjeh *et al.* [42], the signal and idler frequencies were 1.606 GHz and 1.082 GHz. The idler is again measured immediately using heterodyne detection. The signal is reflected off a target whilst travelling through 1m of unrefrigerated free space. Heavy filtering and amplification of the signal and idler modes meant that the correlations in the amplifier noise contributed to the measurement outcome instead of the correlations between the entangled modes, because the amplifier noise was greater than the environmental noise.

The theory of quantum illumination can progress by finding different quantum states and detection methods to find a greater level of quantum supremacy. In practise, however, the range of quantum illumination would be severely limited. The maximum range of a conventional radar (far-field) is

$$r_{max} \propto \left(\frac{P}{P_{min}}\right)^{1/4}, \tag{1.14}$$

where P_{min} is the minimum detectable signal power of the receiver antenna [1]. The max range for a few photons would be on the order of a few metres. And for quantum illumination with laser sources, the highly collimated signal is sensitive to environmental losses. Some authors have suggested that quantum illumination have applications in small-scale, close-range sensing such as in quantum reading [43–46]. Another challenging experimental implementation to reach theory predictions is the requirement to retain the idler mode for a joint measurement, because not only does it require lossless storage of a fragile entangled state, but it requires foreknowledge of the target range so that the idler and signal can be combined at the appropriate time. This is clearly very difficult if not impossible to achieve for a target moving unpredictably, therefore joint measurement schemes should be reserved for applications with static targets.

This provides the motivation for investigating non-simultaneous detection methods: one can simply detect the returning signal directly, after measuring the idler, however this measurement is not optimal, but the method is simpler (shown by Figure 1.2). In this thesis I shall explore direct photodetection for Gaussian state quantum illumination in detail, which could simplify set-ups leading to a more practical quantum radar/lidar. This direct photodetection approach sees the idler mode of a two-mode squeezed vacuum, which does not interact with the environment anyway, being *measured first* with results stored digitally. When a successful idler detection occurs, the information from this detection helps to post-select detection results of the receiving detector because the number of photons in the signal and idler of the two-mode squeezed vacuum are correlated. The measure-first approach breaks entanglement between the signal and idler modes because the measurement itself destroys the idler mode, but in doing so, it conditions the remaining transmitted signal mode into a nonclassical state, therefore this technique would still qualify as "quantum illumination" [47–49].

For articles and more extensive reviews on quantum illumination methods and quantum radar, see refs.[50–53].

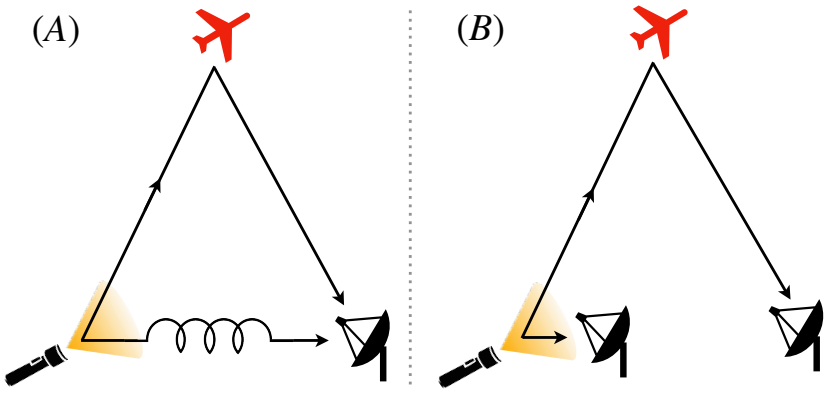

Figure 1.2: Schematic of the optimal vs. non-optimal detection methods. (A) Optimal detection requires photon storage e.g. in loops of optical fibre, so a simultaneous measurement can be made with a returning signal later. (B) Non-optimal, measure-first method. The idler mode is measured first and detection results are compared with the detection results of the returning signal. Residual correlations remain from the initially entangled signal.

1.3 Basic Theoretical Methods

Commonly employed analytical methods are stated here as a preliminary because they are used extensively throughout the thesis. All are well-known aspects of probability theory, quantum optics and quantum information which follow the approach of textbooks in refs. [4, 23].

The physics presented in this thesis are that of the electromagnetic (EM) field of a quantum nature. It is an overall statistical and frequency independent approach, transferable to analysis of general bosonic systems.

A *quantum state* describes an instance of the underlying physical system. It is a useful mathematical object which summarises the information in the underlying field. "Quantum" indicates that there is quantisation of energy in the system into discrete magnitudes. For the EM field, a single quanta i.e. a *photon* has an energy equal to its frequency times Planck's constant

$$E = \hbar\omega, \tag{1.15}$$

often expressed in literature as the "reduced" Planck's constant $\hbar = 1.055 \times 10^{-34}$Js times the angular frequency $\omega = 2\pi f$ [23, 54, 55].

A Hilbert space, $\mathcal{H}$, is a complex vector space with an inner product. Quantum states are either pure or mixed: pure states are rays on $\mathcal{H}$, whereas mixed states are positive-semidefinite operators that act on $\mathcal{H}$ [4, 56]. Expressed in Dirac notation [57], a pure state is represented as a "ket"

$$|\psi\rangle\,, \tag{1.16}$$

that is, a column-vector if expressed in a discrete countable basis. The adjoint of the pure state is the "bra" $\langle\psi|$ that is, a row-vector with complex conjugated values that were contained in $|\psi\rangle$. Mixed states are represented as density operators, denoted as $\hat{\rho}$: they are a probabilistic ensemble of pure states

$$\hat{\rho} = \sum_{i=0}^{\infty} p_i \,|i\rangle\langle i|\,, \tag{1.17}$$

with p_i as the probability of the system existing in state $|i\rangle$. The ket $|i\rangle$ is in the "computational basis', useful thanks to its simplicity

$$|i\rangle\,, \quad i \in \mathbb{N}, \tag{1.18}$$

where two different states are orthogonal have the following inner product

$$\langle i|j\rangle = \delta_{i,j}, \tag{1.19}$$

$\delta_{i,j}$ is the Kronecker delta symbol which equals 1 if $i = j$ and zero otherwise, thus the number states are orthogonal and normalised, which forms a useful orthonormal basis. In this thesis, $|i\rangle$ will denote the pure state containing i-photons [4, 22]. In vector form, $|i\rangle$ is a column-vector that has the value 1 in the i^{th} position (the index starts from 0). Superpositions are allowed for quantum states, written as a linear combination

$$|\psi\rangle = \sum_{i=0}^{\infty} c_i \, |i\rangle \, , \tag{1.20}$$

with the coefficients c_i as complex numbers, such that $\sum_i |c_i|^2 = 1$. A pure state can be expressed as a density operator by taking the following outer product

$$\hat{\rho} = |\psi\rangle\langle\psi| \, , \tag{1.21}$$

but kets alone are sufficient for description of a pure state. Mixed states cannot be factorized in this way. A simple test for the purity of a state is to calculate

$$\text{purity} = \text{tr}(\hat{\rho}^2), \tag{1.22}$$

which if less that 1, the state is mixed. States which are maximally mixed have the density matrix

$$\hat{\rho} = \mathbb{1}_d/d, \tag{1.23}$$

with $\mathbb{1}_d$ as the $d \times d$ identity matrix if working in a finite basis. The maximally mixed state is therefore a d-dimensional state where each pure state occurs with equal probability. All density operators must satisfy the following conditions: unit trace and positive-semidefiniteness. The unit trace property

$$\text{tr}(\hat{\rho}) = 1, \tag{1.24}$$

ensures that the state is properly normalised, similar to a probability distribution, whereas positive-semidefiniteness

$$\hat{\rho} \geq 1, \tag{1.25}$$

ensures that the state is physical – the inequality applies to the density operator eigenvalues.

Observables in quantum information take on the form of Hermitian operators $\hat{O}$. The expectation value of the observable with respect to the quantum state is calculated by the Born rule, by forming the bra-ket

$$\langle \hat{O} \rangle = \langle \psi | \hat{O} | \psi \rangle \,. \tag{1.26}$$

The expectation value of an operator with respect to a mixed state is

$$\langle \hat{O} \rangle = \mathrm{tr}(\hat{O}\hat{\rho}), \tag{1.27}$$

which is equivalent to the pure state expression if $\hat{\rho} = |\psi\rangle\langle\psi|$

$$\langle \hat{O} \rangle = \mathrm{tr}(\hat{O}\,|\psi\rangle\langle\psi|) = \langle \psi | \hat{O} | \psi \rangle \,, \tag{1.28}$$

thanks to the cyclic property of the trace operation

$$\mathrm{tr}(ABC) = \mathrm{tr}(BCA) = \mathrm{tr}(CAB). \tag{1.29}$$

The measurement of the quantum state is encapsulated by the positive operator value measure (POVM) [4, 23]. A measurement is described by a set of operators $\left\{\hat{\Pi}_k\right\}$, each operator element $\hat{\Pi}_k$ within this set represents a specific outcome, which occurs with probability

$$p(k) = \mathrm{tr}\Big(\hat{\Pi}_k \hat{\rho}\Big), \tag{1.30}$$

as provided by the Born rule. All members of the POVM must satisfy the closure relation

$$\sum_k \hat{\Pi}_k = \mathbb{1}, \tag{1.31}$$

and are positive-semidefinite matrices. If the quantum state is representative of a certain hypothesis in a test, say $\hat{\rho}_1$ for H_1, then expression (1.30) can be explicitly defined as a conditional probability of the measurement outcome given the hypothesis

$$p(k|H_1) = \mathrm{tr}\Big(\hat{\Pi}_k \hat{\rho}_1\Big). \tag{1.32}$$

The conditional probability representation is useful for Bayes' Law calculations to estimate posterior probabilities

$$p(H_1|k) = \frac{p(H_1)p(k|H_1)}{p(k)}, \tag{1.33}$$

in a backward process.

1.4 Thesis Layout

Chapter 2 presents Gaussian states and phase space quantum optics. The purpose of this chapter is to summarise how the radiation states are modelled in terms of their photon statistics. I begin by showing correspondence between classical and quantum optics theory, demonstrating that the electric field solutions to Maxwell's equations are analogous with the quadrature operators of the quantum harmonic oscillator. The quantum harmonic oscillator model helps set the foundations to continuous-variable quantum information, Gaussian quantum information and phase space methods. In Gaussian quantum information, Gaussian states are characterised in terms of their first and second statistical moments: the μ (mean) and Σ (covariance). The entangled two-mode squeezed vacuum is mentioned in this chapter, as it is a fundamental example of an entangled Gaussian state that can produce an advantage through quantum illumination. The purpose behind modelling radiation states using Gaussian quantum information is that Gaussian states are experimentally capable, macroscopic quantum states that contain a finite energy (mean photon number).

In chapter 3, I summarise two discrimination measures commonly used in hypothesis testing in quantum information. In radar theory, return signals are discriminated from background by a hypothesis testing procedure which quantifies the differences between their voltage distributions of the signal-plus-background vs. background; H_1 vs. H_0; object present vs. absence. This is translated into quantum information by modelling the state of signal-plus-background and background as density matrices $\hat{\rho}_1$ and $\hat{\rho}_0$, to which they are subjected to either a distance or overlap-based discrimination measure, which both ultimately relates

to an error probability. In some instances, calculation of the distance measure is difficult, for example: multiple observations. Discrimination via overlap based bounds is always possible using the statistical moments of Gaussian states. Hypothesis testing using discrimination measures alone corresponds to optimal detection of quantum states, which cannot be experimentally performed.

In chapter 4, I present the detection theory of photoelectron-counting or "photocounting", which is prerequisite to the binary, on-off detection method. This sub-optimal measurement only contains two outcomes, "click" or "no-click" depending of the vacuum population of the quantum state, and one detector can only measure one mode. The click detector model is then extended to many click detectors in a multiplexed arrangement, such that multiple clicks may occur, to achieve quasi-photon number resolution measurement. Measurement-based state engineering is a technique which uses detection of one mode in an entangled state, in order to condition the non-measured mode into another particular quantum state [58–61]. If the state is the two-mode squeezed vacuum, then a class of multi-click heralded states can be engineered from the detection outcomes using a multiplexed click detector [48, 49]. These single-mode states have a higher or lower mean photon number to their pre-heralded state, depending on the heralding outcome. The states which have a higher mean photon number lead to higher subsequent click probabilities such that it correlated with the heralding detection, and is responsible for the enhancement quantum illumination offers over classical illumination.

Chapter 5 connects the theoretical findings of the previous chapters in the context of the quantum illumination model. Using state discrimination, one can show that quantum illumination is always better than classical illumination for a given signal energy, more so under lossy scenarios. If incorporating sub-optimal click detection, then quantum illumination performs better at low signal energy, whereas for higher signal energy, classical illumination provides higher detection probabilities. Sequential click detection processes are modelled using Monte Carlo simulations, to show the hypothesis estimation capabilities of using classical and quantum illumination, before concluding remarks.

Chapter 2

Gaussian States & Phase Space Quantum Optics

This chapter presents a category of EM field states known as *Gaussian states*, accompanied by analytical methods on quantum phase space. The analytical tools presented here are not strictly limited to photons but extends to other bosonic systems as well. In order to relate and identify common features between the theory of classical vs. quantum radiation, this chapter starts by comparing classical and quantum theory.

Classically, Maxwell's equations in free space have sinusoidal plane-wave solutions, where a single wave with a specific frequency and polarisation can be defined as a "mode" of radiation [62]. A single mode of quantized radiation is modelled by the quantum harmonic oscillator, where energy values occurs in discrete steps, showing the number of photons present in the radiation state. These eigenstates of the quantum harmonic oscillator and energy eigenvalues are solutions of the time-independent Schrödinger equation with a harmonic potential. The eigenstates form a discrete basis that allows basis decomposition of an arbitrary quantum state, informing us of the photon number probability distribution in that particular quantum state.

The position and momentum of a classical particle are tracked by points on a phase space, whereby a certain coordinate (q, p) denotes the state of the particle, with time parameterised. A similar idea is reflected by quantum phase space,

except that for a quantum state, there are precise points, but a distribution of values instead. Position and momentum become operators with real and continuous eigenvalues. The space spanned by the expectation values of both position and momentum operators is therefore the quantum phase space, hwoever the joint position-momentum representation of a quantum state is *not* a proper probability density but a quasiprobability density (so-called *Wigner function*) [63, 64]. However, the marginal distribution (e.g. the momentum distribution of a quantum state) *is* a probability density. Phase space therefore represents a quantum state in a continuous-variable basis. If a state exhibits a Gaussian distribution on phase space, then it is classified as a Gaussian state [46, 65–68]. Gaussian states are well-defined by their first and second statistical moments: the *mean vector*, μ, and *covariance matrix*, Σ [69]. They summarise the coherent amplitude and its variance. Despite this, and with exception to the vacuum state, Gaussian states are infinite-sums expanded in the discrete basis of the quantum harmonic oscillator. Conversion from the discrete to the continuous representation is straightforward and covered in this chapter.

In single-mode: the thermal state, coherent state and the squeezed vacuum each pertain to a Gaussian state with a distinct macroscopic property. The thermal state models thermal noise; coherent state models ideal coherent radiation and the squeezed vacuum have reduced noise along a certain phase angle. States such as thermal coherent states, squeezed coherent states, squeezed thermal states etc. are Gaussian states with composite properties. The only two-mode Gaussian state analysed here is the two-mode squeezed vacuum, which is an entangled Gaussian state, that is correlated in both photon number and quadratures, similar to the state postulated in the original EPR paper [6]. The two-mode squeezed vacuum is an important entanglement resource used for modelling quantum illumination in the later chapters.

2.1 Brief Classical vs. Quantum Theory

2.1.1 Maxwell's Equations

Electric and magnetic vector fields in the vacuum are described by Maxwell's equations, expressed in differential form as

$$\nabla \cdot \mathbf{E} = 0, \tag{2.1}$$

$$\nabla \cdot \mathbf{B} = 0, \tag{2.2}$$

$$-\nabla \times \mathbf{E} = \frac{\partial \mathbf{B}}{\partial t}, \tag{2.3}$$

$$c^2 \nabla \times \mathbf{B} = \frac{\partial \mathbf{E}}{\partial t}, \tag{2.4}$$

where $\mathbf{E}$ and $\mathbf{B}$ are the electric and magnetic field vectors respectively, as functions of space and time [62]. The nabla symbol $\nabla := (\partial_x, \partial_y, \partial_z)$ is the differential operator in 3D. The first two equations are Gauss's laws which describe static EM fields: in free space the divergence of both fields are zero. The latter two equations are Faraday's law and Ampère's law: a time-varying electric field will induce a magnetic field and vice-versa. The constant c in Ampère's law denotes the speed of light in vacuum: expressed in SI units as $2.998 \times 10^8\,\mathrm{ms}^{-1}$.

In terms of potentials, the fields are:

$$\mathbf{E} = -\nabla\varphi - \frac{\partial \mathbf{A}}{\partial t}, \tag{2.5}$$

$$\mathbf{B} = \nabla \times \mathbf{A}, \tag{2.6}$$

where φ denotes a scalar potential and $\mathbf{A}$ a vector potential. By taking the curl of both sides of eq. (2.6), equating to Ampère's Law (2.4) and substituting in the potential equation for $\mathbf{E}$ in (2.5) – the following inhomogeneous wave equation is obtained

$$\nabla(\nabla \cdot \mathbf{A}) - \nabla^2 \mathbf{A} = \frac{1}{c^2}\frac{\partial}{\partial t}\left(\nabla\varphi + \frac{\partial \mathbf{A}}{\partial t}\right). \tag{2.7}$$

In free-space, no current density and no charges implies that $\nabla\varphi = 0$. Then, to ensure that Maxwell's equations still hold with respect to a transformation in the scalar and vector potential ($\varphi \to \varphi - \partial_t\psi(\mathbf{r}, t)$; $\mathbf{A} \to \mathbf{A} + \nabla\psi(\mathbf{r}, t)$) the

gauge is fixed and chosen as the Coulomb gauge, more specifically $\nabla \cdot \mathbf{A} = 0$ [62]. Equation (2.7) is now a homogenous wave equation

$$\nabla^2 \mathbf{A} - \frac{1}{c^2} \frac{\partial^2 \mathbf{A}}{\partial t^2} = 0, \tag{2.8}$$

which has the plane-wave solution for a single field mode

$$\mathbf{A} = \mathbf{e}_{\mathbf{k}\lambda} \left(A_{\mathbf{k}\lambda} e^{-i(\omega_k t - \mathbf{k}\cdot\mathbf{r})} + A^*_{\mathbf{k}\lambda} e^{i(\omega_k t - \mathbf{k}\cdot\mathbf{r})} \right), \tag{2.9}$$

which is a monochromatic and polarised field mode of complex amplitude $A_{\mathbf{k}\lambda}$ and angular frequency ω_k propagating parallel to wavevector $\mathbf{k}$. The full general solution includes the sum over all polarizations λ, and directional unit vectors $\mathbf{e}_{\mathbf{k}\lambda}$, however the single-mode derivation shall suffice for derivations.

The solution of $\mathbf{A}$ then gives the solution for the electric and magnetic fields, by substituting (2.9) into eqs. (2.5) and (2.6)

$$\mathbf{E} = i\omega_k \mathbf{e}_{\mathbf{k}\lambda} \left(A_{\mathbf{k}\lambda} e^{-i(\omega_k t - \mathbf{k}\cdot\mathbf{r})} - A^*_{\mathbf{k}\lambda} e^{i(\omega_k t - \mathbf{k}\cdot\mathbf{r})} \right), \tag{2.10}$$

$$\mathbf{B} = i\mathbf{k} \times \mathbf{e}_{\mathbf{k}\lambda} \left(A_{\mathbf{k}\lambda} e^{-i(\omega_k t - \mathbf{k}\cdot\mathbf{r})} - A^*_{\mathbf{k}\lambda} e^{i(\omega_k t - \mathbf{k}\cdot\mathbf{r})} \right). \tag{2.11}$$

The total energy of a single mode enclosed within an arbitrary volume V is

$$E = \frac{1}{2} \int_{\text{all}} dV \, \left(\epsilon_0 \, \mathbf{E}.\mathbf{E} + \mu_0^{-1} \, \mathbf{B}.\mathbf{B} \right), \tag{2.12}$$

$$= \epsilon_0 V \omega_k^2 \Big(A_{\mathbf{k}\lambda} A^*_{\mathbf{k}\lambda} + A^*_{\mathbf{k}\lambda} A_{\mathbf{k}\lambda} \Big), \tag{2.13}$$

using the identity $(\mathbf{k} \times \mathbf{e}_{\mathbf{k},\lambda}).(\mathbf{k} \times \mathbf{e}_{\mathbf{k},\lambda}) = k^2$. Conveniently, the time-dependent terms vanish as the squared terms $A^2_{\mathbf{k}\lambda}$ and $(A^*_{\mathbf{k}\lambda})^2$ cancel out, leaving a time independent energy term [62, 70].

2.1.2 Quantum Harmonic Oscillator

The quantum harmonic oscillator is analogous to the classical harmonic oscillator system, except that the energy is restricted to discrete levels $|n\rangle$, $n \in \mathbb{N}$, known as energy eigenstates, that are well standardised by textbooks [4, 23, 70, 71]. The stationary states of the quantum harmonic oscillator are solutions of the time-independent Schrödinger equation

$$\hat{H} \, |n\rangle = E_n \, |n\rangle \, , \tag{2.14}$$

where E_n are the energy eigenvalues of the eigenstates. The total energy operator is called the Hamiltonian

$$\hat{H} = \hat{K} + \hat{V}, \tag{2.15}$$

which consists of the kinetic and the harmonic potential energy operators

$$\hat{K} = \frac{\hat{p}^2}{2m}, \qquad \hat{V} = \frac{1}{2}m\omega\hat{q}^2. \tag{2.16}$$

Both equations have maintained the same form as their classical counterparts, except position and momentum have been converted to operators: $\hat{q}$ and $\hat{p}$.

By scaling to "natural units" where $\hbar = \omega = m = 1$ the Hamiltonian becomes

$$\hat{H} = \tfrac{1}{2}(\hat{p}^2 + \hat{q}^2), \tag{2.17}$$

which shows position and momentum operators as quadratures. The operators do not commute, forming the well-known commutation relation

$$[\hat{q}, \hat{p}] := \hat{q}\hat{p} - \hat{p}\hat{q} = i. \tag{2.18}$$

They also obey Heisenberg's uncertainty principle, being conjugate observables

$$\langle\Delta\hat{q}\rangle^2\langle\Delta\hat{p}\rangle^2 \geq \tfrac{\hbar^2}{4}, \tag{2.19}$$

where $\Delta\hat{A} := \hat{A} - \langle\hat{A}\rangle$. The uncertainty principle is expressed here as a product of variances of the operators [70].

Instead of solving directly for the eigenstates in eqn. (2.14), the "ladder method" is used [57, 70, 71]. The following operators

$$\hat{a} = \tfrac{1}{\sqrt{2}}\left(\hat{q} + i\hat{p}\right), \qquad \hat{a}^\dagger = \tfrac{1}{\sqrt{2}}\left(\hat{q} - i\hat{p}\right), \tag{2.20}$$

are the annihilation operator, $\hat{a}$, with its adjoint $\hat{a}^\dagger$ as the creation operator, representing elementary operations within the oscillator. The commutation relation (2.19) becomes

$$[\hat{a}, \hat{a}^\dagger] = 1. \tag{2.21}$$

The quadratures in terms of $\hat{a}$ and $\hat{a}^\dagger$ are:

$$\hat{q} = \tfrac{1}{\sqrt{2}}(\hat{a}^\dagger + \hat{a}), \qquad \hat{p} = \tfrac{i}{\sqrt{2}}(\hat{a}^\dagger - \hat{a}), \tag{2.22}$$

meaning that the Hamiltonian in eq. (2.17) can be rearranged to

$$\hat{H} = \tfrac{1}{2}(\hat{a}^\dagger \hat{a} + \hat{a}\hat{a}^\dagger). \tag{2.23}$$

Comparing with eq. (2.13), the Hamiltonian is now similar to E, up to a normalisation. Using the commutation relation eq. (2.21), the rearranged Hamiltonian is now

$$\hat{H} = \hat{a}^\dagger \hat{a} + \tfrac{1}{2}, \tag{2.24}$$

which includes the photon number operator

$$\hat{n} := \hat{a}^\dagger \hat{a}, \tag{2.25}$$

The expectation value of $\hat{n}$ shows the mean number of photons present in the system. The number operator forms the following relation with the energy eigenstate

$$\hat{n} \left|n\right\rangle = n \left|n\right\rangle, \tag{2.26}$$

where n is the number of photons. Using this relation, the energy eigenvalue is

$$E_n = n + \tfrac{1}{2}. \tag{2.27}$$

The time-independent Schrödinger equation is therefore

$$\hat{H} \left|n\right\rangle = (n + \tfrac{1}{2}) \left|n\right\rangle. \tag{2.28}$$

Therefore, the expectation value of the Hamiltonian or the energy of the oscillator is directly proportional to the mean number of photons plus a half. When no photons are present in the oscillator, the vacuum state $|0\rangle$ retains a finite zero-point energy $E_0 = \frac{1}{2}$. Successive eigenstates are equally spaced by an energy difference of $\hbar\omega = 1$, which is the energy of a single photon. The operators $\hat{a}$ and $\hat{a}^\dagger$ cause step-wise transitions between different energy states

$$\hat{a} \left|n\right\rangle = \sqrt{n} \left|n-1\right\rangle, \tag{2.29}$$

$$\hat{a}^\dagger \left|n\right\rangle = \sqrt{n+1} \left|n+1\right\rangle, \tag{2.30}$$

hence $\hat{a}$ removes or "annihilates" a photon whereas $\hat{a}^\dagger$ adds or "creates" a photon in the oscillator. The vacuum state cannot be lowered

$$\hat{a} \left|0\right\rangle = 0, \tag{2.31}$$

because obviously there are no more photons to be removed. Creation and annihilation operators demonstrate simple operations, but they are considered as non-observables, as they are non-Hermitian.

The discrete energy eigenstates $|n\rangle$ are therefore photon number states or Fock states. An n-photon state is generated by applying the creation operator to a vacuum state n-times

$$|n\rangle = \frac{(\hat{a}^\dagger)^n}{\sqrt{n!}} |0\rangle \,. \tag{2.32}$$

Inner product between two different number states is

$$\langle n|m\rangle = \delta_{n,m}, \tag{2.33}$$

where $\delta_{n,m}$ is the Kronecker delta function which equals one when $n = m$, and zero otherwise. The identity operator is expressed in the number state basis as

$$\mathbb{1} = \sum_{n=0}^{\infty} |n\rangle\langle n| \,. \tag{2.34}$$

Number states form a orthogonal and normalized (orthonormal) basis, useful for analysing an arbitrary quantum state in the context of the quantum harmonic oscillator. Such a description show the distribution of photons throughout the energy levels. The photon number distribution is

$$P(n) = \langle n|\hat{\rho}|n\rangle \,, \tag{2.35}$$

that is a probability mass function, also they are the diagonals of the state density matrix.

Correspondence between field modes obtained by solving Maxwell's equations and the quantum harmonic oscillator operators can be seen by comparison of the Hamiltonian expressed in the form of eq. (2.23) with the classical energy expression eq. (2.13), suggesting that the vector potential is quantized as [72]

$$A_{\mathbf{k}\lambda} \to \sqrt{\frac{\hbar}{2\epsilon_0 V \omega_k}} \hat{a}_{\mathbf{k}\lambda}. \tag{2.36}$$

Electric and magnetic field operators are expressed in terms of creation and an-

nihilation operators as

$$\hat{E} = \mathbf{e}_{\mathbf{k}\lambda}\sqrt{\frac{\hbar\omega_k}{2\epsilon_0 V}}\left(\hat{a}_{\mathbf{k}\lambda}e^{-i\phi_k(\mathbf{r},t)} + \hat{a}^\dagger_{\mathbf{k}\lambda}e^{i\phi(\mathbf{r},t)}\right), \tag{2.37}$$

$$\hat{B} = \mathbf{k}\times\mathbf{e}_{\mathbf{k}\lambda}\sqrt{\frac{\hbar}{2\epsilon_0 V\omega_k}}\left(\hat{a}_{\mathbf{k}\lambda}e^{-i\phi(\mathbf{r},t)} + \hat{a}^\dagger_{\mathbf{k}\lambda}e^{i\phi(\mathbf{r},t)}\right), \tag{2.38}$$

where the imaginary factor in eqs. (2.10) and (2.11) has been absorbed into the phase

$$\phi(\mathbf{r},t) = \omega_k t - \mathbf{k}.\mathbf{r} - \tfrac{\pi}{2}. \tag{2.39}$$

Back in natural units, the electric field operator is directly related to a generalised quadrature operator

$$\hat{E}_\phi \equiv \hat{x}_\phi := \tfrac{1}{\sqrt{2}}(\hat{a}e^{-i\phi} + \hat{a}^\dagger e^{i\phi}), \tag{2.40}$$

which allows the determination of the state marginal distribution at any phase angle. The position and momentum operators are recovered by setting the phase angle at zero and $\pi/2$. The electric field operator can then be decomposed in terms of position and momentum operators

$$\hat{E}_\phi = \hat{q}\cos\phi + \hat{p}\sin\phi, \tag{2.41}$$

showing the real and imaginary parts of the electric field mode. Generalised quadrature operators forms the following relation

$$\hat{x}_\phi\left|x_\phi\right\rangle = x_\phi\left|x_\phi\right\rangle \tag{2.42}$$

with $|x_\phi\rangle$ as the quadrature eigenstate and x_ϕ the quadrature eigenvalue that take on continuous values. The inner product of two general quadrature eigenstates is

$$\left\langle x'_\phi\middle|x_\phi\right\rangle = \delta(x'_\phi - x_\phi), \tag{2.43}$$

where $\delta(x)$ is the Dirac delta function. This identity show that the quadrature eigenstates $|x_\phi\rangle$ are considered "improper" eigenstates, because the Dirac delta cannot be normalized. The quadrature eigenstates are orthogonal but not normalisable

$$\mathbb{1} = \int_{-\infty}^{\infty} dx_\phi\ \left|x_\phi\right\rangle\!\left\langle x_\phi\right|. \tag{2.44}$$

The overlap between a quantum state and the quadrature eigenstate gives a marginal distribution of the state at phase angle ϕ, that is a proper probability density. The position wavefunction of a pure state $|\psi\rangle$ is obtained through the inner product with the position eigenstate

$$\psi(q) = \langle q|\psi\rangle \,. \tag{2.45}$$

The momentum wavefunction is obtained through the Fourier transform

$$\psi(p) = \frac{1}{2\pi}\int_{-\infty}^{\infty} dq\, \psi(q) e^{-iqp}. \tag{2.46}$$

By re-casting the wavefunction into coordinate space, the time-independent Schrödinger equation for the quantum harmonic oscillator can be solved to prove that indeed the solutions are wave-like [73]. For example, the position wavefunction of a number state are a set of functions which contain the Hermite polynomials

$$\psi_n(q) = \langle q|n\rangle = \frac{1}{\pi^{1/4}\sqrt{2^n n!}} H_n(q) e^{-q^2/2}, \tag{2.47}$$

with $H_n(x)$ as the n^{th} order Hermite polynomial.

Therefore, we have two statistical representations for a quantum state: discrete and continuous. In relevant literature for continuous variable quantum mechanics, care must be taken when converting from discrete to continuous space as authors use different $\hbar$ scaling conventions for the quadrature operators. This effectively re-scales the uncertainty principle in eq. (2.19). For example, in refs. [65, 72], the convention is $\hbar = \frac{1}{2}$, meaning that the uncertainty principle is

$$\langle \Delta\hat{q}^2\rangle \langle \Delta\hat{p}^2\rangle \geq \tfrac{1}{16}. \tag{2.48}$$

Whereas in refs. [46, 74], $\hbar = 2$ meaning that

$$\langle \Delta\hat{q}^2\rangle \langle \Delta\hat{p}^2\rangle \geq 1. \tag{2.49}$$

which is normalised to the quadrature variance of the vacuum state. These minor differences affect normalisation factors and can produce inconsistencies during analysis; ref. [59] gives a summary of all three scaling conventions.

2.2 Gaussian States

From the most general perspective: a Gaussian state is either a thermal state or a thermal state evolved under a Gaussian unitary operation

$$\hat{\rho}' = \hat{U}\hat{\rho}\hat{U}^{\dagger}, \tag{2.50}$$

where

$$\hat{U} = e^{-i\hat{H}t}, \tag{2.51}$$

is the unitary operator which evolves the system in time t. A unitary operator is Gaussian if the Hamiltonian contains creation and annihilation operators up to a maximum of the second order [46, 59, 65]

$$\hat{H}_G = \sum_{k=1}^{N} g_k^{(1)} \hat{a}_k^{\dagger} + \sum_{k>l=1}^{N} g_{kl}^{(2)} \hat{a}_k^{\dagger}\hat{a}_l + \sum_{k,l=1}^{N} g_{kl}^{(3)} \hat{a}_k^{\dagger}\hat{a}_l^{\dagger} + \text{h.c.}\,. \tag{2.52}$$

This is a general sum-expansion for N-modes: each operator has attached coupling coefficients $g^{(m)}$; notice that only two modes may couple together and no more. Each sum group of the Hamiltonian along with its Hermitian conjugate generates a particular type of Gaussian state: the first is the displacement operation, which generates coherent states; the second is for photon-conserving processes between two separate modes such as that in the beamsplitter, as well as free evolution of modes for $\hat{a}_k^{\dagger}\hat{a}_k$ (the terms may be removed via the interaction picture); the last corresponds to single-mode and two-mode squeezing that generates squeezed states as a result of two-photon processes, i.e. $\hat{a}_k^{\dagger}\hat{a}_l^{\dagger}$. The vacuum state and its evolution under a Gaussian unitary creates the set of pure Gaussian states, whereas those for thermal states are mixed Gaussian states [46].

2.2.1 Thermal States

Besides the vacuum state – the fundamental Gaussian state is the thermal state. They are fundamental because they form an irreducible "core" to which general Gaussian states can be reduced. In the latter chapters, the thermal state is used to model background noise sources. It is a state of a system in a thermal

equilibrium with its surroundings at temperature T. It has the following density matrix

$$\hat{\rho}_{th} = \frac{e^{-\beta\hat{H}}}{\mathrm{tr}\left(e^{-\beta\hat{H}}\right)}, \tag{2.53}$$

where $\beta := (k_B T)^{-1}$ and k_B being Boltzmann's constant. The density matrix is analogous to the probability of finding the system in at a certain energy within the classic canonical ensemble [70, 73], with energy replaced by the Hamiltonian operator. Substitution of the harmonic oscillator Hamiltonian in eq. (2.24) gives

$$\hat{\rho}_{th} = (1 - e^{-\beta}) \sum_{n=0}^{\infty} e^{-\beta n} \left|n\right\rangle\!\left\langle n\right| . \tag{2.54}$$

The mean number of photons in a thermal state is

$$\bar{n} = (e^{\beta} - 1)^{-1}. \tag{2.55}$$

Re-substitution of the above expression into eq. (2.54) gives the density matrix solely in terms of $\bar{n}$

$$\hat{\rho}_{th} = \frac{1}{1+\bar{n}} \sum_{n=0}^{\infty} \left(\frac{\bar{n}}{\bar{n}+1}\right)^{n} \left|n\right\rangle\!\left\langle n\right| , \tag{2.56}$$

which is a statistical mixture of different number states that follow a Bose-Einstein distribution, shown in Figure 2.1. The thermal state has a photon number variance of

$$\langle \Delta\hat{n}^2 \rangle = \bar{n}(1+\bar{n}), \tag{2.57}$$

which is always greater than the mean, referred to as "super-Poissonian" behaviour that is characteristic of thermal light [70, 72]. Looking at eq. (2.56), the greatest probability for finite temperatures remains with the ground state (vacuum state) at $(1+\bar{n})^{-1}$, shown by Figure 2.1. The higher photon number levels are populated by increasing $\bar{n}$. This flattens out the distribution and at the limiting case of $\bar{n} \to \infty$, the thermal state tends to a maximally-mixed state $\hat{\rho} \approx \mathbb{1}/(1+\bar{n})$, as the coefficients in eqn. (2.56) approach unity.

For quadratures, the thermal state has zero-mean amplitude

$$\langle \hat{E}_{\phi} \rangle = 0, \tag{2.58}$$

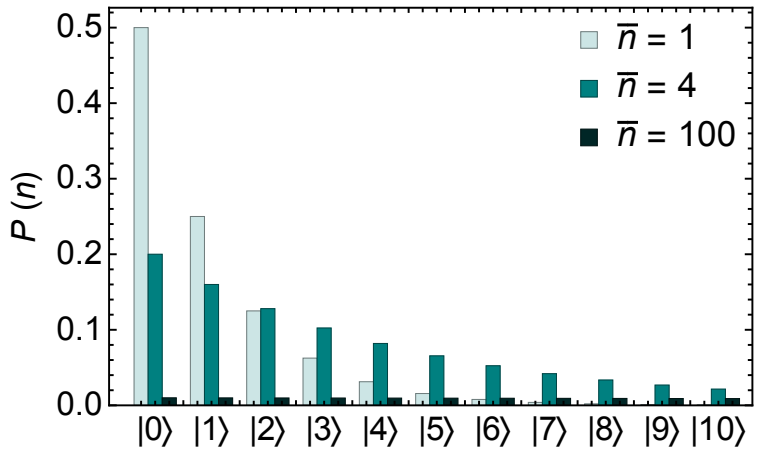

Figure 2.1: Photon number distribution of thermal states with various mean photon numbers of $\bar{n} = 1$, $\bar{n} = 4$ and $\bar{n} = 100$, throughout 10 harmonic oscillator levels. The photons are distributed via a Bose-Einstein distribution (or geometric series) in which the ground state maintains the highest probability. For $\bar{n} = 1$, probabilities tail off after the vacuum, following a $2^{-(1+n)}$ trend for successive photon numbers, therefore the probability of such a thermal state containing 8 photons is low ($2^{-(1+8)} \approx 0.2\%$). Increasing the mean photon number will distribute photons into higher harmonic oscillator levels, but flattens out the distribution (in the case of $\bar{n} = 100$).

however the variance is non-zero

$$\langle \Delta \hat{E}_{\phi}^{2} \rangle = \bar{n} + \tfrac{1}{2}. \tag{2.59}$$

No phase terms exist in both of these expressions therefore the average electric field of thermal state is distributed around the origin of the phase space. In the instance of zero mean photons, the vacuum state has a field variance of 1/2.

2.2.2 Coherent States

The coherent states of the quantum harmonic oscillator are an important class of pure states that are sometimes used to model the statistics of ideal monochromatic laser light at the quantum shot-noise limit. A coherent state has the following

photon number basis expansion:

$$|\alpha\rangle = e^{-|\alpha|^2/2} \sum_{n=0}^{\infty} \frac{\alpha^n}{\sqrt{n!}} |n\rangle \,, \tag{2.60}$$

with complex amplitude α [70, 72, 75]. The coherent state is a left-eigenstate of the creation operator and a right-eigenstate of the annihilation operator

$$\langle\alpha| \hat{a}^\dagger = \langle\alpha| \alpha^*, \qquad \hat{a} |\alpha\rangle = \alpha |\alpha\rangle \,. \tag{2.61}$$

The mean photon number of a coherent state is the modulus-squared of the complex amplitude

$$\bar{n} = |\alpha|^2, \tag{2.62}$$

which equates to the photon number variance

$$\langle \Delta \hat{n}^2 \rangle = |\alpha|^2. \tag{2.63}$$

Equal mean and variance indicate Poissonian statistics, which is reflected in the photon number distribution of the coherent state

$$P(n) = \frac{\bar{n}^n}{n!} e^{-\bar{n}}, \tag{2.64}$$

shown in Figure 2.2. The greatest photon number probability occurs near $|n \approx \bar{n}\rangle$, rather than the ground state for thermal states.

The coherent state is generated by evolution of the vacuum state under the displacement unitary operator

$$|\alpha\rangle = \hat{D}(\alpha) |0\rangle \,. \tag{2.65}$$

The displacement operator being

$$\hat{D}(\alpha) = e^{\alpha \hat{a}^\dagger - \alpha^* \hat{a}}, \tag{2.66}$$

and comparing with the general Gaussian unitary in eq. (2.52), the Hamiltonian is of the first order in $\hat{a}$ and $\hat{a}^\dagger$. In order to derive the number basis expansion from eq. (2.65), the displacement unitary must be factorised into products of exponential operators, by application of the Baker-Campbell-Hausdroff formula [59, 70]

$$\hat{D}(\alpha) = e^{-|\alpha|^2/2} e^{\alpha \hat{a}^\dagger} e^{-\alpha^* \hat{a}}, \tag{2.67}$$

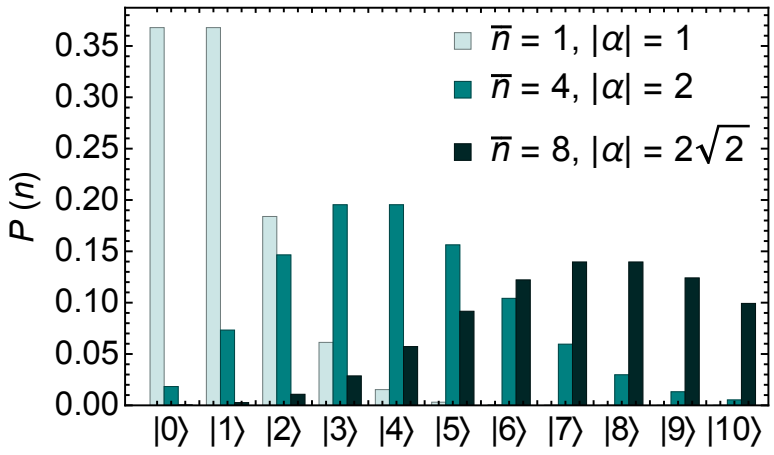

Figure 2.2: Photon number distribution of coherent states with various amplitudes. Photons in the coherent state are distributed via a Poissonian distribution, with the highest probability occurring around the mean photon number. Larger amplitudes results in further displacement of the distribution peak from the vacuum state, but as the variance is proportional to the mean, there results a greater spread also.

because for exponential operators factorisation such as $e^{\hat{x}}e^{\hat{y}} = e^{\hat{x}+\hat{y}}$ is true only if $\hat{x}$ and $\hat{y}$ commute, hence for non-commuting operators, factorising the exponent of operator sums into products of exponential operators require general operator ordering theorems [70]. An exponential operator can be expanded as a series via

$$e^{\hat{x}} = \sum_{k=0}^{\infty} \frac{\hat{x}^k}{k!}, \tag{2.68}$$

and applying the above equation in conjunction with eq. (2.67) to the vacuum state, provides the number state basis expansion in (2.60).

The displacement operator shifts the vacuum to a magnitude of $|\alpha|$, the same occurs to the electric field amplitude

$$\langle \hat{E}_\phi \rangle = \sqrt{2}|\alpha| \cos(\theta - \phi), \tag{2.69}$$

where θ is the displacement angle. The variance remains unchanged as

$$\langle \Delta \hat{E}_\phi^2 \rangle = \tfrac{1}{2}. \tag{2.70}$$

The quadrature variance of a coherent state is the same as the vacuum state,

saturating the lower bound of Heisenberg's uncertainty principle in eq. (2.19) – these are known as minimum uncertainty states.

A basis can be constructed using coherent states, but it is "over-complete". The identity resolved in a coherent state basis is

$$\mathbb{1} = \frac{1}{\pi} \int d^2\alpha \; |\alpha\rangle\langle\alpha| \,, \tag{2.71}$$

but the overlap of two coherent states is not orthogonal

$$\langle\beta|\alpha\rangle = e^{-\frac{1}{2}(|\beta|^2+|\alpha|^2-2\beta^*\alpha)}. \tag{2.72}$$

Density matrices expanded in the coherent basis require a weight function $P(\alpha)$, which represents the state as an expansion of classical waves with complex amplitude α. This representation is not really suitable for nonclassical states because it becomes highly singular and difficult to work with – an example is given in the next section.

2.2.3 Single-Mode Squeezed Vacuum

Squeezed states are nonclassical Gaussian states produced from parametric amplification processes [24, 76]. Their defining feature is having reduced noise along one quadrature, and in certain instances, below the variance of the vacuum state of 1/2. But the trade-off is that the orthogonal quadrature increases in noise, constrained by the uncertainty principle

$$\langle\Delta\hat{x}_\phi^2\rangle\langle\Delta\hat{x}_{\phi+\pi/2}^2\rangle \geq \tfrac{1}{4}. \tag{2.73}$$

Squeezed states relate to photon pairs: in the single-mode squeezed vacuum both photons are in the same mode. This is apparent in the wavefunction of the squeezed vacuum expanded in the number basis as

$$|\zeta\rangle = \frac{1}{\sqrt{\cosh r}} \sum_{n=0}^{\infty} \left(-\frac{e^{i\varphi}}{2} \tanh r \right)^n \frac{\sqrt{(2n)!}}{n!} \, |2n\rangle \,, \tag{2.74}$$

where ζ is the complex squeezing amplitude, that has $r \equiv |\zeta|$ as the squeezing strength and φ the squeezing phase. The photon number distribution for the squeezed vacuum is show by Figure 2.3. Despite having "vacuum" in its name,

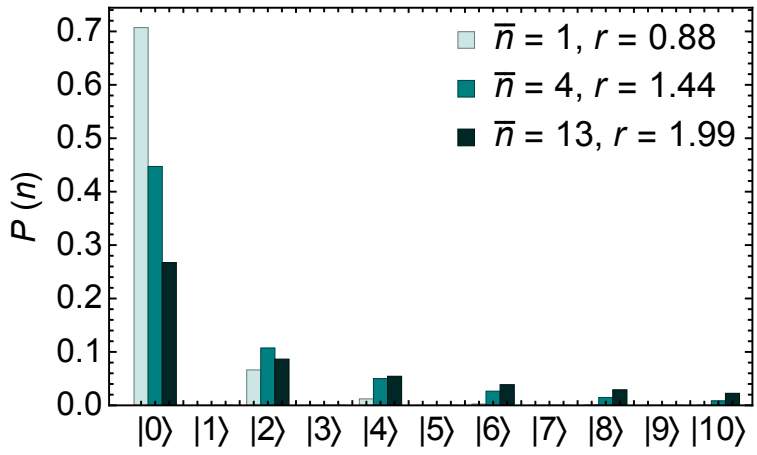

Figure 2.3: Photon number distribution of the single-mode squeezed vacuum under various squeezing amplitudes. The distribution only contains occupation at even photon numbers, and overall has a similar trend to the thermal state where the ground state contains the highest occupation. Increasing squeezing increases the mean photon number within the state, occupying higher energy levels.

the mean number of photons in a squeezed vacuum is not zero, but a hyperbolic function of the squeezing amplitude [70, 77]

$$\bar{n} = \sinh^2 r. \tag{2.75}$$

The photon number variance is

$$\langle \Delta \hat{n}^2 \rangle = 2\bar{n}(\bar{n}+1), \tag{2.76}$$

which is double the thermal state variance [70], hence the squeezed vacuum is also super-Poissonian.

The single-mode squeezed vacuum is generated from the vacuum state by

$$|\zeta\rangle = \hat{S}(\zeta)\,|0\rangle\,, \tag{2.77}$$

where

$$\hat{S}(\zeta) = e^{-\frac{1}{2}(\zeta \hat{a}^{\dagger 2} - \zeta^* \hat{a}^2)}, \tag{2.78}$$

is the single-mode squeezing operator. The ordered single-mode squeezing operator is

$$\hat{S}(\zeta) = e^{-\frac{1}{2}\hat{a}^{\dagger 2} e^{i\varphi} \tanh r} e^{-\frac{1}{2}(\hat{a}^\dagger \hat{a} + \hat{a}\hat{a}^\dagger)\log(\cosh r)} e^{-\frac{1}{2}\hat{a}^2 e^{-i\varphi} \tanh r} \tag{2.79}$$

which applied to the vacuum state generates the number basis expansion in eq. (2.74) [59, 70].

Similar to the vacuum state and the thermal state, the squeezed vacuum has a mean field of zero

$$\langle \hat{E}_\phi \rangle = 0, \tag{2.80}$$

however the variance is phase dependent

$$\langle \Delta \hat{E}_\phi^2 \rangle = \tfrac{1}{2} e^{-2r} \cos^2(\phi - \varphi/2) + \tfrac{1}{2} e^{2r} \sin^2(\phi - \varphi/2), \tag{2.81}$$

showing that there is a reduction in variance along certain squeezing angles with respect to the squeezing phase. For example, setting $\phi = \varphi = 0$, the variance of the position and momentum operators become

$$\langle \Delta \hat{q}^2 \rangle = \tfrac{1}{2} e^{-2r}, \qquad \langle \Delta \hat{p}^2 \rangle = \tfrac{1}{2} e^{2r}, \tag{2.82}$$

such that the variance in the position quadrature is decreased below the standard quantum limit of 1/2 for $r > 0$. The squeezing is often quoted in decibels (dB) and refers to the power ratio between the variance of the squeezed quadrature vs. the vacuum [24]

$$\text{squeezing (dB)} = 10 \log_{10}(e^{-2r}). \tag{2.83}$$

Experimentally, single-mode squeezed states are produced by degenerate parametric down-conversion processes [24, 76, 78], where both output beams are in the same mode. The squeezed vacuum is so named because the down-conversion is triggered by vacuum fluctuations – in essence it is an amplified vacuum. If emission is triggered by a coherent pump source, then the output would be a displaced squeezed state [70, 76]

$$|\alpha, \zeta\rangle = \hat{D}(\alpha)\hat{S}(\zeta)\,|0\rangle\,, \tag{2.84}$$

which contain a mean photon number of $\bar{n} = \sinh^2 r + |\alpha|^2$ [77]. Squeezing therefore reduces the noise along one phase angle, whilst displacement changes the coherent amplitude of the state.

2.2.4 Two-Mode Squeezed Vacuum

When parametric down-conversion outputs photons that are distinguishable, then the global state is a *two-mode squeezed vacuum* (TMSV). The TMSV expanded in the photon number basis is [59, 70, 79]

$$|\Psi\rangle = \sqrt{1-\tanh^2 r}\sum_{n=0}^{\infty}(e^{i\varphi}\tanh r)^n\,|n,n\rangle\,, \tag{2.85}$$

which shows photon number correlation in the conventionally known *signal* and *idler* modes in a composite basis $|n,n\rangle = |n\rangle\otimes|n\rangle$ (as the signal and idler have the same coefficients they are statistically indistinguishable from each other). This state is an example of an entangled Gaussian state [80]. In the low-squeezing regime the state approximates a photon-pair state

$$|\Psi\rangle \approx |0,0\rangle + r\,|1,1\rangle\,. \tag{2.86}$$

The TMSV is therefore the general state of non-degenerate parametric down-conversion that includes multiple photons in twin-beams with photon number correlations. The TMSV is generated by

$$|\Psi\rangle = \hat{S}_2(\zeta)\,|0,0\rangle\,, \tag{2.87}$$

where the two-mode squeezing operator is

$$\hat{S}_2(\zeta) = e^{-\zeta\hat{a}^\dagger\hat{b}^\dagger+\zeta^*\hat{a}\hat{b}}, \tag{2.88}$$

with $\hat{b}$ as the field operator for the second mode. In ordered form [70], this operator is

$$\hat{S}_2(\zeta) = e^{-\hat{a}^\dagger\hat{b}^\dagger e^{i\varphi}\tanh r}e^{-\frac{1}{2}(\hat{a}^\dagger\hat{a}+\hat{b}^\dagger\hat{b})\log(\cosh r)}e^{-\hat{a}\hat{b}\,e^{-i\varphi}\tanh r}, \tag{2.89}$$

and is required to derive the number state expansion in eq. (2.85).

Entangled states lose information when one mode is considered without the other. This can be seen by taking the partial trace of the TMSV, which leaves a thermal state remaining

$$\mathrm{tr}_s(|\Psi\rangle\langle\Psi|) = (1-\tanh^2 r)\sum_{n=0}^{\infty}\tanh^{2n} r\,|n\rangle\langle n|\,, \tag{2.90}$$

with mean photon number

$$\bar{n} = \sinh^2 r, \tag{2.91}$$

thus only through simultaneous measurement of both modes, the intensity correlations can be verified.

Expressing eq. (2.90) in terms of $\bar{n}$ produces the same expression as the thermal state density matrix in eq. (2.56). The total mean number of photons in the TMSV therefore total $2\bar{n}$. The variance of the mean photon number difference vanishes

$$\langle \Delta(\hat{n}_s - \hat{n}_i)^2 \rangle = \langle \Delta \hat{n}_s^2 \rangle + \langle \Delta \hat{n}_i^2 \rangle - 2(\langle \hat{n}_s \hat{n}_i \rangle - \langle \hat{n}_s \rangle \langle \hat{n}_i \rangle) = 0, \tag{2.92}$$

as a result of its photon number correlations. The loss of information due to partial tracing of the entangled TMSV, is analogous to the instance where by taking the partial trace of an entangled Bell state leaves a remaining maximally mixed state – the TMSV is the purification of the thermal state [4, 81].

The state is "squeezed" in the sense that the sum and difference of the position and momentum operators between both modes show a reduction in variance

$$\langle \Delta(\hat{q}_1 - \hat{q}_2)^2 \rangle = e^{-2r}, \qquad \langle \Delta(\hat{p}_1 + \hat{p}_2)^2 \rangle = e^{-2r}, \tag{2.93}$$

as a result of the inter-mode quadrature correlations [79, 82, 83]. In the limit of $r \to \infty$, the state becomes delta-correlated over all photon numbers in the form of the EPR state [6], although this would be unphysical. With photon number correlations and quadrature correlations, the TMSV is a very useful entangled state which will produce correlated measurement results stronger than that for classical states [17, 84].

2.3 Phase Space Quantum Optics

2.3.1 Characteristic & Wigner Functions

All states and operators can be represented on phase space – the starting transformation is through the *characteristic function* which maps from a discrete basis

into the continuous variable basis [59, 70]. The quantum characteristic function is expectation value of the displacement operator

$$\chi(\xi) = \langle \hat{D}(\xi) \rangle; \tag{2.94}$$

this particular characteristic function is for symmetrically-ordered boson operators [70]. In standard probability theory, the characteristic function is the Fourier transform of a probability density [59, 85]. A subsequent Fourier transform of the quantum characteristic function results in *Wigner function*

$$W(\alpha) = \frac{1}{\pi^2} \int d^2\xi \, \chi(\xi) \, e^{\alpha\xi^* - \xi\alpha^*}, \tag{2.95}$$

which in this case is refers to a single-mode; for N-modes states the above integral runs over $2N$ variables. The Wigner function is a well-known example of a phase space "quasiprobabilistic" distribution: it is not a genuine probability density as negative values are permitted. The marginals, however, are positive and related to $\langle \hat{x}_\phi \rangle$. For example, number states demonstrate the negativity of Wigner functions:

$$W(\alpha) = \frac{2}{\pi}(-1)^n L_n\left(4|\alpha|^2\right) e^{-2|\alpha|^2}, \tag{2.96}$$

where $L_n(x)$ are the standard Laguerre polynomials [73]. An example for a three photon state is shown by Figure 2.4. The distinct negativity of the Wigner function clearly indicate nonclassical behaviour of a state [73, 86–88]. It is a sufficient, but not a necessary condition, because the single-mode squeezed states have an entirely positive Wigner function

$$W(\alpha) = \frac{2}{\pi} e^{-2(e^{-2r}\mathrm{Re}(\alpha)^2 + e^{2r}\mathrm{Im}(\alpha)^2)}. \tag{2.97}$$

The other two well-known quasiprobability distributions are the P and Q-functions. The P-function [89] enables the density matrix to be expanded in the coherent basis

$$\hat{\rho} = \int d^2\alpha \, P(\alpha) \, |\alpha\rangle\langle\alpha| \, . \tag{2.98}$$

The P-function is derived by by taking the Fourier transform of the characteristic function, similar to eq. (2.95), but under normal boson operator ordering [75].

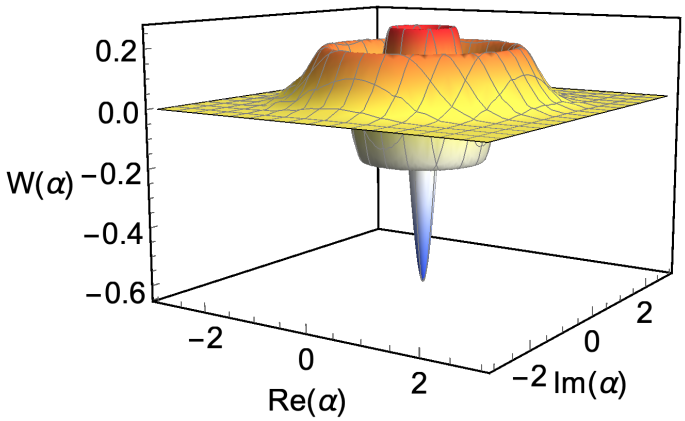

Figure 2.4: Wigner function of the three photon state, $|3\rangle$. The Wigner function, or all phase space quasiprobabilities, are not proper multivariate probability distributions. Only the marginal distributions are related to actual probability distributions of a quadrature expectation value, found by integrating over a quadrature, e.g. $\frac{1}{2}\int W(q,p)\,dp = \langle q|\,\hat{\rho}\,|q\rangle$.

Despite having a straightforward interpretation, the P-function becomes difficult to handle for certain nonclassical states: the P-function of a number state is

$$P(\alpha) = \sum_{m=0}^{n} \binom{n}{m} \frac{1}{m!} \left(\frac{\partial^2}{\partial\alpha\partial\alpha^*}\right)^m \delta^{(2)}(\alpha), \tag{2.99}$$

which contains m^{th} order derivatives of the Dirac delta function. Positivity of the P-function is often used as a yes/no test to determine whether a state is classical or not [88]. The Q-function, is directly available via

$$Q(\alpha) = \frac{1}{\pi}\,\langle\alpha|\hat{\rho}|\alpha\rangle\,, \tag{2.100}$$

which is the expectation value of the density matrix with respect to the coherent state [90, 91]. It can also be calculated via the Fourier transform of the characteristic function under anti-normal boson operator ordering [22]. The Q-function is positive semi-definite everywhere, and in contrast to the P-function the Q-function for the number state is

$$Q(\alpha) = e^{-|\alpha|^2}\frac{|\alpha|^{2n}}{\pi n!}, \tag{2.101}$$

similar to the photon number distribution of the coherent state in eq. (2.64) divided by π. Despite being positive, the function is still considered a quasiprobability density due to the over-completeness of the coherent states, meaning that

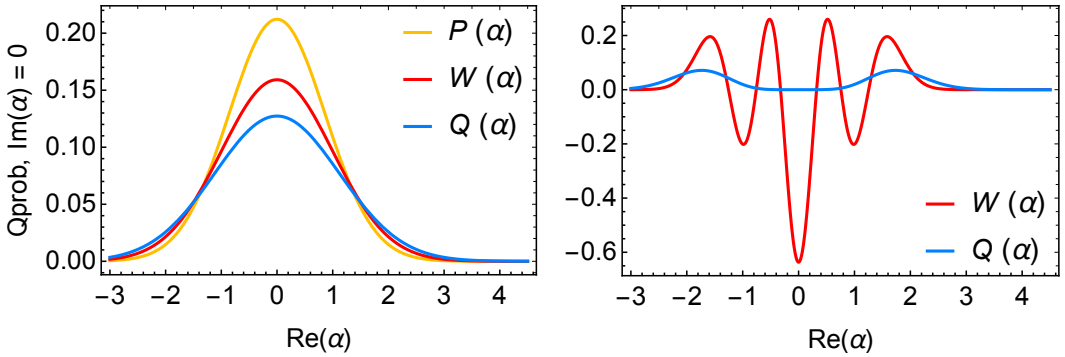

Figure 2.5: Two examples of different quasiprobabilities for two different states, both plots are cross sections viewed into the $\mathrm{Im}(\alpha) = 0$ plane, *not* marginal distributions. LEFT: phase space distributions for a thermal state with $\bar{n} = 1.5$. P, W and Q are all shown here as $P(\alpha)$ is analytic for the classical thermal state. RIGHT: W and Q distributions for the three photon state. $Q(\alpha)$ is by far the easiest to calculate however it provides the largest uncertainty spread, whilst for nonclassical states it washes out salient negative regions of the corresponding Wigner function.

each point is not unique. The Q-function is associated with joint-quadrature measurements of a quantum state [73], or detector characterisation using coherent states [92, 93]. The Q-function has a broader uncertainty spread and is always positive as shown by Figure (2.5).

The Wigner function is therefore a compromise between the P or Q-functions for representing states on phase space. It is always smooth, able to accommodate negative values and related to the marginal distribution. The main motivation for phase space representation are ease of state identification and helps visualise the state in terms of its coherent amplitude or noise, as well as providing an alternative route from discrete basis calculations. The overlap of two operators can be calculated via a convolution of their characteristic or Wigner functions in phase space

$$\mathrm{tr}\left(\hat{O}_1\hat{O}_2\right) = \pi^{-N}\int_{\mathbb{C}^N} d^{2N}\xi\, \chi_{\hat{O}_1}(\xi)\chi_{\hat{O}_2}(-\xi) = \pi^{N}\int_{\mathbb{C}^N} d^{2N}\alpha\, W_{\hat{O}_1}(\alpha)W_{\hat{O}_2}(\alpha), \tag{2.102}$$

where the characteristic and Wigner function of the operators are denoted as

$\chi_{\hat{O}_1}(\xi)$ and $W_{\hat{O}}$. The integration is over a complex plane for each mode, where $d^2\xi \equiv d\mathrm{Re}(\xi)d\mathrm{Im}(\xi)$.

2.3.2 Mean Vector & Covariance Matrix

The Gaussian states are conveniently characterized by their first and second statistical moments [46, 59, 65, 94], instead of infinite-sum number basis expansions. Through this continuous variable formalism, a single-mode density matrix is mapped onto a 2-dimensional vector and 2×2 matrix; N-modes therefore map onto a $2N$-dimensional vector and $2N \times 2N$ matrix. The first moment is the mean

$$\mu = \langle \hat{\mathrm{x}} \rangle, \qquad \hat{\mathrm{x}} := \{\hat{q}_1, \hat{p}_1, \ldots, \hat{q}_N, \hat{p}_N\}^T, \tag{2.103}$$

denoted as μ. These are the expectation values of the quadrature operators arranged pairwise in a vector $\hat{\mathrm{x}}$. The second moment, the covariance matrix, is a $2N \times 2N$ matrix with entries

$$\Sigma_{kl} = \tfrac{1}{2} \langle \hat{\mathrm{x}}_k \hat{\mathrm{x}}_l + \hat{\mathrm{x}}_l \hat{\mathrm{x}}_k \rangle - \mu_k \mu_l, \tag{2.104}$$

with $k, l \in [1, 2N]$ as the k-th and l-th elements in vector $\hat{\mathrm{x}}$. The diagonals of the covariance are the position and momentum variance of each mode in the global state, whereas the off-diagonals show the intramode or intermode quadrature correlations.

Composite density matrices are formed by tensor product on Hilbert space – this translates to direct sums of moments on phase space

$$\hat{\rho}_a \otimes \hat{\rho}_b \to \mu_a \oplus \mu_b, \ \Sigma_a \oplus \Sigma_b. \tag{2.105}$$

The partial trace is performed by reduction of the dimensions of the first and second moments, by deletion of all entries associated with the traced-out mode

$$\hat{\rho}_b = \mathrm{tr}_a(\hat{\rho}_{a,b}) \to \mu_b, \Sigma_b. \tag{2.106}$$

Only quadratures operators from the same mode possess a non-zero commutation relation $[\hat{q}_k, \hat{p}_l] = i\delta_{kl}$ (the scaling is still in "natural units" where $\hbar = 1$).

The global commutation relation is therefore compactly summarised by

$$[\hat{\mathrm{x}}_k, \hat{\mathrm{x}}_l] = i\Omega_{kl}, \tag{2.107}$$

where Ω_{kl} are the elements of the symplectic form matrix

$$\Omega = \bigoplus_{k=1}^{N} \omega, \qquad \omega = \begin{pmatrix} 0 & 1 \\ -1 & 0 \end{pmatrix}, \tag{2.108}$$

in block-diagonal form. The symplectic matrix Ω is also used for imposing the positivity condition on the covariance matrix

$$\Sigma + i\Omega/2 \geq 0, \tag{2.109}$$

hence the eigenvalues of the covariance matrix must remain positive semi-definite.

The characteristic and Wigner functions of Gaussian states can be expressed in non-integral form using the mean vector and covariance matrix

$$\chi(\Lambda) = e^{-\frac{1}{2}\Lambda^T \Sigma \Lambda + i\Lambda^T \mu}, \tag{2.110}$$

$$W(X) = \left(\pi^N \sqrt{\det \Sigma}\right)^{-1} e^{-\frac{1}{2}(X-\mu)^T \Sigma^{-1}(X-\mu)}, \tag{2.111}$$

similarly to multivariate Gaussian densities in mathematics [68, 85]. The expressions have been converted to Cartesian coordinates of real numbers instead of complex parameters that exist in eqs. (2.94) and (2.95) by setting

$$\xi = \tfrac{1}{\sqrt{2}}(a + ib), \qquad \alpha = \tfrac{1}{\sqrt{2}}(q + ip), \tag{2.112}$$

such that a, b, q and $p \in \mathbb{R}$. The integrals over complex phase space also acquire an additional factor $1/2$ per mode due to the conversion

$$\int_{\mathbb{C}^N} d^{2N}\xi = \frac{1}{2^N} \int_{\mathbb{R}^{2N}} d^{2N}\Lambda, \qquad \int_{\mathbb{C}^N} d^{2N}\alpha = \frac{1}{2^N} \int_{\mathbb{R}^{2N}} d^{2N}X, \tag{2.113}$$

with parameters $\Lambda = \{a_1, b_1, \ldots, a_N, b_N\}, X = \{q_1, p_1, \ldots, q_N, p_N\}$ as vectors of real numbers. As an example, the normalisation of the density matrix can be checked via

$$\mathrm{tr}(\hat{\rho}) = \left((2\pi)^N \sqrt{\det \Sigma}\right)^{-1} \int_{\mathbb{R}^{2N}} d^{2N}X \, e^{-\frac{1}{2}(X-\mu)^T \Sigma^{-1}(X-\mu)} = 1, \tag{2.114}$$

that requires the Gaussian integral identity

$$\int_{\mathbb{R}^{2N}} d^{2N}X\, e^{-\frac{1}{2}(X-\mu)^T\Sigma^{-1}(X-\mu)} = (2\pi)^N\sqrt{\det\Sigma}. \tag{2.115}$$

This example demonstrates again that the displacement is a linear shift on phase space – it does not alter the Gaussian shape of the Wigner function, and μ does not appear in the solution after integration.

For two different N-mode Gaussian states $\hat{\rho}_0$ and $\hat{\rho}_1$, the overlap in terms of the mean vector and covariance matrix is found through the convolution integral eq. (2.102), using the Gaussian characteristic functions

$$\mathrm{tr}(\hat{\rho}_0\hat{\rho}_1) = (2\pi)^{-N}\int_{\mathbb{R}^{2N}} d^{2N}\Lambda\, e^{-\frac{1}{2}\Lambda^T(\Sigma_0+\Sigma_1)\Lambda+i\Lambda^T(\mu_0-\mu_1)}, \tag{2.116}$$

to perform the integral requires the following identity

$$\int_{\mathbb{R}^N} d^{2N}\Lambda\, e^{-\frac{1}{2}\Lambda^T\Sigma\Lambda+i\Lambda^T\mu} = \frac{(2\pi)^N}{\sqrt{\det\Sigma}}e^{-\frac{1}{2}\mu^T\Sigma^{-1}\mu}, \tag{2.117}$$

which leads to

$$\mathrm{tr}(\hat{\rho}_0\hat{\rho}_1) = \frac{1}{\sqrt{\det(\Sigma_0+\Sigma_1)}}e^{-\frac{1}{2}(\mu_0-\mu_1)^T(\Sigma_0+\Sigma_1)^{-1}(\mu_0-\mu_1)}. \tag{2.118}$$

The same expression can also be derived using the Wigner function, however this adds another layer of complexity, having to simplify the inverse matrix relations inside the exponential terms.

2.3.3 Moments of Gaussian States

Thermal States

The moments of the thermal state are derived using the quadrature mean variances for a thermal state stated in eq.(2.59)

$$\mu_{th} = 0, \qquad \Sigma_{th} = (\bar{n}+\tfrac{1}{2})\mathbb{1}_2, \tag{2.119}$$

or by using the density matrix expression in eq. (2.56) to calculate expectation values of the operators in eqs.(2.103) and (2.104). On phase space it is a zero-mean state (the expression "$\mu_{th} = 0$" here is simply shorthand for the zero mean

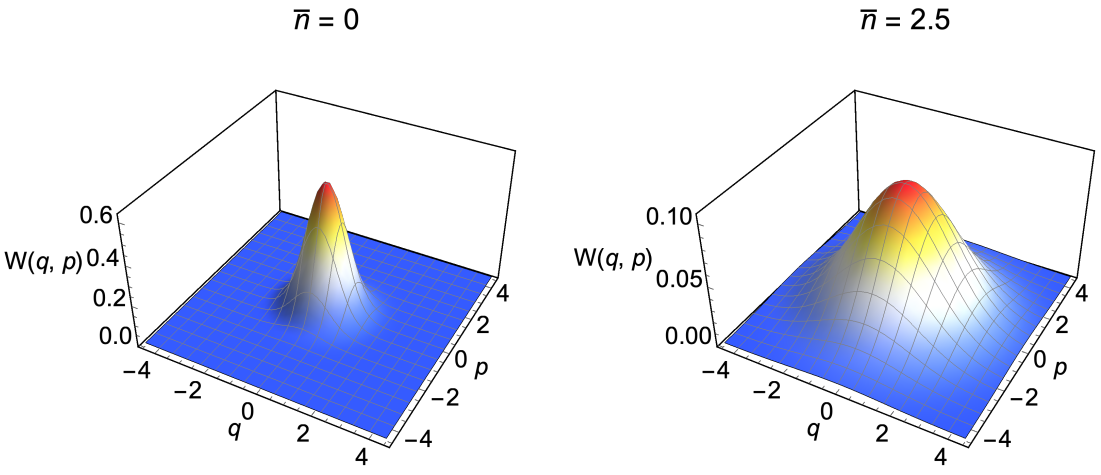

Figure 2.6: Wigner functions of thermal states: for $\bar{n} = 0$, the vacuum state is a narrow Gaussian peak in phase space centred at the origin, with variance limited by quantum shot noise. Increase in mean number of thermal photons broadens the Wigner function and the amplitude is flattened out (note the change in scaling on z-axis for $\bar{n} = 2$). As both state have zero mean, the covariance matrix alone is enough to characterise the state.

vector $\{0, 0\}^T$), that has equal variance in the q and p axes, in agreement with expectation and variance of the electric field operator in eqs. (2.58) and (2.59). Increasing the mean number of photons broadens the thermal Wigner function.

The vacuum state moments are obtained for $\bar{n} = 0$

$$\mu_0 = 0, \qquad \Sigma_0 = \tfrac{1}{2}\mathbb{1}_2, \tag{2.120}$$

and essentially shows the quantum shot noise limit for both quadratures.

Coherent States

The moments of the coherent state are

$$\mu_\alpha = \sqrt{2}\left\{\mathrm{Re}(\alpha), \mathrm{Im}(\alpha)\right\}^T, \qquad \Sigma_\alpha = \tfrac{1}{2}\mathbb{1}_2, \tag{2.121}$$

as $\alpha = \mathrm{Re}(\alpha) + i\,\mathrm{Im}(\alpha)$ is an overall complex displacement, which may be decomposed into a displacement amplitude and angle. The $\sqrt{2}$ factor arises due to the scaling of the quadratures – for example

$$\langle \hat{q} \rangle = \tfrac{1}{\sqrt{2}}(\alpha + \alpha^*) = \sqrt{2}\mathrm{Re}(\alpha). \tag{2.122}$$

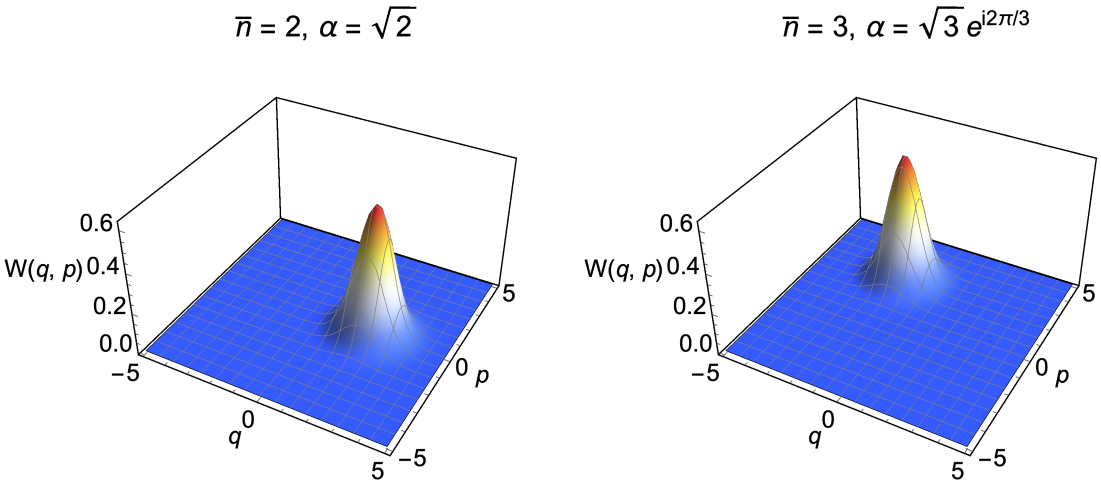

Figure 2.7: Wigner functions of coherent states: both examples show displacement of the vacuum state from the origin of the phase space to the coordinate specified by the complex displacement parameter α.

For μ_α in terms of the mean photon number:

$$\mu_\alpha = \sqrt{2\bar{n}}\{\cos\theta, \sin\theta\}^T, \tag{2.123}$$

made by substitution of $\bar{n} = |\alpha|^2$. θ is the displacement angle.

Examples of coherent states are shown in Figure 2.7. Note that the covariance is the same as the vacuum state, meaning that displacing a state does not change the noise distribution of the state and only shifts the centre of fluctuations to a new coordinate on phase space. The overall evolution of the coherent state orbits the phase space origin anti-clockwise, and projects an oscillating distribution onto a certain phase angle ϕ.

Single-Mode Squeezed Vacuum

The single-mode squeezed vacuum, with zero squeezing phase, has the following moments

$$\mu_r = 0, \qquad \Sigma_r = \begin{pmatrix} \frac{1}{2}e^{-2r} & 0 \\ 0 & \frac{1}{2}e^{2r} \end{pmatrix}, \tag{2.124}$$

which is in accordance with eqs. (2.80) and (2.81). The eigenvalues of the covariance matrix show the variance along the q axis is squeezed and that of p is

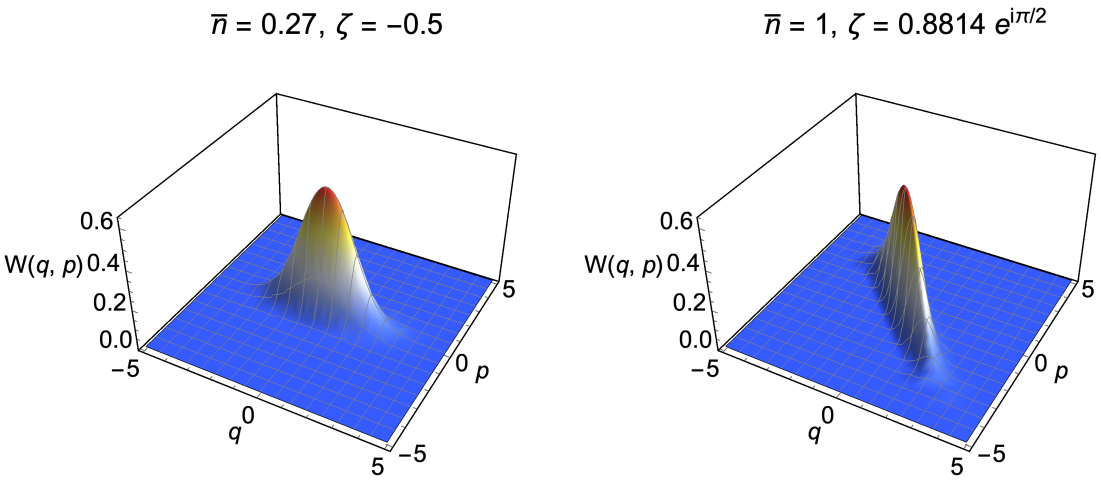

Figure 2.8: Wigner functions of the single mode squeezed vacuum, showing the variance of a Gaussian distribution reduced along one axis. Example on the left show that a "negative" value of squeezing means squeezing phase set at π, due to this, the semi-minor axis of the squeezing ellipse is parallel to angle $\varphi/2$ anti-clockwise from the q-axis. Example on the right show a larger squeezing amplitude, leading to a flatter Gaussian, with a squeezing angle $\varphi = \pi/2$.

anti-squeezed, via an exponential function of r. The squeezed vacuum, similar to a regular vacuum, is zero-mean.

In terms of mean photon number

$$\Sigma_r = \begin{pmatrix} (2(\sqrt{\bar{n}} + \sqrt{1+\bar{n}})^2)^{-1} & 0 \\ 0 & \bar{n} + \frac{1}{2} + \sqrt{\bar{n}(1+\bar{n})} \end{pmatrix}, \tag{2.125}$$

made by substitution of $\bar{n} = \sinh^2 r$. The product of the covariances give $1/4$.

Two-Mode Squeezed Vacuum

The two mode squeezed vacuum has larger covariance matrix, incorporating the quadratures of both modes exhibiting inter-mode quadrature correlations. Ex-

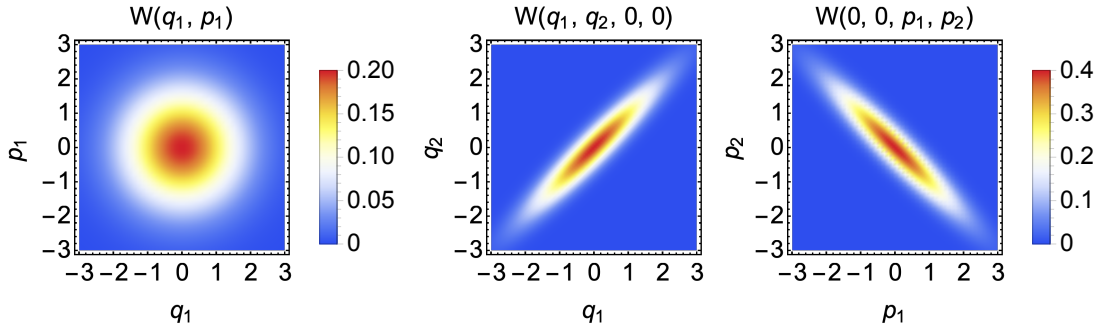

Figure 2.9: Density plots of Wigner functions for TMSV with $r = 0.8814, \bar{n} = 1$. As the TMSV is a multimode state, only two variables can be plotted to see the Wigner function. The single plot on the left shows the Wigner function of the remaining thermal state after partial tracing of the TMSV. The pair of density plots on the right show quadrature correlations, at cross sections where $p_1 = p_2 = 0$ or $q_1 = q_2 = 0$, shared by both modes (note axes labels). Two identical thermal states cannot produce this type of quadrature correlation.

pressed in terms of mean photon number, the moments of TMSV are

$$\mu_{TMSV} = 0, \qquad \Sigma_{TMSV} = \begin{pmatrix} \bar{n}+1/2 & 0 & \sqrt{\bar{n}(1+\bar{n})} & 0 \\ 0 & \bar{n}+1/2 & 0 & -\sqrt{\bar{n}(1+\bar{n})} \\ \sqrt{\bar{n}(1+\bar{n})} & 0 & \bar{n}+1/2 & 0 \\ 0 & -\sqrt{\bar{n}(1+\bar{n})} & 0 & \bar{n}+1/2, \end{pmatrix}, \tag{2.126}$$

where $\bar{n} = \sinh^2 r$ is the mean photon number of a single-mode. If this state is partially traced, by deletion of the third and fourth row and column, then the covariance matrix is that of a thermal state. The off-diagonal elements show quadrature correlations $\langle \hat{q}_1 \hat{q}_2 \rangle$ and $\langle \hat{p}_1 \hat{p}_2 \rangle$ between the two modes – positively correlated for position and negatively correlated the momentum, for $\varphi = 0$. In Figure 2.9, the effects of squeezing in both modes can be seen in the density plots, which are Wigner functions where quadratures have been set to zero e.g. $p_1 = p_2 = 0$ or $q_1 = q_2 = 0$, in order to show the squeezing of quadratures, as the

Wigner function at such coordinates are

$$W(q_1, q_2, 0, 0) \propto e^{-\frac{1}{2}(q_1^2+q_2^2)(\bar{n}+\frac{1}{2})-4q_1q_2\sqrt{\bar{n}(1+\bar{n})}}, \tag{2.127}$$

$$W(0, 0, p_1, p_2) \propto e^{-\frac{1}{2}(p_1^2+p_2^2)(\bar{n}+\frac{1}{2})+4p_1p_2\sqrt{\bar{n}(1+\bar{n})}}, \tag{2.128}$$

which plots a Gaussian ellipse due to the cross correlation terms $-4q_1q_2\sqrt{\bar{n}(1+\bar{n})}$ and $4p_1p_2\sqrt{\bar{n}(1+\bar{n})}$.

2.3.4 Symplectic Transforms

Gaussian unitary transformations become symplectic transformation matrices on phase space [46, 59, 94–96]. The symplectic matrices, denoted here as "S", are derived from factorising out the coefficients after evolving the quadrature operators under a Gaussian unitary. For example, the symplectic transform for the single-mode squeezing operator is derived by first evolving the annihilation operator

$$\hat{a}' = \hat{S}^\dagger(\zeta)\hat{a}\hat{S}(\zeta) = \hat{a}\cosh r - \hat{a}^\dagger e^{i\varphi}\sinh r. \tag{2.129}$$

This can be done by using the following operator theorem [70]

$$e^{\hat{x}}\hat{y}e^{-\hat{x}} = \hat{y} + [\hat{y}, \hat{x}] + \tfrac{1}{2!}[\hat{y}, [\hat{y}, \hat{x}]] + \tfrac{1}{3!}[\hat{y}, [\hat{y}, [\hat{y}, \hat{x}]]] + \ldots. \tag{2.130}$$

The position and momentum operators evolve as

$$\hat{q}' = \hat{q}(\cosh r - \cos\varphi\sinh r) - \hat{p}\sin\varphi\sinh r, \tag{2.131}$$

$$\hat{p}' = \hat{q}(\cosh r + \cos\varphi\sinh r) - \hat{q}\sin\varphi\sinh r, \tag{2.132}$$

which can be collected into a single matrix equation $\hat{\mathrm{x}}' = \mathrm{S}_\zeta \mathrm{x}$ by writing the quadrature operators as a vector and the transformation coefficients as a matrix

$$\mathrm{S}_\zeta = \begin{pmatrix} \cosh r - \cos\varphi\sinh r & -\sin\varphi\sinh r \\ -\sin\varphi\sinh r & \cosh r + \cos\varphi\sinh r \end{pmatrix}, \tag{2.133}$$

is therefore the symplectic transform matrix for the single mode squeeze operator. As for two-mode squeezing, the operator (2.88) acts on both modes

$$\hat{a}' = \hat{S}_2^\dagger(\zeta)\hat{a}\hat{S}_2(\zeta) = \hat{a}\cosh r - \hat{b}^\dagger e^{i\varphi}\sinh r, \tag{2.134}$$

$$\hat{b}' = \hat{S}_2^\dagger(\zeta)\hat{b}\hat{S}_2(\zeta) = \hat{b}\cosh r - \hat{a}^\dagger e^{i\varphi}\sinh r, \tag{2.135}$$

so the following can be derived as

$$\mathrm{S}_{2,\zeta} = \begin{pmatrix} \cosh r & 0 & -\cos\varphi\sinh r & -\sin\varphi\sinh r \\ 0 & \cosh r & -\sin\varphi\sinh r & \cos\varphi\sinh r \\ -\cos\varphi\sinh r & -\sin\varphi\sinh r & \cosh r & 0 \\ -\sin\varphi\sinh r & \cos\varphi\sinh r & 0 & \cosh r \end{pmatrix}. \quad (2.136)$$

By finding the symplectic transform corresponding to a particular Gaussian unitary – instead of evolving the density matrix directly via $\hat{\rho}' = \hat{U}\hat{\rho}\hat{U}^\dagger$ – on phase space simply evolve the moments using the symplectic transforms

$$\mu' = \mathrm{S}\mu + d_\alpha, \qquad \Sigma' = \mathrm{S}\Sigma\mathrm{S}^T. \quad (2.137)$$

The additional term $d_\alpha = \sqrt{2}\left\{\mathrm{Re}(\alpha), \mathrm{Im}(\alpha)\right\}^T$ is a result of applying a displacement operation, which does not alter the covariance matrix but only shifts the mean vector of the Gaussian state to a new position $\mu + d$. The process is also reversible: if there is an arbitrary covariance matrix Σ, then symplectic diagonalization is able to factor it into N-thermal states that have undergone symplectic transforms

$$\Sigma = \mathrm{S}\Sigma^{\oplus}\mathrm{S}^T, \quad (2.138)$$

where

$$\Sigma^{\oplus} = \mathrm{diag}(\nu_1, \nu_1, \ldots, \nu_N, \nu_N), \quad (2.139)$$

is a diagonal matrix with repeated (symplectic) eigenvalues ν_k and is named the "Williamson form" [95]. The symplectic eigenvalues of a two-mode covariance matrix are

$$\nu_\pm = \sqrt{\frac{\Delta \pm \sqrt{\Delta^2 - 4\det\Sigma}}{2}}, \quad (2.140)$$

where the factor $\Delta = \det A + \det B + 2\det C$; A, B, C are the 2×2 sub-block matrices of

$$\Sigma = \begin{pmatrix} A & C \\ C & B \end{pmatrix}. \quad (2.141)$$

The symplectic eigenvalues $\nu_\pm$ show the possibility of a larger and smaller eigenvalue if the two-mode state consists of thermal states with differing mean photon numbers such that

$$\Sigma^{\oplus} = \mathrm{diag}(\nu_-, \nu_-, \nu_+, \nu_+). \quad (2.142)$$

This demonstrates again that Gaussian states are thermal states transformed by additional Gaussian unitaries, which translates into symplectic transforms on phase space. In the case of $N = 2$, the global symplectic transform is derived by

$$\mathrm{S} = \begin{pmatrix} \sqrt{\frac{a+b+\sqrt{y}}{2\sqrt{y}}} & 0 & \sqrt{\frac{a+b-\sqrt{y}}{2\sqrt{y}}} & 0 \\ 0 & \sqrt{\frac{a+b+\sqrt{y}}{2\sqrt{y}}} & 0 & -\sqrt{\frac{a+b-\sqrt{y}}{2\sqrt{y}}} \\ \sqrt{\frac{a+b-\sqrt{y}}{2\sqrt{y}}} & 0 & \sqrt{\frac{a+b+\sqrt{y}}{2\sqrt{y}}} & 0 \\ 0 & -\sqrt{\frac{a+b-\sqrt{y}}{2\sqrt{y}}} & 0 & \sqrt{\frac{a+b+\sqrt{y}}{2\sqrt{y}}} \end{pmatrix}, \tag{2.143}$$

where $y = a^2 + b^2 - 4c^2$, and a, b, c are the elements of the symplectic matrix in "standard form"

$$\mathrm{S} = \begin{pmatrix} a & 0 & c & 0 \\ 0 & a & 0 & c \\ c & 0 & b & 0 \\ 0 & c & 0 & b \end{pmatrix}, \tag{2.144}$$

which is always achievable from a general covariance matrix, through a series of symplectic transforms of local and global squeezing, as well as local and global rotation operations [46, 94].

In addition, the symplectic matrix S must satisfy a couple of identities:

$$\mathrm{S}\Omega\mathrm{S}^T = \Omega, \qquad \det \mathrm{S} = 1. \tag{2.145}$$

The symplectic group here is related to the special orthogonal matrix group.

Single & Two-Mode Rotation Operators

Despite not being highlighted in the previous section, the rotation operator is a Gaussian unitary – single-mode rotation can either correspond to free evolution of the state, or a deliberate phase shift of the state. The two-mode rotation describes a linear mixing process which occurs on a beamsplitter or an interferometer. Rotation, unlike displacement or squeezing, is a photon conserving process and does not alter the energy of the state.

The single mode rotation unitary is

$$\hat{R}(\phi) = e^{i\phi\hat{a}^\dagger\hat{a}}, \tag{2.146}$$

with angle ϕ. Evolution of the annihilation operator gives

$$\hat{a}' = \hat{R}(\phi)^\dagger_\phi \hat{a} \hat{R}(\phi) = \hat{a}(1 + i\phi - \phi a^2/2! + i\phi^3/3! + \ldots) = \hat{a}e^{i\phi}. \tag{2.147}$$

The phase factor then transfers onto evolved quadrature operators, which can then be factored out as

$$\mathrm{S}_\phi = \begin{pmatrix} \cos\phi & -\sin\phi \\ \sin\phi & \cos\phi \end{pmatrix}, \tag{2.148}$$

which is an anti-clockwise rotation with respect to the positive q-axis on the Cartesian plane. As the displacement and single-mode squeezing both contain phase factors, their respective symplectic transforms can be decomposed into an amplitude transform and then a rotation transform.

The two-mode rotation unitary is

$$\hat{R}_2(\phi) = e^{i\phi(\hat{a}^\dagger \hat{b} - \hat{a}\hat{b}^\dagger)}, \tag{2.149}$$

and the derivation process of the symplectic transform remain similar to the previous examples, except that $\hat{\mathrm{x}}$ contains two pairs of quadrature operators. The symplectic matrix corresponding to the two-mode rotation is

$$\mathrm{S}_\phi = \begin{pmatrix} \cos\phi & 0 & \sin\phi & 0 \\ 0 & \cos\phi & 0 & -\sin\phi \\ \sin\phi & 0 & \cos\phi & 0 \\ 0 & -\sin\phi & 0 & \cos\phi \end{pmatrix}, \tag{2.150}$$

where ϕ can be treated as a mixing angle of a beamsplitter with variable transmissivity $\kappa = \cos^2\phi$, so that

$$\mathrm{S}_\kappa = \begin{pmatrix} \sqrt{\kappa} & 0 & \sqrt{1-\kappa} & 0 \\ 0 & \sqrt{\kappa} & 0 & -\sqrt{1-\kappa} \\ \sqrt{1-\kappa} & 0 & \sqrt{\kappa} & 0 \\ 0 & -\sqrt{1-\kappa} & 0 & \sqrt{\kappa} \end{pmatrix}. \tag{2.151}$$

The beamsplitter is used later in the quantum illumination model and optics in general to model the coupling of two modes. For example, the two-mode squeezed vacuum may be generated by mixing two single mode squeezed vacua,

with equal squeezing amplitude but orthogonal squeezing angles, together on a 50:50 beamsplitter [11]

$$\Sigma_{TMSV} = \mathrm{S}_{\kappa=1/2}(\Sigma_r \oplus \Sigma_{-r})\mathrm{S}^T_{\kappa=1/2}. \tag{2.152}$$

2.4 Discussion

Four main important Gaussian states were presented in this chapter using discrete and continuous variable basis representation. They are important resource states useful for modelling different types of signals in later chapters.

From simple photon absorption and emission processes in the quantum harmonic oscillator – the general single-mode Gaussian state is a combination of three distinct effects: thermalisation, displacement and squeezing. For a single-mode, the most general Gaussian state is

$$\hat{\rho} = \hat{D}(\alpha)\hat{S}(\zeta)\hat{\rho}_{th}\hat{S}^\dagger(\zeta)\hat{D}^\dagger(\alpha), \tag{2.153}$$

namely, the displaced squeezed thermal state. It has a mean photon number of

$$\bar{n} = \bar{n}_{th}\cosh(2r) + \sinh^2 r + |\alpha|^2, \tag{2.154}$$

$\bar{n}_{th}$ being the amount of thermal state photons [77]. The moments of this state are

$$\mu = \mathrm{S}_\theta d_{|\alpha|}, \qquad \Sigma = \mathrm{S}_{\varphi/2}\mathrm{S}_r\Sigma_{th}\mathrm{S}_r^T\mathrm{S}_{\varphi/2}^T, \tag{2.155}$$

which can be summarized by 5 parameters: thermal photon number $\bar{n}_{th}$; displacement amplitude $|\alpha|$; displacement angle ϕ; squeezing amplitude r and squeezing angle φ. If the thermal photon number equals zero, then the displaced squeezed vacuum is obtained, which is the most general minimum uncertainty Gaussian state. Each effect is feasible and controllable in experimental optics [46]: phase shifts can be executed through electronic optical modulators, linear mixing occurs in beamsplitters, and squeezing is produced from optical parametric amplifiers. Displacement is either generated from the laser itself, or by mixing with a coherent state on a beamsplitter.

The two-mode squeezed vacuum has also been highlighted in this section, as it is an important example of entangled Gaussian state (some examples where the TMSV violates Bell's theorem are available in refs. [97, 98]). In theory, the extension of displacement and thermalisation can extend onto the two-mode squeezed vacuum e.g. displaced two-mode squeezed vacuum etc. but thermalisation and displacement are factorisable quantities for $N > 1$ modes. A two-mode displaced state, or a two-mode thermal state are factorisable, and do not increase the amount of nonclassical correlations between two systems, therefore they cannot offer any more quantum enhancement. TMSV is the simplest example of an entangled two-mode Gaussian state for a given mean photon number $\bar{n}$.

Through the phase space formalism, states of the quantum harmonic oscillator may be visualised in terms of a joint quasiprobability density such as the Wigner function. Nonclassical states such as photon number states have negative Wigner functions, although this is only a sufficient condition as the squeezed states are nonclassical yet have positive Wigner functions. Phase space methods are important analytical tools and offers an alternative route for calculation of expectation values. This turns out to be useful in a computational setting, where N-mode Gaussian states, that have infinite-sum expansions in the photon number basis, are represented by $2N$-dimensional vector and a $2N \times 2N$ matrix instead of a d^N matrix (d as the dimension of the state vector or density matrix). However, both continuous variable or discrete formalisms contains limitations in analysis – for example, the beamsplitter transform is easier to carry out in phase space, but photocounting is more efficiently computed using number state expansions of the state. Familiarity with both representations are therefore useful for statistical analysis involving photons or bosons in general.

Chapter 3

Quantum State Discrimination

Quantum state discrimination in quantum information, through calculating various discrimination metrics, attempts to quantify the difference between different quantum states, which informs us of the preparation of the quantum state. In this thesis I focus only on binary state discrimination.

If states are representations of a physical field then quantum state discrimination theory is applicable to physical signals. Some of the common measures used in quantum state discrimination often stem from classical discrimination theory of distributions [1, 99–101], generalised to density matrices. State discrimination is crucial for quantum hypothesis testing which are then applied to models such as quantum sensing [102], quantum reading [43] and quantum illumination [2, 30, 31, 103].

Broadly speaking, there are two main classes of discrimination measures: *distance* and *overlap*. Both measures output a number between zero and one that quantify distinguishability between two density matrices: $\hat{\rho}_0$ and $\hat{\rho}_1$. The measures are related to bounds on the probability of error when deciding between such two states: distance usually denotes the difference

$$\text{distance} \propto \hat{\rho}_0 - \hat{\rho}_1, \tag{3.1}$$

whereas overlap denotes the trace over a product

$$\text{overlap} \propto \text{tr}(\hat{\rho}_0 \hat{\rho}_1). \tag{3.2}$$

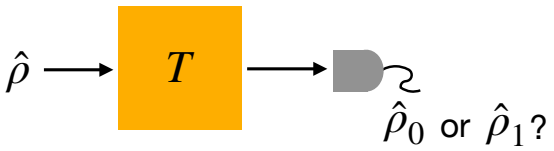

Figure 3.1: State discrimination as hypothesis testing.

Both can be used to measure density matrices or functions of density matrices. A distance value of 1 or an overlap of 0 would imply perfect discrimination achievable only by orthogonal states [4], and vice-versa for identical states.

Let's imagine two density matrices, $\hat{\rho}_0$ and $\hat{\rho}_1$, that represent conditional outcomes of a hypothesis which aims to determine whether a signal $\hat{\rho}$ has undergone transformation T or not, shown Figure 3.1. Hence the two possible outcomes are

$$H_0 : \hat{\rho}_0, \tag{3.3}$$

$$H_1 : \hat{\rho}_1 = T(\hat{\rho}). \tag{3.4}$$

If we have sent signal $\hat{\rho}$, then outcome of discrimination will tells us about the process T, whereas $\hat{\rho}_0$ would indicate signal loss (we are simply measuring the environment state). We can use this information to decide whether the transformation has happened, or not, to our signal. Even with ideal detection, there will persist a probability of error if the conditional hypothesis states are not orthogonal. Calculation of the discrimination measure then allows us then to estimate the success or error probability of this measurement process.

To help discriminate between conditional hypothesis states we have to perform a measurement on the output. For a simple example: assume a binary detector, which has two measurement outcomes $0, 1$, each represented by the following positive operators

$$\hat{\pi}_0, \qquad \hat{\pi}_1 = \mathbb{1} - \hat{\pi}_0. \tag{3.5}$$

Together, the set $\{\hat{\pi}_0, \hat{\pi}_1\}$ form a positive operator value measure (POVM). If $\hat{\pi}_0$ outputs the correct result for $\hat{\rho}_0$, and $\hat{\pi}_1$ for $\hat{\rho}_1$, then the total success probability per shot is

$$p_s = p_0 \operatorname{tr}(\hat{\pi}_0\hat{\rho}_0) + p_1 \operatorname{tr}(\hat{\pi}_1\hat{\rho}_1), \tag{3.6}$$

and the error probability is

$$p_e = p_0 \operatorname{tr}(\hat{\pi}_1 \hat{\rho}_0) + p_1 \operatorname{tr}(\hat{\pi}_0 \hat{\rho}_1), \tag{3.7}$$

such that $p_e + p_s = 1$. The error probability is the weighted sum of the incorrect outcomes, shown by the mismatched indices on the operators in the trace bracket. The attached prior probabilities, $p_0 \equiv p(H_0)$ and $p_1 \equiv p(H_1)$, are those associated with the respective hypothesis. These are set up as $p_0 = p_1 = 1/2$ to model feigned ignorance.

The measurement outcomes can be more explicitly defined as conditional probabilities where

$$\operatorname{tr}(\hat{\pi}_i \hat{\rho}_j) = p(i|H_j), \tag{3.8}$$

is the conditional probability of measuring $\hat{\pi}_i$ under hypothesis H_j, $i, j \in \{0, 1\}$. The error probabilities then occur when $i \neq j$, and success probabilities are when $i = j$. The error probability in eq. (3.7) is the sum of both type-I and type-II errors [99]: type-I being the 'false-positive" probability

$$p(1|H_0) = \operatorname{tr}(\hat{\pi}_1 \hat{\rho}_0), \tag{3.9}$$

which is outcome $\hat{\pi}_1$ for the null hypothesis. The type-II error is then the "false-negative" probability

$$p(0|H_1) = \operatorname{tr}(\hat{\pi}_0 \hat{\rho}_1), \tag{3.10}$$

which is when $\hat{\pi}_0$ happens under the alternate hypothesis. Then for minimum error discrimination there are degrees of freedom in choosing different measurements or different states to minimise the error probability.

3.1 The Helstrom Bound

The Helstrom bound provides the absolute theoretical minimum bound on the error probability in the context of discriminating two quantum states a single measurement [99]. It is a distance-based discrimination measure. I shall present two derivations of the Helstrom bound from the error probability to its textbook definitions [4, 99] and discuss its uses on different states.

The derivation of the Helstrom bound follows directly from the error probability in eq. (3.7), where by substituting in equal prior probabilities and expanding in terms of $\hat{\pi}_1$ gives

$$p_e = \tfrac{1}{2}[\mathrm{tr}(\hat{\pi}_1\hat{\rho}_0) + \mathrm{tr}(\hat{\pi}_0\hat{\rho}_1)], \tag{3.11}$$

then by substitution of $\hat{\pi}_0 = \mathbb{1} - \hat{\pi}_1$ we have

$$p_e = \tfrac{1}{2}\left[1 - \mathrm{tr}(\hat{\pi}_1\hat{\rho}_1 - \hat{\pi}_1\hat{\rho}_0)\right]. \tag{3.12}$$

In order to minimise p_e, the expression inside the trace bracket must be maximised: the degree of freedom here is to choose a POVM operator (a form of measurement) which maximises the difference between the conditional hypotheses. However, the matrix

$$\hat{\gamma} := \hat{\rho}_1 - \hat{\rho}_0, \tag{3.13}$$

known as the Helstrom matrix, has trace zero, meaning that it contains negative eigenvalues which do not correspond to physical observables. In order to maximise $\mathrm{tr}(\hat{\pi}_1\hat{\gamma})$, the operator $\hat{\pi}_1$ must project onto the spanned subspace of $\hat{\gamma}$ that contains positive eigenvalues [4, 99, 104]. Spectral decomposition of $\hat{\gamma}$ gives

$$\mathrm{tr}(\hat{\pi}_1\hat{\gamma}) = \sum_k \lambda_k \langle\lambda_k|\hat{\pi}_1|\lambda_k\rangle, \tag{3.14}$$

where λ_k are the matrix eigenvalues corresponding to eigenstate $|\lambda_k\rangle\langle\lambda_k|$. The positive projection requires the following

$$\langle\lambda_k|\hat{\pi}_1|\lambda_k\rangle = 1, \qquad \lambda_k \geq 0, \tag{3.15}$$

$$\langle\lambda_k|\hat{\pi}_1|\lambda_k\rangle = 0, \qquad \lambda_k < 0, \tag{3.16}$$

indicating that, the optimum distinguishing measurement operator is simply

$$\hat{\pi}_1 = \sum_k |\lambda_k\rangle\langle\lambda_k|, \qquad \lambda_k > 0, \tag{3.17}$$

because negative eigenvalues do not represent physical outcomes of a measurement. Thus, the sum of the positive eigenvalues of $\hat{\gamma}$ gives the Helstrom bound: another method is through using the Jordan decomposition [105, 112] of a self-adjoint operator

$$\hat{\gamma} = \hat{\gamma}_+ - \hat{\gamma}_-, \tag{3.18}$$

which breaks the Helstrom matrix into its positive and negative parts, with

$$\hat{\gamma}_+ := \tfrac{1}{2}\left(|\hat{\gamma}| + \hat{\gamma}\right), \qquad \hat{\gamma}_- := \tfrac{1}{2}\left(|\hat{\gamma}| - \hat{\gamma}\right), \tag{3.19}$$

and $|\hat{\gamma}| = \sqrt{\hat{\gamma}^\dagger \hat{\gamma}}$. As the optimum measurement only picks out the positive part of the matrix, the negative part vanishes, hence

$$\mathrm{tr}(\hat{\pi}_1 \hat{\gamma}) = \mathrm{tr}(\hat{\gamma}_+) = \tfrac{1}{2}\,\mathrm{tr}\,|\hat{\gamma}| = \tfrac{1}{2}\|\hat{\gamma}\|_1. \tag{3.20}$$

with $\|\hat{\gamma}\|_1 = \mathrm{tr}\,|\hat{\gamma}|$ as the trace-norm. Substitution of eq. (3.20) into eq. (3.12) and expanding back into density matrices gives

$$p_{e,min} = \tfrac{1}{2}\left[1 - \tfrac{1}{2}\|\hat{\rho}_1 - \hat{\rho}_0\|_1\right], \tag{3.21}$$

which is the well-known form of the Helstrom bound expressed using the trace-distance

$$\mathcal{D}(\hat{\rho}_0, \hat{\rho}_1) := \tfrac{1}{2}\|\hat{\rho}_1 - \hat{\rho}_0\|_1. \tag{3.22}$$

The trace-distance quantifies the distinguishability between two quantum states, it is a quantum generalization of the classical statistical distance [4, 106]

$$\mathcal{D}(p, q) = \tfrac{1}{2}\sum_i |p_i - q_i|, \tag{3.23}$$

where p and q are elements of classical probability distributions. The limits of the trace-distance are zero for identical states and one for orthogonal states, hence the absolute error equals, respectively, $1/2$ and zero. The Helstrom bound is difficult to achieve experimentally because it requires exact mapping of the state density matrix, hence in some 2-dimensional systems, some available schemes are detailed in refs. [22, 107, 108].

The Helstrom bound for two general pure states: $\hat{\rho}_0 = |\psi\rangle\langle\psi|$ and $\hat{\rho}_1 = |\phi\rangle\langle\phi|$ is related to the overlap $\langle\psi|\phi\rangle$. For the general solution it is useful to define

$$|\phi\rangle = \cos\theta\,|\psi\rangle + \sin\theta\,|\psi\rangle^\perp, \tag{3.24}$$

in terms of a basis of $\{|\psi\rangle, |\psi\rangle^\perp\}$ such that $\langle\psi|\phi\rangle = \cos\theta$. The Helstrom matrix is therefore

$$\hat{\gamma} = \begin{pmatrix} 1 - \cos^2\theta & \sin\theta\cos\theta \\ -\sin\theta\cos\theta & -\sin^2\theta \end{pmatrix}. \tag{3.25}$$

The eigenvalues are thus $-\sin\theta$ and $\sin\theta$, which leads to the general solution for pure states

$$p_{e,min} = \tfrac{1}{2}\left(1 - \sqrt{1 - |\langle\psi|\phi\rangle|^2}\right). \tag{3.26}$$

For two coherent states of amplitudes α and β, the bound is

$$p_{e,min} = \tfrac{1}{2}\left(1 - \sqrt{1 - e^{-|\alpha-\beta|^2}}\right), \tag{3.27}$$

using the expression for coherent states from eq. (2.72). This is the lowest error bound achievable for a single-shot, optimal measurement of two coherent states with different amplitudes. For two coherent states with equal amplitudes but π-phase difference, the Helstrom bound is

$$p_{e,min} = \tfrac{1}{2}\left(1 - \sqrt{1 - e^{-4|\alpha|^2}}\right), \tag{3.28}$$

which is achievable via Dolinar's method [109, 110].

Two classical thermal states with mean photon numbers $\bar{n}_0$ and $\bar{n}_1$ will have the following Helstrom bound

$$p_{e,min} = \tfrac{1}{2}\left(1 - \tfrac{1}{2}\sum_{n=0}^{\infty}\left|\tfrac{1}{1+\bar{n}_1}\left(\tfrac{\bar{n}_1}{1+\bar{n}_1}\right)^n - \tfrac{1}{1+\bar{n}_2}\left(\tfrac{\bar{n}_2}{1+\bar{n}_2}\right)^n\right|\right), \tag{3.29}$$

which is like the trace-distance between two classical probability distributions given by eqn. (3.23).

Between a thermal state and a coherent state, the Helstrom bound is

$$p_{e,min} = \tfrac{1}{2}\left(1 - \left\|\sum_{n=0}^{\infty}\tfrac{1}{1+\bar{n}}\left(\tfrac{\bar{n}}{1+\bar{n}}\right)^n|n\rangle\langle n| - |\alpha\rangle\langle\alpha|\right\|_1\right), \tag{3.30}$$

which cannot be reduced to a simple analytical form.

For general Gaussian states, a complete analytical expression does not exist for the trace-distance in terms of mean and covariance matrices so far, hence for distinguishability proofs that involve general or Gaussian quantum states the Helstrom bound must be evaluated numerically, or by approximating it using error bounds derived from overlap-based measures.

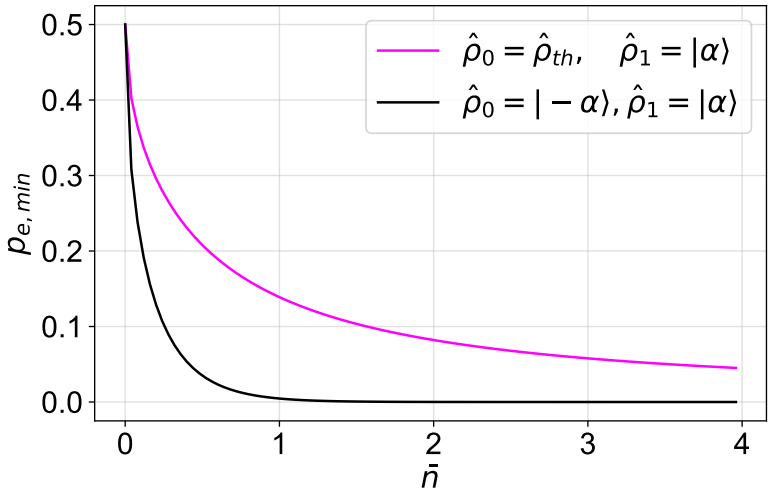

Figure 3.2: Numerical calculations of the Helstrom bounds in eqs. (3.28) and (3.30). The error probability decreases as mean photon number $\bar{n}$ increases because the photon statistics of the states differ more. A coherent state is therefore more distinguishable from a π-phase shifted coherent state, compared to a thermal state. This is due to the increase in displacement on phase space causing both states to displace in opposing directions, decreasing the overlap of their Wigner functions, whereas a thermal state spreads in uncertainty in all directions.

3.2 Overlap-Based Error Bounds

3.2.1 Fidelity

A commonly employed overlap-based measure is the quantum fidelity [100, 111]

$$\mathcal{F}(\hat{\rho}_0, \hat{\rho}_1) = \mathrm{tr}\left(\sqrt{\sqrt{\hat{\rho}_0}\hat{\rho}_1\sqrt{\hat{\rho}_0}}\right)^2, \tag{3.31}$$

Its classical analogue is [106]

$$\mathcal{F}(p, q) = \Big(\sum_i \sqrt{p_i q_i}\Big)^2; \tag{3.32}$$

in some literature the un-squared version of expression (3.31) is used.

The quantum fidelity differs from the standard overlap, $\mathrm{tr}(\hat{\rho}_0\hat{\rho}_1)$, as it equals one, if and only if $\hat{\rho}_0 = \hat{\rho}_1$ [100].

When one of the input states is a pure state, then an interpretation of the

fidelity is the probability of $\hat{\rho}_0$ passing a yes-no test of being the pure state $|\psi\rangle$

$$\mathcal{F}(\hat{\rho}_0, |\psi\rangle) = \langle\psi|\hat{\rho}_0|\psi\rangle\,. \tag{3.33}$$

When both states are pure, the fidelity coincides with modulus squared of the inner product

$$\mathcal{F}(|\psi\rangle\,, |\phi\rangle) = |\langle\psi|\phi\rangle|^2. \tag{3.34}$$

There is, then, a direct relation between the fidelity and the trace-distance [4, 106]

$$\mathcal{D}(|\psi\rangle\,, |\phi\rangle) = \sqrt{1 - \mathcal{F}(|\psi\rangle\,, |\phi\rangle)}. \tag{3.35}$$

This becomes an upper bound when the pure states are replaced by density operators or mixed states. The lower bound to the trace distance is

$$1 - \sqrt{\mathcal{F}} \leq \mathcal{D}. \tag{3.36}$$

Fidelity (or any overlap-based measure) therefore produces an upper and lower bound on the Helstrom bound. Substitution of the fidelity bounds on the trace distance into eqn. (3.12) gives

$$p^{-}_{e,\mathcal{F}} \leq p_{e,min} \leq p^{+}_{e,\mathcal{F}}, \tag{3.37}$$

with upper and lower fidelity bounds

$$p^{+}_{e,\mathcal{F}} = \tfrac{1}{2}\sqrt{\mathcal{F}}, \qquad p^{-}_{e,\mathcal{F}} = \tfrac{1}{2}\left(1 - \sqrt{1 - \mathcal{F}}\right), \tag{3.38}$$

a result first summarized by Fuchs and de Graaf [106].

3.2.2 Quantum Chernoff Bound

The quantum Chernoff bound is another overlap-based bound that provides a tighter approximation to the Helstrom bound [74, 105, 112–114]. This result is considered important because in the asymptotic limit (large number of observations) it becomes exponentially tight to the Helstrom bound. First, there exists the so-called quantum Chernoff information

$$\mathcal{C}(\hat{\rho}_0, \hat{\rho}_1) := \min_{0<s<1} \mathrm{tr}\left(\hat{\rho}_0^s \hat{\rho}_1^{1-s}\right). \tag{3.39}$$

When minimized over $s \in [0,1]$, times by a factor of $1/2$, the (upper) quantum Chernoff bound is obtained

$$p^{+}_{e,\mathcal{C}}(\hat{\rho}_0, \hat{\rho}_1) = \tfrac{1}{2}\mathcal{C}(\hat{\rho}_0, \hat{\rho}_1). \tag{3.40}$$

When $s = 1/2$

$$p^{+}_{e,\mathcal{B}}(\hat{\rho}_0, \hat{\rho}_1) = \tfrac{1}{2}\operatorname{tr}\Big(\sqrt{\hat{\rho}_0\hat{\rho}_1}\Big), \tag{3.41}$$

is known as the upper Bhattacharyya bound [101], with

$$\mathcal{B} = \operatorname{tr}\Big(\sqrt{\hat{\rho}_0\hat{\rho}_1}\Big), \tag{3.42}$$

is the Bhattacharyya information which is simpler to compute as no minimization process is required, and is also useful to approximate the Chernoff bound when two states are very similar [74]. But in general, it is less tight compared to the quantum Chernoff bound which is shown by Fig. 3.3. For example, when one of the states is pure, then the Chernoff and Bhattacharyya information become

$$\mathcal{C}(\hat{\rho}_0, |\psi\rangle) = \langle\psi|\hat{\rho}_0^s|\psi\rangle\,, \qquad \mathcal{B}(\hat{\rho}_0, |\psi\rangle) = \langle\psi|\sqrt{\hat{\rho}}|\psi\rangle\,, \tag{3.43}$$

immediately $s = 1$ minimizes the Chernoff information. The upper Chernoff bound therefore is equivalent to the fidelity expression eq. (3.33), whereas the upper Bhattacharyya takes on a value that is less than the square root fidelity as

$$\tfrac{1}{2}\sqrt{\langle\psi|\hat{\rho}|\psi\rangle} \geq \tfrac{1}{2}\langle\psi|\sqrt{\hat{\rho}}|\psi\rangle\,, \tag{3.44}$$

meaning that it is still tighter than the upper fidelity bound. When both states are pure

$$\mathcal{C}(|\psi\rangle\,, |\phi\rangle) = |\langle\psi|\phi\rangle|^2, \qquad \mathcal{B}(|\psi\rangle\,, |\phi\rangle) = |\langle\psi|\phi\rangle|^2, \tag{3.45}$$

both measures, along with fidelity, coincide together.

In a similar fashion to inequality chain (3.36), I can arrange the bounds on the trace-distance by the Bhattacharyya and Chernoff information as follows

$$1 - \mathcal{B} \leq 1 - \mathcal{C} \leq \mathcal{D} \leq \sqrt{1 - \mathcal{B}^2} \leq \sqrt{1 - \mathcal{C}^2}. \tag{3.46}$$

In terms of the probability of error, then the entire chain of overlap-based error bounds, including the fidelity, with respect to the Helstrom bound are as follows

$$p^{-}_{e,\mathcal{C}} \leq p^{-}_{e,\mathcal{B}} \leq p^{-}_{e,\mathcal{F}} \leq p_{e,min} \leq p^{+}_{e,\mathcal{C}} \leq p^{+}_{e,\mathcal{B}} \leq p^{+}_{e,\mathcal{F}}, \tag{3.47}$$

which define probability regions where the trace-distance exists. This is the expression for general states, but if both states are pure, then the above inequality chain collapses to

$$p_{e,min} \leq p^{+}_{e,\mathcal{F}}, \tag{3.48}$$

in which the lower overlap bounds coincides with the Helstrom bound (3.26).

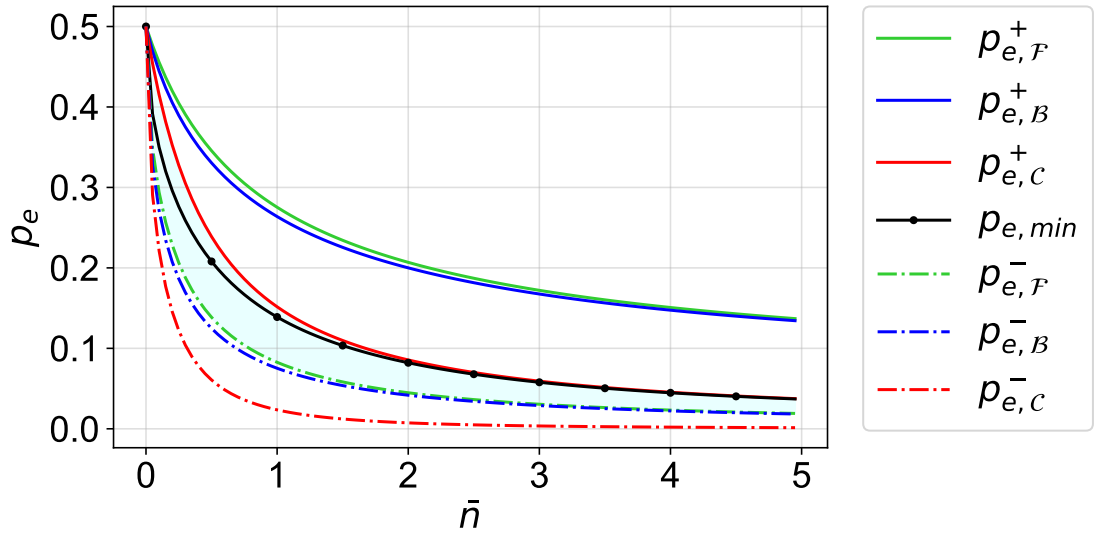

Figure 3.3: Distance vs. overlap-based error bounds in inequality (3.47) between a thermal state and a coherent state as a function of mean photon number. The decrease in the error probability indicates the two states become more distinguishable for higher mean photon numbers, this is true as the differing photon statistics become more apparent with larger mean photon numbers. The upper bounds are solid curves whereas lower bounds are dash-dot curves. The Helstrom bound (solid black line with dot overlay) is in-between the upper and lower overlap-based bounds and is approached closest from above by the upper quantum Chernoff bound, whereas from below it is achieved by the lower fidelity bound. The closest upper-lower bound approximation to the Helstrom is highlighted by the shaded region.

3.2.3 Gaussian State Expressions

To reiterate, Gaussian states can be expressed simply by their first and second statistical moments. In Gaussian quantum state discrimination, the lack of ana-

lytical expressions, in terms of statistical moments, for the Helstrom bound poses an obstacle to attaining the minimum error of discrimination for two Gaussian states. However, for fidelity and the quantum Chernoff bound, they have been solved for N-mode Gaussian states in refs. [115, 116] and [74]. I shall present them here and discuss them a little as they are used in later sections.

Fidelity

There are two separate analytical expressions for quantum fidelity of two Gaussian states, one for $N = 1$ and another for $N > 1$ [115]:

$$\mathcal{F}(\hat{\rho}_0, \hat{\rho}_1) = \frac{\mathrm{e}^{-\frac{1}{2}(\mu_0-\mu_1)^T(\Sigma_0+\Sigma_1)^{-1}(\mu_0-\mu_1)}}{\sqrt{\Delta+\Lambda}-\sqrt{\Lambda}} \qquad \text{for} \qquad N = 1, \tag{3.49}$$

$$\mathcal{F}(\hat{\rho}_0, \hat{\rho}_1) = \frac{\mathrm{e}^{-\frac{1}{2}(\mu_0-\mu_1)^T(\Sigma_0+\Sigma_1)^{-1}(\mu_0-\mu_1)}}{(\sqrt{\Gamma}+\sqrt{\Lambda})-\sqrt{(\sqrt{\Gamma}+\sqrt{\Lambda})^2-\Delta}} \qquad \text{for} \qquad N > 1, \tag{3.50}$$

where

$$\Delta := \det(\Sigma_0 + \Sigma_1), \tag{3.51a}$$

$$\Gamma := 2^{2n} \det(\Omega\Sigma_0\Omega\Sigma_1 - \mathbb{1}/4), \tag{3.51b}$$

$$\Lambda := 2^{2n} \det(\Sigma_0 + i\Omega/2) \det(\Sigma_1 + i\Omega/2). \tag{3.51c}$$

The matrix Ω is the symplectic form matrix in eq. (2.108). The exponential part of both expressions occurs frequently in overlap-based measures for Gaussian states which include displacement due to eq. (2.117) that was used to evaluate Gaussian state overlap. The two different equations for Gaussian state fidelity was unified into a single expression later by Banchi *et al* [116], albeit no less complex.

Quantum Chernoff Bound

From refs. [30, 46, 74], the following equation calculates the Chernoff information for two N-mode Gaussian states

$$\mathcal{C}(\hat{\rho}_0, \hat{\rho}_1) = \min_{0<s<1} \sqrt{\frac{\det \mathrm{G}_s(\Sigma_0, \Sigma_1)}{\det \mathrm{Z}_s(\Sigma_0, \Sigma_1)}} e^{-\frac{1}{2}(\mu_0-\mu_1)\mathrm{Z}_s^{-1}(\Sigma_0,\Sigma_1)(\mu_0-\mu_1)}, \tag{3.52}$$

where the matrices

$$\mathrm{G}_s(\Sigma_0, \Sigma_1) = g_s(\Sigma_0^{\oplus}) g_{1-s}(\Sigma_1^{\oplus}), \tag{3.53a}$$

$$\mathrm{Z}_s(\Sigma_0, \Sigma_1) = \mathrm{S}_0 z_s(\Sigma_0^{\oplus}) \mathrm{S}_0^T + \mathrm{S}_1 z_{1-s}(\Sigma_1^{\oplus}) \mathrm{S}_1^T, \tag{3.53b}$$

contain the following functions

$$g_s(\nu) = \tfrac{1}{(\nu+1/2)^s - (\nu-1/2)^s}, \tag{3.54a}$$

$$z_s(\nu) = \tfrac{1}{2} \tfrac{(\nu+1/2)^s + (\nu-1/2)^s}{(\nu+1/2)^s - (\nu-1/2)^s}, \tag{3.54b}$$

that act on the symplectic eigenvalues nu of the covariance matrix in Willamson form

$$f(\Sigma^{\oplus}) = \bigoplus_{k=1}^{N} f(\nu_k) \mathbb{1}. \tag{3.55}$$

The above expression contains slightly different values from its derivation in ref. [74], which was done for $\hbar = 2$. Note that the matrix Z_s requires the symplectic transforms which diagonalizes the covariance matrix, which, for $N = 2$ the analytical solution is derived via eqn. (2.143).

3.3 Multicopy State Discrimination

The previous discrimination measures summarised in Fig. (3.3) provide optimal estimates for error probabilities for single-shot discrimination. For multiple copies of states $\hat{\rho}_0$ and $\hat{\rho}_1$, overlap-based error bounds brings another advantage thanks to the factorizability of tensor products under the trace operation. If there are multiple copies of density matrices $\hat{\rho}_0$ and $\hat{\rho}_1$, then their respective multicopy density matrix expressions are $\hat{\rho}_0^{\otimes M}$ and $\hat{\rho}_1^{\otimes M}$, with $M > 1$ being the number of copies. In this case the Helstrom bound becomes

$$p_{e,min}^{(M)} = \tfrac{1}{2} \left(1 - \tfrac{1}{2} || \hat{\rho}_0^{\otimes M} - \hat{\rho}_1^{\otimes M} ||_1 \right), \tag{3.56}$$

which is evidently difficult to evaluate, especially for Gaussian states with infinite-sum expansions in the number basis as the dimensions of the Hilbert state space scales as as power of M, e.g. $\dim(\hat{\rho}^{\otimes M}) = N^M$. However, in terms of fidelity the multicopy error bounds are simply powers of the single copy fidelity

$$p_{e,\mathcal{F}}^{-(M)} = \tfrac{1}{2} \left(1 - \sqrt{1 - \mathcal{F}^M}\right), \qquad p_{e,\mathcal{F}}^{+(M)} = \tfrac{1}{2} \sqrt{\mathcal{F}^M}, \tag{3.57}$$

where $(\hat{\rho}^{\otimes M})^a = (\hat{\rho}^a)^{\otimes M}$, and the trace of a tensor product obeys the following [4]

$$\mathrm{tr}(A \otimes B) = \mathrm{tr}(A)\,\mathrm{tr}(B), \tag{3.58}$$

hence the multicopy version of the bound in eqn. (3.37) holds, as well as rest of the overlap-based bounds in the inequality chain eq. (3.47). For the equivalent multicopy Chernoff/Bhattacharyya bounds directly substitute the Chernoff/Bhattacharyya information into eqn. (3.57).

In the limit of many shots $M \gg 1$, the error probability will eventually decrease exponentially according to an asymptotic rate ξ [112]. This is useful for quantifying the performance of state discrimination with respect to the number of trials/shots/copies

$$\xi = \lim_{M\to\infty} -\frac{\log(p_e)}{M}. \tag{3.59}$$

In the asymptotic limit, the quantum Chernoff bound decays with the same error exponent as the Helstrom bound [105, 114].

3.4 Discussion

In this chapter two measures of state discrimination were presented, that are important for analysis of quantum illumination as hypothesis testing is useful for modelling return signal discrimination. Both measures show the probability of error in terms of the density matrix. In Figure 3.3, the error probability between distinguishing a coherent state and thermal state decreases as a nonlinear function of $\bar{n}$, showing that differences in the statistics of the states can enhance distinguishability. This model has been studied in refs. [99] and [103], as it models discrimination of a single frequency mode from thermal background noise of a similar frequency. The Helstrom bound represents the absolute error probability where the optimal measurement strategy only has two outcomes that discriminate between the null and alternative hypothesis. A sub-optimal measurement process obviously increases the discrimination error.

In multicopy state discrimination or for general Gaussian states, analytical solutions of the Helstrom bound are difficult to obtain. The main technique

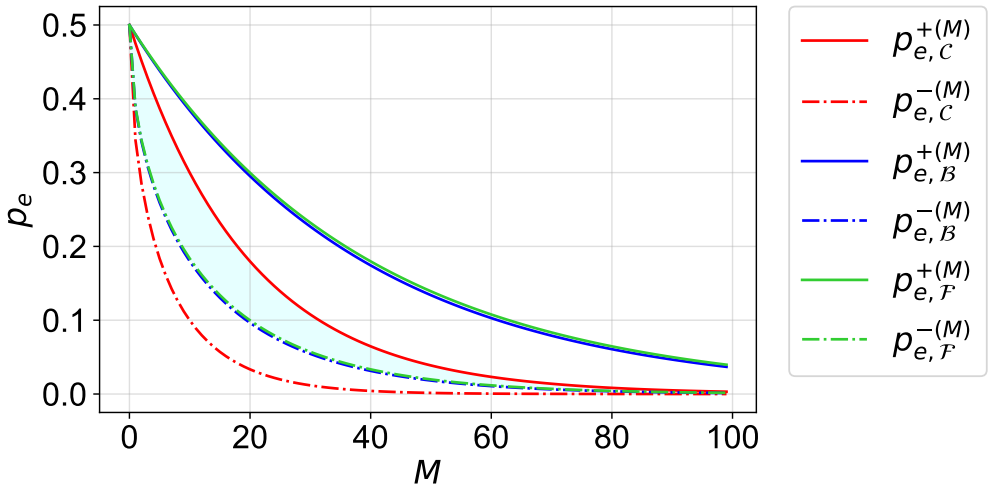

Figure 3.4: Upper and lower overlap-based error bounds for multicopy discrimination of a thermal state and a coherent state, both with mean photon number $\bar{n} = 0.05$. $\mathcal{C} = 0.950116$, which is equal to the state overlap as the coherent state is a pure state. The upper overlap exponents are: Chernoff $\xi = 0.744318$, Bhattacharyya $\xi = 0.719497$, and fidelity $\xi = 0.718733$. The computation of the Helstrom bound is not possible here due to exponential scaling of the state Hilbert space with M-shots. The shaded area show the narrowest approximation to the Helstrom bound achievable using and upper and lower overlap bound. The Helstrom bound itself is more likely exist nearer the upper Chernoff bound plot.

around this is to consider the overlap-based bounds that depend on the fidelity or quantum Chernoff information, so that for multicopy discrimination bounds simply scale as an exponential power of the number of shots. In the asymptotic limit, the error probability becomes

$$p_e \sim e^{-M\xi}, \tag{3.60}$$

where the quantum Chernoff bound decays with the same error exponent as that of the Helstrom bound.

For Gaussian states, expressions for calculating fidelity and the quantum Chernoff bound exist in terms of mean vector and covariance matrix. The drawback to using overlap-based bounds is that they do not give a direct relationship to the absolute error unless both states are pure. For general states, the closest approximation to the Helstrom bound is the (upper) quantum Chernoff bound.

Chapter 4

Quantum State Measurement

Measurement is how we extract information encoded within a quantum state. Such extracted information, however, is almost always incomplete because measurement disrupts the quantum state and carries with it other undesirable factors such as signal losses, detector inefficiencies and ambient dark noise that can affect the accuracy of the measurement outcome [4, 23, 93, 117]. The measurement of the return signals of course would constitute a crucial step in the development of quantum radar/lidar technology. In this chapter I will present a phase-insensitive method of photon detection and discuss its benefits when used with the entangled TMSV state.

In another sense, measurement of a quantum state accesses entries of the state density matrix. To obtain a more complete measurement of a quantum state, that is to say, a more complete way of "mapping out" the density matrix, usually requires a phase-sensitive technique [118]. For optical states there are techniques such as homodyne and heterodyne detection which have been inspired by their classical counterparts [119, 120]. Both require mixing into the signal a stable phase reference (local oscillator), such as a relatively large-amplitude coherent state. In balanced homodyne detection, the quantum state would be mixed with the local oscillator on a 50:50 beamsplitter. With $\hat{a}$ as the annihilation operator and α as the coherent amplitude, the number of photons at the exit ports are [119]

$$\hat{n}_3 = \tfrac{1}{2}(\hat{a}+\alpha)^\dagger(\hat{a}+\alpha), \quad \hat{n}_4 = \tfrac{1}{2}(\hat{a}-\alpha)^\dagger(\hat{a}-\alpha). \tag{4.1}$$

Subtraction of the outputs gives

$$\hat{n}_3 - \hat{n}_4 = \sqrt{2}|\alpha|\hat{x}_\phi, \tag{4.2}$$

Therefore, we can see that through counting photons, balanced homodyne detection can access the marginal distribution of the quantum state $\langle \hat{x}_\phi \rangle$ scanned at an angle ϕ relative to the local oscillator. A picture of the Wigner function can then be reconstructed up by sampling various phase angles. This process is called quantum state tomography [87, 118]. Tomography is useful for characterising novel nonclassical states [76, 88], but may not be an appropriate method for rangefinding as homodyne detection demands stability of the local oscillator, alignment and precise mode matching. Construction of the Wigner function is also unnecessary.

Phase-insensitive methods could offer a much simpler technique for detection of quantum states, which would produce results at a faster rate whilst at the expense of losing more information about the state density matrix compared to phase-sensitive methods [92]. This chapter focuses on the theory of phase-insensitive *on-off photodetection* which is a measurement scheme closely related to photocounting implemented by detectors such as avalanche-photodiodes (APDs) or photomultiplier tubes [93, 121]. I shall then extend this by analysing measurement outcomes for multiple on-off detectors arranged in a multiplexed array set-up, forming a higher resolution measurement of the quantum state [122, 123].

Two detectors measuring bipartite entangled modes will show stronger-than-classical correlations. Detection of an entangled mode is useful to herald changes in the photon number distribution of the unmeasured mode, so called "quantum state engineering" [49, 58, 61]. This conditional measurement can generate certain quantum states, providing a wider resource pool of states for quantum illumination [58, 59]. In the final section of this chapter, on-off detection is harnessed for measurement-based state engineering using the entangled TMSV.

4.1 Photocounting

The theory of photocounting stems back to Mandel and Wolf [72, 124], which stated the following semi-classical relation under the following assumptions: for a stationary light source, the probability of counting m-photons within integration time T follows a Poissonian distribution

$$p_m(t,T) = \left\langle \frac{(\eta \bar{I}(t,T)T)^m}{m!} e^{-\eta \bar{I}(t,T)T} \right\rangle, \tag{4.3}$$

where $\bar{I}(t,T)$ is the cycle-average intensity within time duration starting from t to $t+T$. The detector has quantum efficiency η, which is the percentage of photons successfully converted into detectable electrical pulses or "counts". Detectors count photons "indirectly" as the detected pulse is a cascade of electrons, initially seeded by an ionized electron ejected from the cathode by the photoelectric effect. Increasing the intensity of light, or by increasing the integration time, increases the probability of counts. The mean number of photocounts within such integration time is

$$\langle m \rangle = \langle \eta I(t,T)T \rangle, \tag{4.4}$$

as this is a property of the Poissonian distribution [72].

The quantum mechanical version of Mandel's formula was presented by Kelly and Kleiner [92, 125]

$$p_m(T) = \left\langle : \frac{(\eta \hat{a}^\dagger \hat{a})^m}{m!} e^{-\eta \hat{a}^\dagger \hat{a}} : \right\rangle, \tag{4.5}$$

where the colons denote normal ordering of operators [70]. This equation is similar to Mandel's photocounting formula, but the term for average intensity has been replaced with the photon number operator. The photocounting POVM element can be extracted from this equation through the Born rule

$$\hat{\Pi}_m(\eta) =: \frac{(\eta \hat{a}^\dagger \hat{a})^m}{m!} e^{-\eta \hat{a}^\dagger \hat{a}} : . \tag{4.6}$$

Rewriting as a differential gives

$$\hat{\Pi}_m(\eta) = \frac{(-\eta)^m}{m!} \frac{\partial^m}{\partial \eta^m} : e^{-\eta \hat{a}^\dagger \hat{a}} :, \tag{4.7}$$

which can then be expressed in the photon number basis, because the normal ordering of the exponential operator is

$$: e^{-\eta\hat{a}^\dagger\hat{a}} := \sum_{n=0}^{\infty}(1-\eta)^n \left|n\right\rangle\!\left\langle n\right|, \tag{4.8}$$

derived using operator ordering theorems [70]. Putting eqs. (4.8) and (4.7) together then differentiating gives

$$\hat{\Pi}_m(\eta) = \eta^m \sum_{n=m}^{\infty} \binom{n}{m} (1-\eta)^{n-m} \left|n\right\rangle\!\left\langle n\right|. \tag{4.9}$$

This operator represents the outcome of m-photons measured by an n-photon resolving detector, to which all possible combinations of m are included in the POVM summation. The summation picks out $n = m$ as the binomial coefficient vanishes for $n < m$. It is binomial because m-photons cause the detector to fire with probability η^m, meaning that there are $\binom{n}{m}$ possible combinations with no-count probability $(1-\eta)^{n-m}$.

4.2 On-Off Detection

4.2.1 One Detector

The "click" detector is an on-off, Geiger counter style photodetector that only has two possible outcomes – it either fires or does not – dependent on the non-vacuum or vacuum probability of the quantum state photon number distribution [59, 92, 93]. Any radiation which falls within the detection bandwidth of the click detector will trigger it. It also cannot distinguish between a single photon or multiple photons very well because it fires if there are one, two, ... or n photons. Multiple photons will only increase the probability of a single click because there is a restricted number of outcomes. The relation between click detection and photon number resolving detection can be derived by infinite summation of eq. (4.9) starting from $m = 1$.

As there can only be two outcomes, on-off detection contains only two POVM elements: the "no-click" operator has the same expression as eq. (4.8) [59, 70, 93]

$$\hat{\Pi}_{N=1,k=0}(\eta) = \sum_{n=0}^{\infty}(1-\eta)^n \left|n\right\rangle\!\left\langle n\right|, \tag{4.10}$$

which for unit quantum efficiency equates to projection onto the vacuum state. The "click" operator is the matrix complement of the no-click operator

$$\hat{\Pi}_{N=1,k=1}(\eta) = \mathbb{1} - \hat{\Pi}_{N=1,k=0}(\eta) = \sum_{n=0}^{\infty}(1-(1-\eta)^n) \left|n\right\rangle\!\left\langle n\right|, \tag{4.11}$$

with indices attached to the operator indicating the number of click detectors, N, and the number of clicks, k, it represents (this notation is useful for subsequent sections). The expectation value of an operator $\hat{\Pi}_{N,k}$ outputs the probability $p_N(k)$ for a state. For example, $\hat{\Pi}_{1,0}$ denotes the outcome "single detector, no click", which occurs with probability $p_1(0)$.

Click Probability of Single-Mode Gaussian States

As Gaussian states are be parameterised by mean photon number $\bar{n}$, the click probability is then directly relatable to the energy of the state. Using the Fock basis expansions of the single-mode Gaussian states stated in Chapter 2, we can derive the single click probability for set mean photon number: the click probability for a coherent state happens to be the most probable for any mean photon number

$$p_1(1) = 1 - e^{-\eta\bar{n}}; \tag{4.12}$$

whereas the thermal state click probability is

$$p_1(1) = 1 - \frac{1}{1+\eta\bar{n}}; \tag{4.13}$$

the single-mode squeezed vacuum is even less likely to trigger a click, with

$$p_1(1) = 1 - \frac{1}{\sqrt{1-\bar{n}\eta+2\bar{n}\eta^2}}, \tag{4.14}$$

and this forms a lower bound on click probability in the class of single-mode Gaussian states. There are no phase terms in the above expressions, because on-off detection only accesses the photon number distribution of a state.

For general single-mode Gaussian states, the click probability in terms of μ and Σ are derived using the Gaussian convolution integral eq. (2.102). The characteristic function of the no-click operator is

$$\chi_{1,0}(\Lambda) = \frac{1}{\eta} e^{-\frac{2-\eta}{4\eta}|\Lambda|^2}, \tag{4.15}$$

which is derived by eqs. (4.10) and (2.94). The diagonal elements of the displacement operator are expressed as the following [70]

$$\langle n|\hat{D}(\Lambda)|n\rangle = e^{-\frac{1}{4}|\Lambda|^2} L_n(\tfrac{1}{2}|\Lambda|^2), \tag{4.16}$$

and to achieve eq. (4.15) requires the generating function for the Laguerre polynomials $L_n(x)$

$$\sum_{n=0}^{\infty} t^n L_n(x) = \frac{1}{1-t} e^{-\frac{tx}{1-t}}. \tag{4.17}$$

Then, the no-click probability for a single-mode Gaussian state is obtained through the integral

$$p_1(0) = \frac{1}{2\pi\eta} \int_{\mathbb{R}^2} d^2\Lambda e^{-\frac{1}{2}\Lambda^T\left(\Sigma+\frac{2-\eta}{2\eta}\mathbb{1}\right)\Lambda + i\Lambda^T\mu} = \frac{e^{-\frac{1}{2}\mu^T\left(\Sigma+\frac{2-\eta}{2\eta}\mathbb{1}_2\right)^{-1}\mu}}{\eta\sqrt{\det\left(\Sigma+\frac{2-\eta}{2\eta}\mathbb{1}_2\right)}}, \tag{4.18}$$

which requires the Gaussian integral identity in eq. (2.117). The click probability for a general single-mode Gaussian state is therefore

$$p_1(1) = 1 - \frac{e^{-\frac{1}{2}\mu^T\left(\Sigma+\frac{2-\eta}{2\eta}\mathbb{1}_2\right)^{-1}\mu}}{\eta\sqrt{\det\left(\Sigma+\frac{2-\eta}{2\eta}\mathbb{1}_2\right)}}. \tag{4.19}$$

Thermal Dark Noise

To incorporate dark noise, it is useful to visualise the imperfect click detector consisting of a hypothetical beamsplitter directly in front of a perfect click detector: the quantum efficiency is modelled by the transmissivity of the beamsplitter, as it couples a thermal background mode, acting as dark noise, with the incoming state, before detection [59, 126] (shown by Fig. 4.1). By construction, using density matrices, Born rule and the beamsplitter unitary transformation, the probability of an imperfect "no-click" outcome for an arbitary state is

$$p_1(0) = \mathrm{tr}\Big(\hat{U}_\eta \hat{\rho} \otimes \hat{\rho}_{th} \hat{U}_\eta^\dagger \mathbb{1} \otimes |0\rangle\langle 0|\Big), \tag{4.20}$$

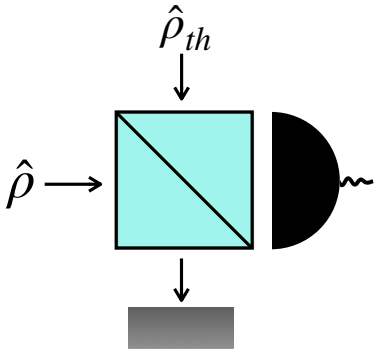

Figure 4.1: Diagram of imperfect click detection. The signal loss due to dark noise and non-unit quantum efficiency is modelled by a hypothetical beamsplitter with transmissivity η that mixes in a thermal mode before ideal detection [126].

and by using the cyclic properties of the trace, the POVM element that includes quantum efficiency and dark noise is

$$\hat{\Pi}_{1,0}(\eta, \bar{n}_{th}) = \mathrm{tr}_2\left(\hat{\rho}_{th}\hat{U}_\eta^\dagger \mathbb{1} \otimes |0\rangle\langle 0| \, \hat{U}_\eta\right). \tag{4.21}$$

This expression can be expanded by considering expanding the identity matrix in the number basis, and applying eq. (2.32) to extract the creation/annihilation operator from $|n\rangle\langle n|$. The beamsplitter unitary transforms the boson operators as follows

$$\hat{U}_\eta^\dagger \hat{a}_{in} \hat{U}_\eta = \sqrt{\eta}\hat{a}_1 + \sqrt{1-\eta}\hat{a}_2, \tag{4.22}$$

then eq. (4.21) expands to

$$\hat{\Pi}_{1,0}(\eta, \bar{n}_{th}) = \frac{1}{1+\bar{n}_{th}} \sum_{s=0}^{\infty} \left(\frac{\bar{n}_{th}}{1+\bar{n}_{th}}\right)^s \sum_{n=0}^{\infty} \binom{n+s}{s} \eta^s (1-\eta)^n \, |n\rangle\langle n| \, . \tag{4.23}$$

The thermal background mode must have its mean photon number scaled by the quantum efficiency

$$\bar{n}_{th} = \bar{n}_d/(1-\eta), \tag{4.24}$$

to ensure that mean photon number $\bar{n}_d$ is mixed into the signal such that it appears as if $\bar{n}_d$ is hitting the detector, otherwise, dark noise would be reduced by a factor $(1-\eta)$ before hitting the detector. Substituting in the scaled mean photon number gives

$$\hat{\Pi}_{1,0}(\eta, \bar{n}_d) = \frac{1}{1+\bar{n}_d} \sum_{n=0}^{\infty} \left(1 - \frac{\eta}{1+\bar{n}_d}\right)^n |n\rangle\langle n| \, . \tag{4.25}$$

4.2.2 Multiple Detectors

Multiple on-off detectors can work together to increase the photon number resolution of this phase-insensitive method. This model requires splitting the mode of radiation onto multiple on-off detectors, in a "multiplexed" scenario [61, 118, 123, 126]. An on-off detector multiplex consists of N identical detectors which measure a single mode of radiation. This can be implemented by using $2N-1$ number of splitters, either spatially via 50:50 beamsplitters, or by time-multiplexing [126, 127]. Another method is to defocus the beam onto an array of on-off detectors, as shown in Figure 4.2. In the multiplexed setup, equivalent to directing the photons into individual "bins", multiple clicks may occur simultaneously which enables quasi-photon number resolution of a quantum state.

I shall derive the Fock basis expansion of the N-detector POVM, and derive an equation for the click probability for general Gaussian states, similar to eq.(4.19) before using it for state engineering in the next section. This follows on from the work done by Sperling *et al* [61, 123] however I am simply considering the effects of a single to a few click detectors [48, 49].

The N-detector multiplex contains $N+1$ outcomes (includes the no-click outcome) – if k, $(0 \leq k \leq N)$, is the number of simultaneous clicks then there are $\binom{N}{k}$ combinations of detectors which performs this outcome

$$\hat{\Pi}_{N,k}(\eta) = \binom{N}{k} : (e^{-\frac{\eta}{N}\hat{a}^\dagger \hat{a}})^{N-k} (\mathbb{1} - e^{-\frac{\eta}{N}\hat{a}^\dagger \hat{a}})^k :, \tag{4.26}$$

assuming no dark state noise for now. For a small number of detectors, this measurement would barely achieve photon number resolution, but in the limiting case where there are large number of detectors, the click counting distribution changes from binomial to Poissonian

$$\lim_{N\to\infty} \left\langle \hat{\Pi}_{N,k}(\eta) \right\rangle = \left\langle : \frac{(\eta \hat{a}^\dagger \hat{a})^k}{k!} e^{-\eta \hat{a}^\dagger \hat{a}} : \right\rangle, \tag{4.27}$$

for large values of N under the Poisson limit theorem, becoming equivalent to the photocounting expression in eq. (4.5). Under unit quantum efficiency, k-clicks amongst a very large number of detectors is equivalent to projection onto the number state $|k\rangle\langle k|$, and reproduces the true photon number distribution

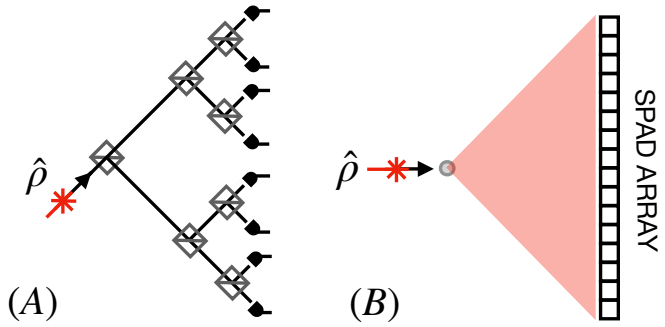

Figure 4.2: Two methods of spatial multiplexed on-off detection, where the incident field is equally distributed onto every single detector. (A) Splitter method: splitting a single-mode $\hat{\rho}$ onto $2N$-detectors via $2N-1$ number of splitters. (B) Defocussing of the beam onto a SPAD array.

of the quantum state [123]. The intensity of the input light that falls on each detector will be attenuated to such an extent that, at most, one photon would hit one detector.

Eq.(4.26) can be again expanded onto the photon number basis: applying the binomial expansion of k then collecting the exponent terms gives

$$\hat{\Pi}_{N,k}(\eta) = \binom{N}{k} \sum_{l=0}^{k} \binom{k}{l} (-1)^{k-l} : e^{-\eta(1-l/N)\hat{a}^\dagger \hat{a}} : . \tag{4.28}$$

Using eq. (4.8) to shed the normal ordering gives

$$\hat{\Pi}_{N,k}(\eta) = \binom{N}{k} \sum_{n=0}^{\infty} \sum_{l=0}^{k} \binom{k}{l} (-1)^{k-l} \left[1 - \eta\left(1 - \frac{l}{N}\right)\right]^n |n\rangle\langle n| , \tag{4.29}$$

with k as the number of clicks within N-detectors, and l as the possible combination of clicks within k-clicks. The operators form a complete set via

$$\sum_{k=0}^{N} \hat{\Pi}_{N,k}(\eta) = \mathbb{1}. \tag{4.30}$$

The characteristic function of N-detector multiplex POVM can then be derived again by using eq.(4.16) to find the diagonal elements of the displacement operator, before using the generating function in eq.(4.17) to simplify

$$\chi_{N,k}(\Lambda) = \binom{N}{k} \sum_{l=0}^{k} \frac{\binom{k}{l}(-1)^{k-l}}{\eta(1-l/N)} e^{-\frac{1}{2}|\Lambda|^2\left(\frac{2-\eta(1-l/N)}{2\eta(1-l/N)}\right)}, \tag{4.31}$$

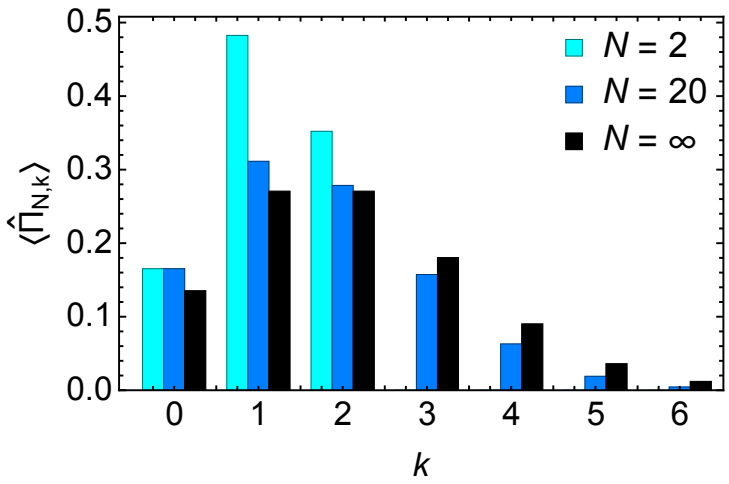

Figure 4.3: Effect of increasing the number of click detectors to approaching full photon number resolution. This example show the multi-click distribution of a coherent state of $\bar{n} = 2$, measured with detector numbers $N = 2$, $N = 20$ and $N = \infty$, which produces true photon number distribution of the coherent state.

which is similar to expression (4.15), with η becoming $\eta(1 - l/N)$, along with the binomial sum. By induction, the multi-click probability for a single-mode Gaussian state is therefore

$$p_N(k) = \binom{N}{k} \sum_{l=0}^{k} \frac{\binom{k}{l}(-1)^{k-l} e^{-\frac{1}{2}\mu^T\left(\Sigma + \frac{2-\eta(1-l/N)}{2\eta(1-l/N)}\mathbb{1}_2\right)^{-1}\mu}}{\eta(1-l/N)\sqrt{\det\left(\Sigma + \frac{2-\eta(1-l/N)}{2\eta(1-l/N)}\mathbb{1}_2\right)}}. \tag{4.32}$$

4.3 Measurement-Based State Engineering

In this section, I shall apply the POVMs derived previously to a single mode of the TMSV state to analyse state engineering using entangled states [58, 59, 61]. The measurement of a single entangled mode will break entanglement however dependent on the measurement outcome (which is probabilistic), the remaining unmeasured state will change in statics. The analysis of single click detector state engineering has been summarised in refs. [47, 48] and those for multiple click detector can be found in ref. [49]

Measurement of an entangled mode is a useful method to engineer particular quantum states. In the instance of a two-mode entangled state, the un-measured

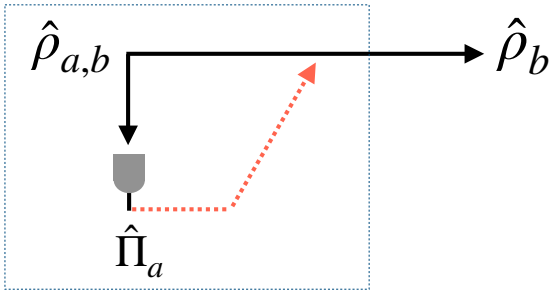

Figure 4.4: Schematic of measurement-based state engineering. Measurement outcomes of the entangled mode a conditions changes into the remaining mode b, shown by the dashed orange arrow. This is performed locally, shown by the boxed region, so that the conditioned state $\hat{\rho}_b$ is sent out.

output signal state is said to be "conditioned" or "heralded" by the measurement of the idler mode. The photon statistics of the remaining mode change after the heralding process despite having not interacted with the detector thanks to entanglement. The density matrix of the heralded state is

$$\hat{\rho}_b = \frac{\mathrm{tr}_a(\hat{\Pi}\hat{\rho}_{ab})}{\mathrm{tr}\big(\hat{\Pi}\hat{\rho}_{ab}\big)}, \tag{4.33}$$

where $\hat{\Pi} := \hat{\Pi}_a \otimes \mathbb{1}_b$ and $\hat{\rho}_{ab}$ is the joint system density matrix. Measurement of mode a leaves mode b in the above state, normalized by the probability of the measurement outcome.

Consider the following maximally entangled Bell state

$$\big|\Psi^+\big\rangle = \frac{1}{\sqrt{2}}\big(\,|0,0\rangle + |1,1\rangle\,\big), \tag{4.34}$$

where each mode contains one photon, and both are in superposition with the vacuum. Measurement of one photon by a perfect photodetector in the first mode with $\hat{\Pi} = |1\rangle\langle 1|$, will occur with probability of $1/2$, which leaves the second mode in the following state

$$\hat{\rho} = |1\rangle\langle 1|\,. \tag{4.35}$$

This very simple example can be generalised to on-off detection in order to herald single photons from the entangled two mode squeezed vacuum, which has a wavefunction of approximate form to eq. (4.34) for low-squeezing. The following

subsections provide analysis of the output states for the general case that uses TMSV with larger mean photon numbers and multiple on-off detectors – the output states, $\hat{\rho}_{N,k}$, are a set of nonclassical states which are a superposition of thermal modes.

4.3.1 One Detector

The number basis expansion of the TMSV in eq. (2.85) in terms of mean photon number per-mode, is

$$|\Psi\rangle_{i,s} = \frac{1}{\sqrt{1+\bar{n}}} \sum_{n=0}^{\infty} \left(\frac{\bar{n}}{1+\bar{n}}\right)^{n/2} |n,n\rangle\,, \tag{4.36}$$

where $\bar{n} = \sinh^2 r$. Each mode of this state contains a mean photon number of $\bar{n}$, hence for both modes it has $2\bar{n}$. The idler mode is directed towards a single on-off detector. If the detector does not fire, then the conditioned output signal mode $\hat{\rho}_{1,0}$ has the following density matrix

$$\hat{\rho}_{1,0} = \frac{1+\bar{n}_d+\bar{n}\eta}{(1+\bar{n})(1+\bar{n}_d)} \sum_{n=0}^{\infty} \left(\frac{\bar{n}}{1+\bar{n}}\left(1-\frac{\eta}{1+\bar{n}_d}\right)\right)^n |n\rangle\langle n|\,, \tag{4.37}$$

derived using eqs. (4.25), (4.33) and (4.36). The mean photon number has been reduced from $\bar{n}$

$$\bar{n}_{1,0} = \bar{n}\left(\frac{1+\bar{n}_d-\eta}{1+\bar{n}_d+\bar{n}\eta}\right) \leq \bar{n}. \tag{4.38}$$

If the idler mode triggers a click, then the conditioned output signal has the density matrix of

$$\hat{\rho}_{1,1} = \frac{1+\bar{n}\eta}{\bar{n}\eta(1+\bar{n})} \sum_{n=0}^{\infty} \left(\frac{\bar{n}}{1+\bar{n}}\right)^n \left(1+\bar{n}_d-\left(1-\frac{\eta}{1+\bar{n}_d}\right)^n\right) |n\rangle\langle n|\,, \tag{4.39}$$

which has increased mean photon number from $\bar{n}$

$$\bar{n}_{1,1} = \bar{n} + \frac{\bar{n}_d(1+\bar{n})}{\bar{n}_d+\bar{n}\eta} + \frac{(1+\bar{n})(1+\bar{n}_d)}{1+\bar{n}_d+\bar{n}\eta} \geq \bar{n}. \tag{4.40}$$

The maximum increase, caused by optimal on-off detection of the idler mode is shown by substitution of $\bar{n}_d = 0$ and $\eta = 1$ to give

$$\bar{n}_{1,1} = \bar{n} + 1, \tag{4.41}$$

hence under ideal on-off detection, the signal mode mean photon number is raised by 1 – this increase can be significant for TMSV with low squeezing as the signal gain is

$$G := \frac{\bar{n}_{1,1}}{\bar{n}} - 1 = \bar{n}^{-1}, \tag{4.42}$$

however, the trade-off is that for large gains in signal output the likelihood of heralding decreases linearly as $p_1(1) \approx \bar{n}$ for low $\bar{n}$. No-click therefore decreases the mean photon number of the signal mode, whereas a click increases its mean photon number. The gain in signal is approximately inversely proportional to the heralding click probability. This measurement-based amplification of the mean photon number of the un-measured mode is due to the photon number correlations between the two modes. By using the click outcome from the idler detector, one can post-select the results from subsequent signal mode detections.

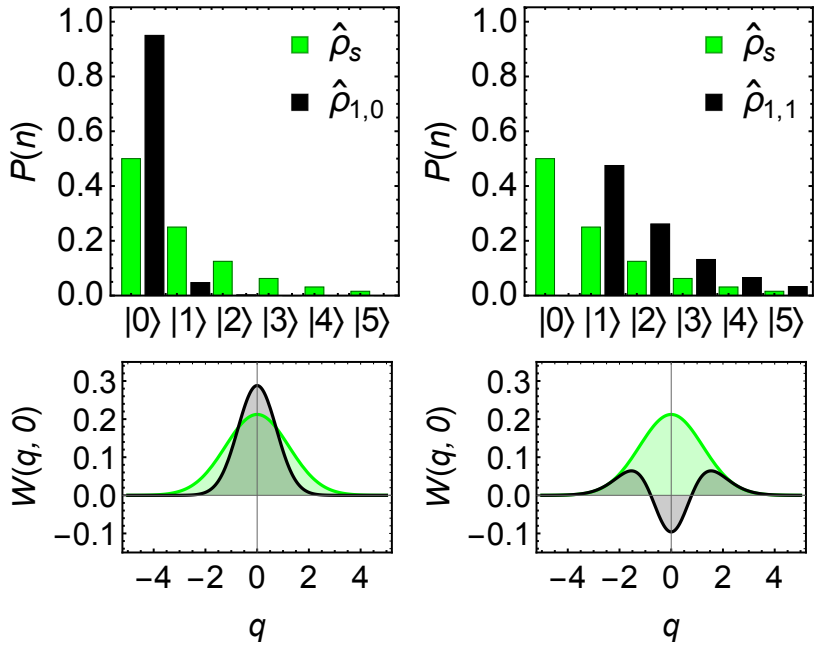

Figure 4.5: Top row: photon number distributions of the signal mode, before ($\hat{\rho}_s$) and after click detection ($\hat{\rho}_{1,0}$ and $\hat{\rho}_{1,1}$), with $\bar{n} = 1$ and $\eta = 0.9$. No-click produces state $\hat{\rho}_{1,0}$ and click produces $\hat{\rho}_{1,1}$. Bottom row: corresponding slice Wigner functions, showing the sudden change from a thermal state to either a more vacuum-like state, or a nonclassical vacuum suppressed state conditioned by the outcomes of single detector click detection.

The photon number distribution of both outcome states, as well as their pre-detection form (partial trace of the idler mode) are shown in Figure 4.5. The partial traced signal mode $\hat{\rho}_s$ is a thermal state. After a no-click outcome, $\hat{\rho}_{1,0}$ become more vacuum-like with respect to $\hat{\rho}_s$; whereas a click outcome suppresses the vacuum and amplifies the probability of higher photon numbers. If no dark noise were present, then the vacuum probability would be fully suppressed, because under the beamsplitter analogy for an imperfect on-off detector, the dark noise is a thermal state that would inject non-zero vacuum probability into the incident state.

The heralded state $\hat{\rho}_{1,1}$ is nonclassical, because it has negative Wigner function regions. It appears similar to that of a one-photon Fock state, however not entirely due to additional contributions from higher photon numbers in its photon number distribution shown in Figure 4.5. The density matrix expression in eq. (4.39) show that the state is a difference of thermal state coefficients within the mode, which implies that $\rho_{1,1}$ is also a difference of Gaussian states. The difference is translated onto phase space as negative regions, where the negativity is maximised when $\eta = 1$. Additional dark noise will wipe out this negativity, shown by Figure 4.6.

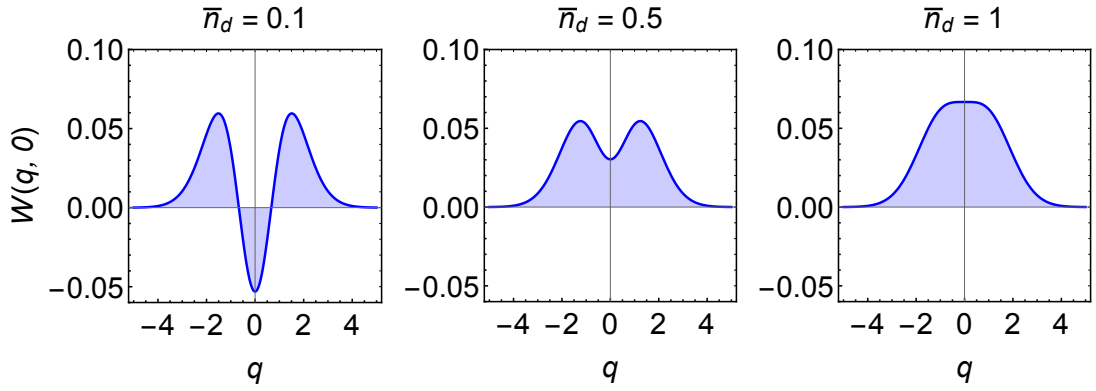

Figure 4.6: Effect of dark noise on the heralding detection: the above slice Wigner functions show the state $\hat{\rho}_{1,1}$, with $\bar{n} = 1, \eta = 0.9$ and increasing mean scaled photon number of the dark noise state. Increasing $\bar{n}_d$ is equivalent to mixing in a thermal state pre-detection. Detector noise will therefore wipe out nonclassical signatures of the heralded state.

4.3.2 Multiple Detectors

State engineering can easily extend to multiple on-off detectors, offering a richer set of detection possibilities. Multiplexed on-off detection facilitates a larger range of measurement outcomes, thus a larger set of nonclassical conditioned states also. The output state density matrix produced by detection with a multiplexed on-off detector is derived by using the POVM expression in eq. (4.29) instead of the single detector POVM. Dark noise terms have been left out for this analysis, not only for simplification but allows us to focus on the negativity and suppressed parts of the output state photon number distribution. As seen in Figure 4.6, even a mean photon number of one is enough to wipe out the nonclassicality of the quantum state.

It is useful to define an expression for the thermal state density matrix with a mean photon number value as

$$\hat{\varrho}\left[\bar{m}\right] = \frac{1}{1+\bar{m}} \sum_{n=0}^{\infty} \left(\frac{\bar{m}}{1+\bar{m}}\right)^{n} |n\rangle\langle n| \,. \tag{4.43}$$

The general output state produced from multi-click heralding on the idler mode of the TMSV, that includes quantum efficiency as a detector parameter, is

$$\hat{\rho}_{N,k} = \mathcal{N}_{N,k} \sum_{l=0}^{k} \binom{k}{l} (-1)^{k-l} (1+\bar{m}_{N,l}) \hat{\varrho}\left[\bar{m}_{N,l}\right], \tag{4.44}$$

with scaled mean photon number

$$\bar{m}_{N,l} = \frac{\bar{n} - \bar{n}\eta\left(1 - l/N\right)}{1 + \bar{n}\eta\left(1 - l/N\right)}. \tag{4.45}$$

The normalization factor

$$\mathcal{N}_{N,k} = \left[\sum_{l=0}^{k} \binom{k}{l} (-1)^{k-l} (1+\bar{m}_{N,l})\right]^{-1}, \tag{4.46}$$

is related to the heralding click probability via

$$p_N(k) = \binom{N}{k} \frac{1}{\mathcal{N}_{N,k}(1+\bar{n})}. \tag{4.47}$$

The heralding probability for detector number up to $N = 8$ are shown in Figure. 4.7. The general trend is that increase of squeezing/mean photon number increases the single and multi-click probability where all N-detectors click.

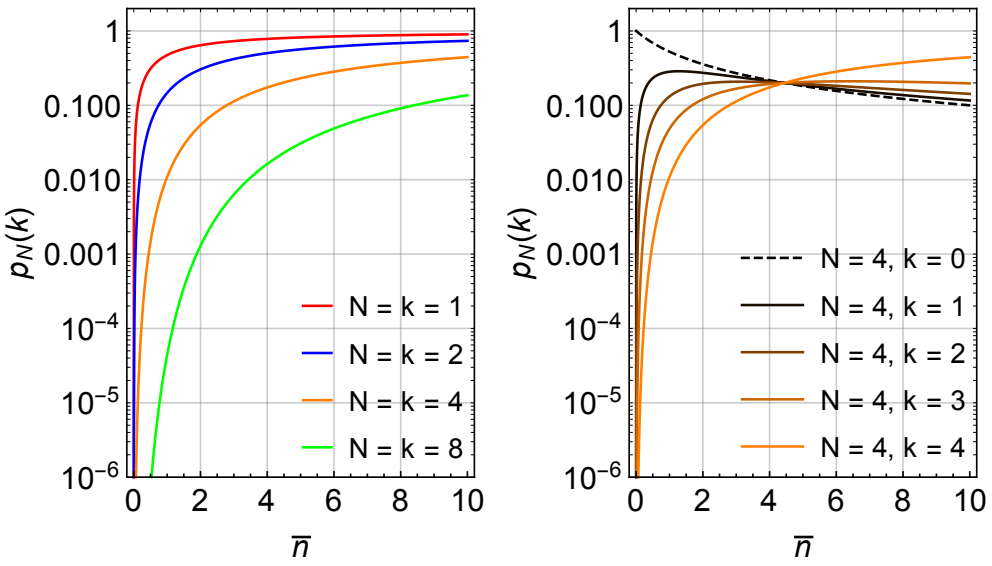

Figure 4.7: Multi-click heralding probabilities as a function of mean photon number $\bar{n}$. The detector efficiency is set at $\eta = 0.9$. Left: click probabilities where all detectors in the multiplex click. Right: click probability for all k-outcomes in a multiplex of four detectors. The intersection point occurs at $\bar{n} = N/\eta$.

However, the outcomes where $k < N$ show that there is a crossover point where all click outcomes are equally likely at $\bar{n} = N/\eta$, after which, increasing $\bar{n}$ reverses the order of relationship of the outcomes. This is possibly due to a "saturation effect", where coincidences are more likely due to bunching of the thermal state photons onto a single detector i.e. a state which has $\bar{n} = 6$ is more likely to cause a higher number of clicks for a multiplex of four detectors as $\bar{n} > N/\eta$. The single click probability even decreases for higher $\bar{n}$ values.

The multi-click heralded TMSV in eq. (4.44) are formed from a weighted binomial sum of $k + 1$ number of thermal states, $\hat{\varrho}$, with a scaled mean photon number $\bar{m}_{N,l}$, that is a function of the detector efficiency and the number of detectors. The statistics for two examples of this state generated by two clicks are shown in Figure 4.8. The photon number distributions show that multi-click heralding outputs a state with suppressed photon number probabilities up to state $|k-1\rangle$. The state tends to a number state if the number of detectors is much greater than the number of heralding clicks – an effect that can be seen by comparing the two top panels in Figure 4.8. The bottom two figures show

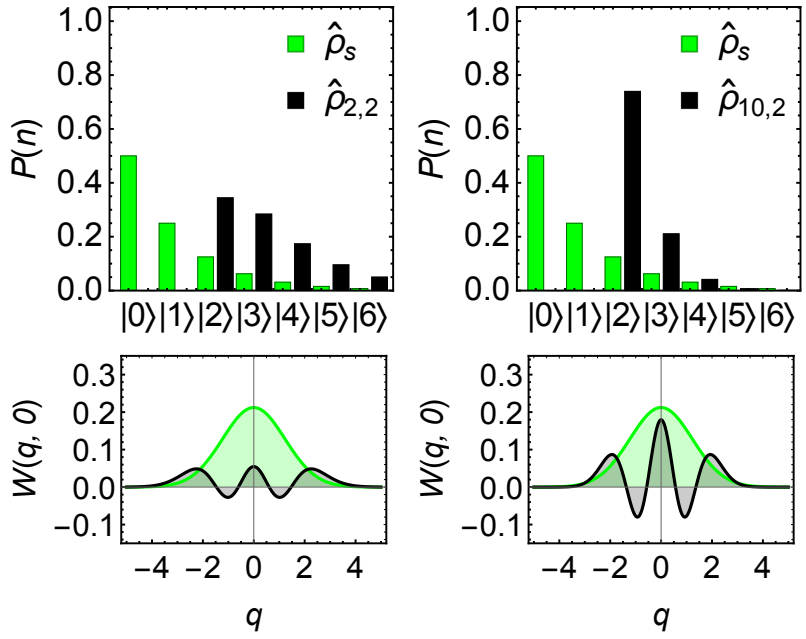

Figure 4.8: Top row: photon number distributions of the multi-click heralded TMSV output, heralded by two-clicks at the idler, compared with that of the unconditioned signal mode $\hat{\rho}_s$ with $\bar{n} = 1$ and $\eta = 0.9$. Bottom row: Wigner function slices $W(q, 0)$ of the corresponding states showing the transformation of a thermal state into a nonclassical one. Left column: $N = 2$ heralding detectors. Right column: $N = 10$ heralding detectors.

Wigner functions slices of the corresponding states, showing the transformation from a positive Gaussian of a thermal state into a nonclassical state as a result of state engineering. As a rough rule of thumb, increasing the number of detectors suppresses the higher photon number probabilities if $k < N$ (approaching to number state), whereas a click outcome for $k > 0$ fully suppresses the lower photon number probabilities up to $|k - 1\rangle$.

Similar to the one detector example, multiple on-off detection can generate a larger increase to the mean photon of the output signal mode compared to a single on-off detector. All N-detectors clicking always causes an increase to the mean photon number in signal mode, meaning that the gain is non-zero for all values of N, and this outcome produces the maximum possible increase for an N-detector multiplex. This relative increase is shown in the left plot in Figure

4.9, which is much more significant for lower $\bar{n}$. It approaches unity in the limit of higher $\bar{n}$ because k clicks would not alter the photon number distribution much: a state that has $\bar{n} = 10$ has a rather flat photon number distribution, to which a single click on the idler mode would output a signal state with a similar flat photon number distribution, with a mean photon number of $\bar{n}_{1,1} \approx 11$. Thus, the effect of heralding is less significant for TMSV with higher mean photon numbers. Looking at $k < N$, for certain values of $\bar{n}$ there results in a gain less than 1 as the detectors that do not click are really acting as photon absorbers. For example, the click outcome for $N = 4, k = 1$, caused by an idler mode with $\bar{n} = 2$, will conditions an output mode with a mean of $\bar{n}_{4,1} \approx 1$, which is 1/2 less than what it was previous to heralding. Examples of Wigner slice functions of heralded states generated with an $N = 4$ detector multiplex are shown in Figure 4.10.

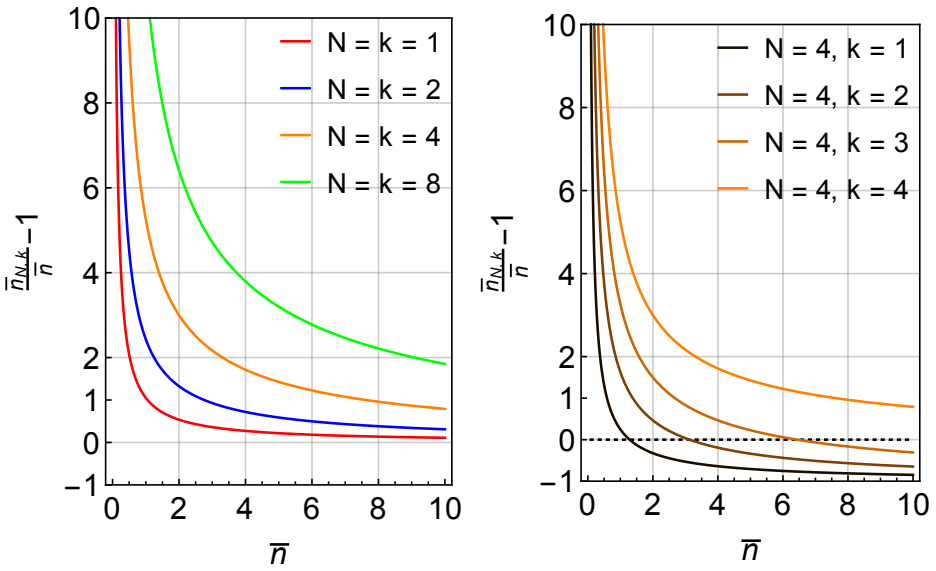

Figure 4.9: Relative gain in mean photon number of the heralded output state as a function of its pre-conditioned mean photon number $\bar{n}$. The detector efficiency is set at $\eta = 0.9$. Left: gain for states that are produced from all detectors clicking, which eventually approaches zero in the asymptotic limit for $\bar{n} \to \infty$ as heralding no longer amplify the mean photon number in the signal mode. Right: gain for states produced with an $N = 4$ detector multiplex. For $k < N$ outcomes, past a certain threshold $\bar{n}$, heralding would lead to a decrease in output mean photon number (below dashed line).

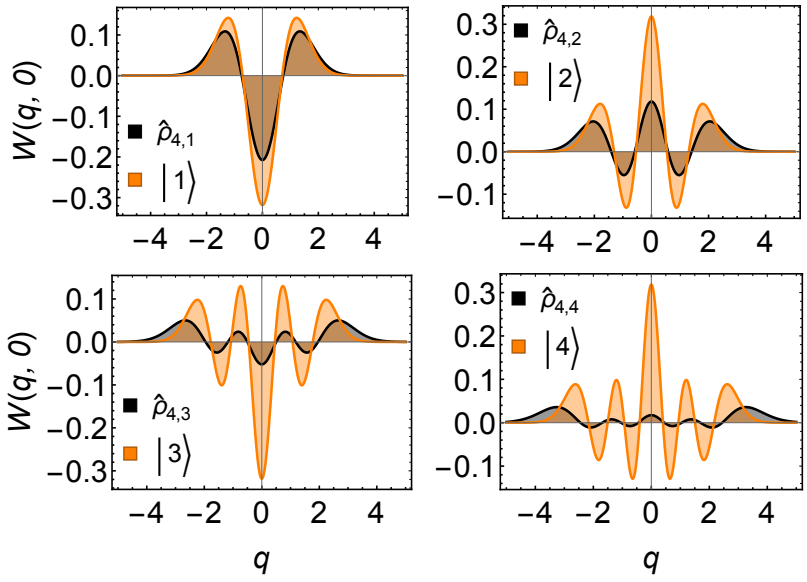

Figure 4.10: Imperfect Fock states. Wigner slice functions of Fock state $|k\rangle$ vs. multi-click heralded state $\hat{\rho}_{4,k}$. Parameters: $\bar{n} = 1$, $\eta = 0.9$.

4.4 Discussion

In practice, achieving photon number resolution is a very difficult task. A method which can produce quasi-photon number resolution is through spatial or temporal multiplexing of the on-off detection. A single detector is branched into many paths such that an incoming mode is evenly distributed into N-detectors which fire simultaneously or does not depending on the photon number distribution of the quantum state. In the limit of an infinite number of on-off detectors each simultaneous click result directly corresponds to the photon number distribution.

Detection is useful in conjunction with entanglement for measurement-based state engineering, which offers a method to probabilistically alter the photon number distribution of an entangled mode which appears classical to an observer without knowledge of both modes. The range of POVM offer a degree of freedom to condition or "engineer" a set of states based on the number of POVM elements (outcomes). A single on-off detector, measuring the idler mode of a TMSV, can condition an increase to the signal mode mean photon number. Under ideal detection, this increase is 1, which is a significant gain for weakly squeezed states with low mean photon number, although the click probability will be low – the

gain is therefore inversely proportional to the heralding probability.

Multiplexed on-off detection of the idler mode of a TMSV conditions the (initially thermal) signal mode into a nonclassical state which is a weighted binomial sum of thermal states. This new class of states have suppressed regions of photon probability distributions from the vacuum up until $|k-1\rangle$, which is a result of the sum and minus terms between the different thermal states. The cumulative effect is transferred as interference on phase space where the heralded state appear as "imperfect" number states. The statistics and properties of such multi-click heralded TMSV states can be summarized by the following assumptions based on the heralding detection outcome:

- $k = N$: the output signal mode will always have a non-zero gain in mean photon number. Although this outcome is least likely to happen unless $\bar{n} > N/\eta$, beyond which it become the most likely outcome, however the gain in the signal will not be as high as in the low mean photon regime.

- $k < N$: for $k \neq 0$ heralding clicks the output mode will have non-zero gain in mean photon number but less likely so as $\bar{n}$ increases, eventually the gain tend towards -1.

- $k \ll N$: the output signal mode very closely resembles a number state. This method is useful for generation of number states, or for achieving photon number resolution in photodetection.

- At $\bar{n} = N/\eta$, all heralding detection outcomes are equally probable, including $k = 0$.

The measurement facilitated boost is due to the direct photon number correlations of the TMSV, and is a demonstration of performance advantages that can be brought about from entanglement, which is harnessed for quantum illumination in the next chapter.

Chapter 5

Quantum Illumination & Detection

Quantum illumination (QI) is a simple model for target detection that uses quantum states, with applications in quantum radar and lidar. Whether the illumination is quantum or not depends solely on whether the signal is quantum or not, hence use of either nonclassical or entangled radiation states could fall under the umbrella definition of QI. But any indicator of performance for QI must always be compared with classical illumination (CI), more specifically, results produced by the coherent state, as a benchmark.

The process is simple: send probe radiation states towards the target or a region of interest and look for return signals. The goal is to determine whether a target is present or absent, summarised by a hypothesis testing process. Illumination can either use single or two-mode states shown by Figure 5.1 – the latter exploiting entanglement. Use of entanglement is crucial for QI, because stronger-than-classical correlations will produce detection results unattainable for classically correlated states. Higher correlations will lead to stronger signatures from noisy return signals.

As stated in the introduction, Lloyd's model of QI [2] compared performance of sending single photons versus sending an entangled d-dimensional mode of the

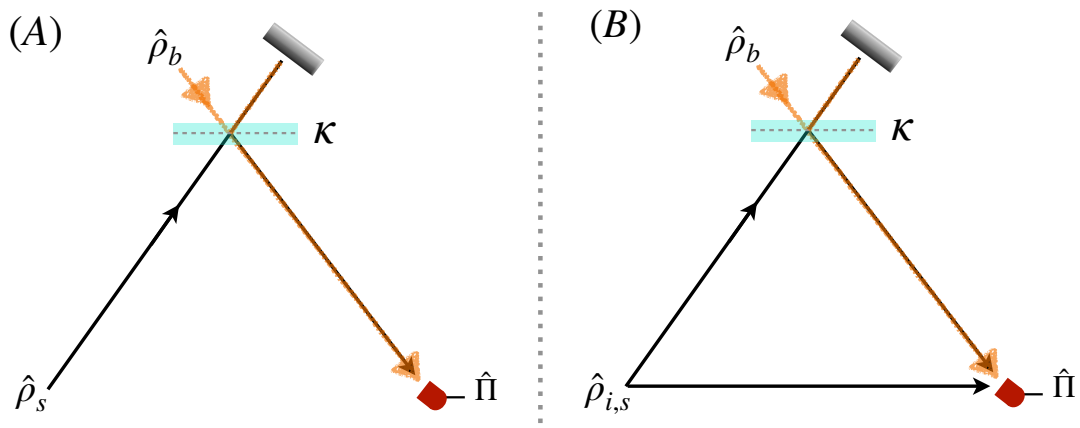

Figure 5.1: Single vs. two-mode illumination models. (A) Single mode illumination where a radiation signal state $\hat{\rho}_s$ is sent as a probe. (B) Two-mode illumination where only the signal mode of a two-mode state $\hat{\rho}_{i,s}$ is sent for target detection. The target object is modelled as a beamsplitter with reflectivity κ, which mixes the background noise mode $\hat{\rho}_b$ with $\hat{\rho}_s$. The detection of the reflected signal mode is summarized by the operator $\hat{\Pi}$.

form

$$|\Psi\rangle_{i,s} = \frac{1}{\sqrt{d}} \sum_{k=1}^{d} |k,k\rangle \,, \tag{5.1}$$

where $|k\rangle$ is the index of the detection mode which contains a single photon and none in all other detection modes. Optimal measurements on the reflected signal mode has been assumed, such that in the instance where the reflected photon contained in mode $|k\rangle$ has been detected, the background noise photon per mode, b, is reduced by the number of modes per detection event d to b/d. In order for this model to be feasible, the product $db \leq 1$ requires that at most, one noise photon is detected per trial.

The QI model for Gaussian states presented by Tan *et al.* [30] was a hypothesis testing model which incorporates state discrimination of density matrices that describe conditional states of target presence or absence, which are

$$H_0 : \hat{\rho}_0 = \text{background noise mode}, \tag{5.2}$$

$$H_1 : \hat{\rho}_1 = \text{reflected signal mode} + \text{background noise mode}. \tag{5.3}$$

Respectively, detection results either belong to target absence and presence: H_0

(null-hypothesis), or H_1 (alternate hypothesis). The general formulae to calculate these conditional states, in terms of density matrices and unitary transforms, are

$$\hat{\rho}_0 = \hat{\rho}_{th}, \tag{5.4}$$

$$\hat{\rho}_1 = \mathrm{tr}_e \left(\hat{U}_\kappa (\hat{\rho}_s \otimes \hat{\rho}'_{th}) \hat{U}_\kappa^\dagger \right), \tag{5.5}$$

for a single-mode signal state $\hat{\rho}_s$. The target-signal interaction is in $\hat{U}_\kappa$, which is the two-mode rotation operator (2.149). The low-reflecting target and background noise which contributes to signal losses is modelled by a beamsplitter with reflectivity κ embedded in a thermal background state (see Figure 5.2). The background mode is assumed to be in a thermal state $\hat{\rho}_b = \hat{\rho}_{th}$, with the apostrophe indicating that the thermal mean photon number has been be scaled according to the reflectivity

$$\bar{n}'_{th} = \bar{n}/(1-\kappa), \tag{5.6}$$

similar to eq. (4.24); the state $\hat{\rho}_1$ equals $\hat{\rho}_0$ for $\kappa = 0$. In $\hat{\rho}_1$, that is the returning state, the environment mode is traced over by tr_e (it is the discarded mode directed to the grey block in Figures 5.1 and 5.2).

For two-mode idler-signal states $\hat{\rho}_{i,s}$, the conditional states are

$$\hat{\rho}_0 = \hat{\rho}_i \otimes \hat{\rho}_{th}, \tag{5.7}$$

$$\hat{\rho}_1 = \mathrm{tr}_e \left((\mathbb{1} \otimes \hat{U}_\kappa)(\hat{\rho}_{i,s} \otimes \hat{\rho}'_{th})(\mathbb{1} \otimes \hat{U}_\kappa^\dagger) \right), \tag{5.8}$$

where $\hat{\rho}_i \equiv \mathrm{tr}_s(\hat{\rho}_{i,s})$. The state $\hat{\rho}_0$ is simply a product state between the idler (ancilla) and the background state as the signal mode has been lost. In $\hat{\rho}_1$, the idler does not interact with the object as denoted by $\mathbb{1} \otimes \hat{U}_\kappa$ which only couples the signal and background modes.

The equation for $\hat{\rho}_1$ contains the signal $\hat{\rho}_s$ which allows freedom of choice over which type of signal state to send, in order to maximise return signal detection probability. In theoretical proofs of QI [2, 30, 103], this is quantified by the error probability of $\hat{\rho}_1$ and $\hat{\rho}_0$, using the Helstrom error bounds to imply "optimal" detection. If the background state remains constant, then the error probability quantifies the performance of signal state $\hat{\rho}_s$. Quantum advantage is then demonstrated by comparing the error bounds produced by an entangled signal mode (of

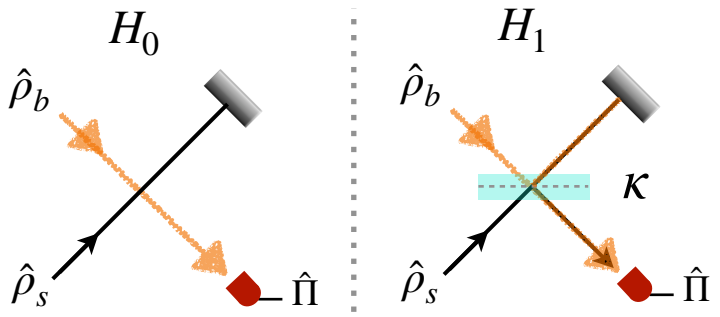

Figure 5.2: Possible scenarios of the signal mode – target absence in H_0 sees the probe signal mode $\hat{\rho}_s$ lost and the detector ends up measuring the background noise mode $\hat{\rho}_b$. Target presence in H_1 sees the target reflecting the transmitted signal mode coupled with background noise to the detector – the target essentially mixes the modes $\hat{\rho}_b$ and $\hat{\rho}_s$.

a TMSV), with that of a coherent state of equal mean photon number. This error probability based proof has analogies in classical radar threshold detection, where the two hypotheses are analogous to conditional probability distributions which model voltage outputs for a narrowband detector [1].

This chapter will present adn extend the QI model, by appending an explicit detection step using POVM operators. First, optimal measurement error bounds for single-mode and two-mode Gaussian signal states are presented. Then, the results which includes multiplexed on-off detection are presented – ultimately a non-optimum strategy. In the instance of two-mode QI, the idler state is measured first, in order to send a multi-click heralded TMSV for quantum illumination. The results show that even under low-signal intensity and high-loss regimes, heralded quantum states can generate a detectable advantage which boost the probability of detection compared to coherent states of the same energy. Finally, repeated observations using QI are modelled via a Monte-Carlo simulation of quantum illumination, which uses repeated application of posterior Bayesian probabilities to sequentially update an estimation of target presence (or absence).

5.1 Gaussian State Quantum Illumination

5.1.1 Single-Mode Signals

The conditional states generated by Gaussian signals remain Gaussian, meaning that eqs. 5.4 and 5.5 can be computed using state moments

$$\mu_0 = 0, \qquad \Sigma_0 = \Sigma_{th} = (\bar{n}_{th} + \tfrac{1}{2})\mathbb{1}_2, \tag{5.9}$$

$$\mu_1 = \mathrm{tr}_e(\mathrm{S}_\kappa\{\mu_s \oplus 0\}), \qquad \Sigma_1 = \mathrm{tr}_e(\mathrm{S}_\kappa(\Sigma_s \oplus \Sigma'_{th})\mathrm{S}_\kappa^T), \tag{5.10}$$

with S_κ being the beamsplitter symplectic transform in eq. (2.151). The moments of $\hat{\rho}_0$ remain invariant for all single-mode signals. These moments can then be substituted into quantum Chernoff bound equation (3.52) for Gaussian states, producing the upper bound to the Helstrom bound for a single shot. Note that the covariance matrix for the thermal background mode in Σ_1, is Σ'_{th}, which has the scaled mean photon number $\bar{n}_{th}/(1-\kappa)$.

Coherent State Illumination

The coherent state has the same covariance matrix as the vacuum state, however as it is displaced from the origin of the phase space it has non-zero first moments. The mean photon number is $\bar{n} = |\alpha|^2$, hence the first moment can be expressed using $\bar{n}$. The following example shall assume displacement in the q-axis

$$\mu_s = \{\sqrt{2\bar{n}}, 0\}, \qquad \Sigma_s = \mathbb{1}_2/2, \tag{5.11}$$

then the moments for the return state after target interaction are

$$\mu_1 = \{\sqrt{2\kappa\bar{n}}, 0\}, \qquad \Sigma_1 = \Sigma_{th}, \tag{5.12}$$

which has the statistics of a displaced thermal state.

Thermal State Illumination

If a thermal state is sent to illuminate a target, the returning state after target interaction would have the following moments

$$\mu_1 = 0, \qquad \Sigma_1 = (\kappa\bar{n} + \bar{n}_{th} + \tfrac{1}{2})\mathbb{1}_2. \tag{5.13}$$

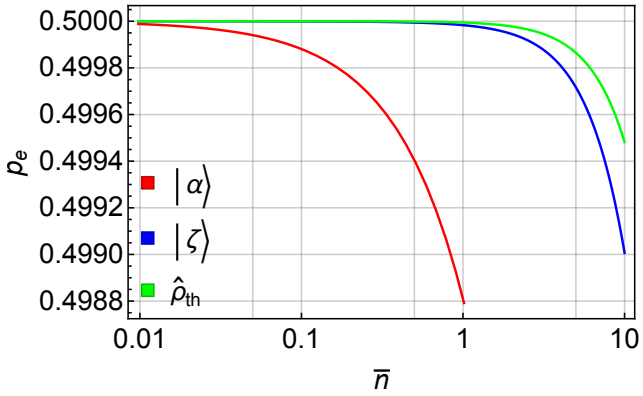

Figure 5.3: Single-shot error probability estimated via the quantum Chernoff bound (upper bound to the Helstrom bound) expression in eq. (3.52) for the three types of single-mode Gaussian state signals. Each curve represents the error probability between states $\hat{\rho}_1$ and $\hat{\rho}_0$. Parameters: $\kappa = 0.1$ and $\bar{n}_{th} = 10$. The quantum Chernoff information is minimized at $s = 1/2$ for all three examples.

The mixing of two thermal states with different mean photon numbers will only produce a thermal state with a larger uncertainty spread on phase space.

Squeezed State Illumination

Illumination with the squeezed vacuum produces the following moments after target interaction

$$\mu_1 = 0,$$
$$\Sigma_1 = \begin{pmatrix} \kappa\left(\bar{n} - \sqrt{\bar{n}(1+\bar{n})}\right) + \bar{n}_{th} + \frac{1}{2} & 0 \\ 0 & \kappa\left(\bar{n} + \sqrt{\bar{n}(1+\bar{n})}\right) + \bar{n}_{th} + \frac{1}{2} \end{pmatrix}, \quad (5.14)$$

where $\bar{n} = \sinh^2 r$. The reflected signal becomes a squeezed thermal state, where the reduction in variance is retained along the q-axis.

The return signal distinguishability for single-mode Gaussian signals are shown in Figure. 5.3, in terms of the quantum Chernoff bound. The coherent state produces the most distinguishable return signal, followed by squeezed vacuum, then thermal state. Only single-shot results are presented here, as the multi-shot expression is simply the quantum Chernoff information to a power: the probability of error can only decrease with successive trials, hence in the

asymptotic limit on the number of trials the coherent state will remain as the best possible choice for single-mode illumination, followed by squeezed vacuum and then the thermal state. For single-mode Gaussian signals, QI is not as advantageous to using CI because the squeezed vacuum does not produce a more distinguishable signal compared to that produced by a coherent state.

5.1.2 Two-Mode Signals

For two-mode Gaussian states, the conditional states now has an ancillary idler mode, which does not interact with the target. The moments of the hypothesis states are as follows:

$$\mu_0 = \mu_i \oplus 0, \qquad \Sigma_0 = \Sigma_i \oplus \Sigma_{th}, \tag{5.15}$$

$$\mu_1 = \mathrm{tr}_e((\mathbb{1}_2 \oplus \mathrm{S}_\kappa)\{\mu_{i,s} \oplus 0\}), \qquad \Sigma_1 = \mathrm{tr}_e((\mathbb{1}_2 \oplus \mathrm{S}_\kappa)(\Sigma_{i,s} \oplus \Sigma'_{th})(\mathbb{1}_2 \oplus \mathrm{S}_\kappa)^T). \tag{5.16}$$

In the case of $\hat{\rho}_0$, the moments are simply the direct sums of the thermal background mode and the idler mode after partial tracing of the signal mode, because it is a product state. If the target is present then only the signal mode and the thermal background mode are mixed by the beamsplitter transform. The matrix $\mathbb{1}_2 \oplus S_\kappa$ is a 6×6 matrix, indicating that overall there are three-modes interacting. Quadrature correlations will remain between the signal and idler modes even after partial tracing of the environment mode.

Two-Mode Coherent State Illumination

A coherent state with mean photon number $2\bar{n}$ sent through a 50:50 beamsplitter will output the same photon statistics as two individual coherent states with $\bar{n}$

$$\mu_{i,s} = \{\sqrt{2\bar{n}}, 0, \sqrt{2\bar{n}}, 0\}, \qquad \Sigma_{i,s} = \mathbb{1}_2/2, \tag{5.17}$$

hence they are separable. The conditional states have the following moments

$$\mu_0 = \{\sqrt{2\bar{n}}, 0, 0, 0\}, \qquad \Sigma_0 = \mathbb{1}_2/2 \oplus \Sigma_{th}, \tag{5.18}$$

$$\mu_1 = \{\sqrt{2\bar{n}}, 0, \sqrt{2\kappa\bar{n}}, 0\}, \qquad \Sigma_1 = \mathbb{1}_2/2 \oplus \Sigma_{th}, \tag{5.19}$$

the former is a product of coherent state and a thermal state, and the latter being the product of a coherent state and a displaced thermal state.

Two-Mode Thermal State Illumination

The two-mode thermal state, is a comparable control test against TMSV because both modes contain thermal statistics, however the two-mode thermal state contains no quadrature correlations. Two identical separable thermal modes of mean photon number $\bar{n}$ have the following covariance matrix

$$\Sigma_{i,s} = \begin{pmatrix} (\bar{n} + \frac{1}{2})\mathbb{1}_2 & 0 \\ 0 & (\bar{n} + \frac{1}{2})\mathbb{1}_2 \end{pmatrix}. \tag{5.20}$$

The covariance of the conditional states are

$$\Sigma_0 = \begin{pmatrix} (\bar{n} + \frac{1}{2})\mathbb{1}_2 & 0 \\ 0 & (\bar{n}_{th} + \frac{1}{2})\mathbb{1}_2 \end{pmatrix}, \tag{5.21}$$

$$\Sigma_1 = \begin{pmatrix} (\bar{n} + \frac{1}{2})\mathbb{1}_2 & 0 \\ 0 & (\kappa\bar{n} + \bar{n}_{th} + \frac{1}{2})\mathbb{1}_2 \end{pmatrix}, \tag{5.22}$$

which are two-mode thermal states with both modes at different mean photon numbers.

Two-Mode Squeezed Vacuum Illumination

The entangled TMSV is the generalised outcome of non-degenerate spontaneous parametric down-conversion, where the signal and idler modes are physically distinguishable from each other. The covariance matrix is stated in eqn. (2.126),

which then produces the following conditional states

$$\mu_0 = 0, \qquad \Sigma_0 = \begin{pmatrix} (\bar{n} + \frac{1}{2})\mathbb{1}_2 & 0 \\ 0 & (\bar{n}_{th} + \frac{1}{2})\mathbb{1}_2 \end{pmatrix}, \tag{5.23}$$

$$\mu_1 = 0, \qquad \Sigma_1 = \begin{pmatrix} \bar{n} + 1/2 & 0 & \sqrt{\kappa\bar{n}(1+\bar{n})} & 0 \\ 0 & \bar{n} + 1/2 & 0 & -\sqrt{\kappa\bar{n}(1+\bar{n})} \\ \sqrt{\kappa\bar{n}(1+\bar{n})} & 0 & \kappa\bar{n} + \bar{n}_{th} + 1/2 & 0 \\ 0 & -\sqrt{\kappa\bar{n}(1+\bar{n})} & 0 & \kappa\bar{n} + \bar{n}_{th} + 1/2 \end{pmatrix}, \tag{5.24}$$

still retaining the nonclassical quadrature correlations between the signal and idler modes dependent on how reflective the target is.

The quantum Chernoff bounds for two-mode illumination are shown in Figure. 5.4. The error probability bounds calculated for TMSV show that it is the most distinguishable Gaussian state signal, in situations of high loss and low reflectivity, performing better than the coherent state. Therefore, QI with TMSV is the most advantageous option for two-mode illumination, and will always outperform any single-mode illumination scheme. Appending extra uncorrelated modes provides no improvements to signal distinguishability compared to using a single-mode signal, as shown by Figure. 5.5.

The multi-shot scenarios comparing CI and QI are presented in Figures 5.6 and 5.7, with their respective error exponents quoted. Upper and lower Chernoff bounds are presented for fixed energy signals in two different conditions. In Figure 5.6, p_e is reduced to 10^{-7} after $\sim 7 \times 10^3$ shots using a coherent state, where using TMSV this error is reached for $\sim 4 \times 10^3$ shots; a 43% reduction compared with CI. In a lossier scenario, where $\kappa = 0.01, \bar{n}_B = 20$, shown by Figure 5.7, more shots overall are required to reach the same error probability: $\sim 1 \times 10^7$ for CI and 3×10^6 for QI, which is a 70% reduction. The upper bound of TMSV eventually falls below the lower bound for the coherent state which suggests for certain that the Helstrom bound for QI is below that for CI.

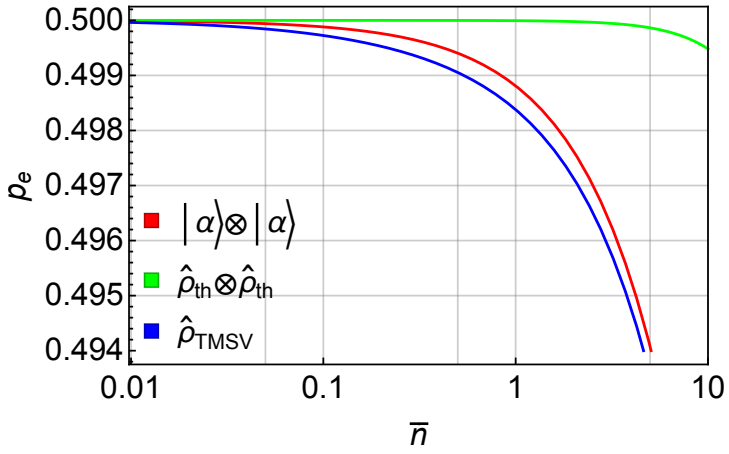

Figure 5.4: Single-shot error probability bound of two-mode signals, estimated via the quantum Chernoff bound, against mean photon number of the signal mode. Parameters: $\kappa = 0.1$ and $\bar{n}_{th} = 10$. The two-mode coherent state error bound is shown for comparison, which happens to coincide with the single-mode error bound (see below). The TMSV produces the lowest error probability compared to all other states.

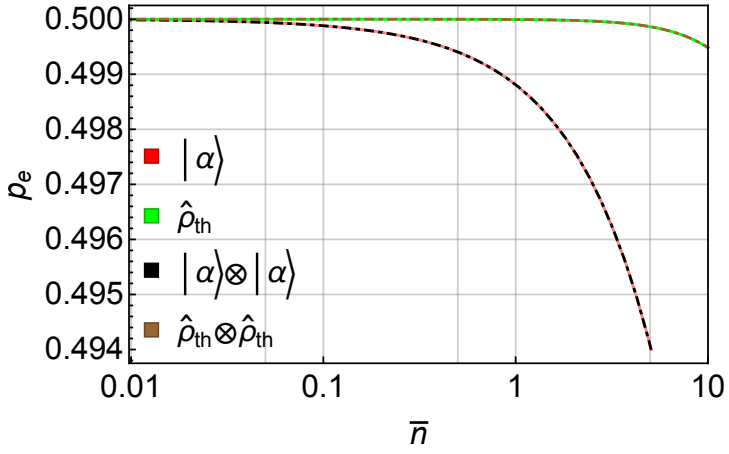

Figure 5.5: Single-shot error probability comparing two-mode separable coherent and thermal states against using single mode signals. Separable state generate no extra distinguishiability as the two-mode outcomes overlaps that of the single-mode outcomes. Parameters: $\kappa = 0.1$ and $\bar{n}_{th} = 10$.

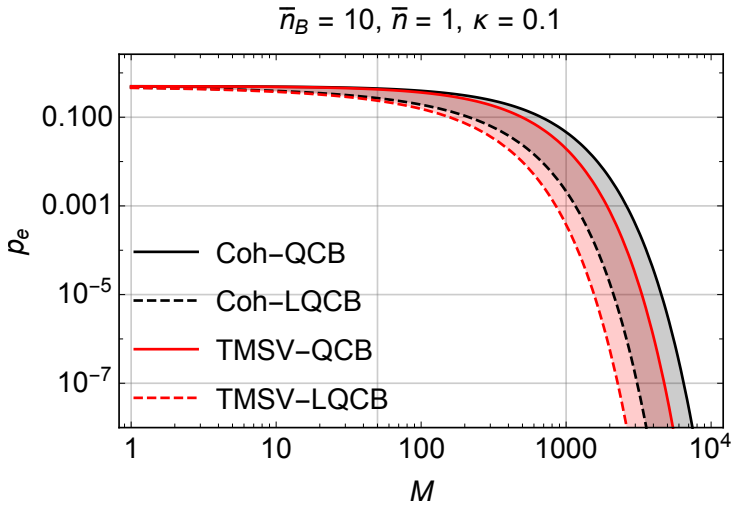

Figure 5.6: Upper (QCB) and lower (LQCB) quantum Chernoff bounds comparing CI and QI for multiple shots. The error exponents of the upper bounds are $\xi_{Coh} = 2.382 \times 10^{-3}$ and $\xi_{TMSV} = 3.247 \times 10^{-3}$ which indicates an improvement of 1.345dB in the asymptotic limit using QI. Note that p_e is plotted in a logarithmic scale.

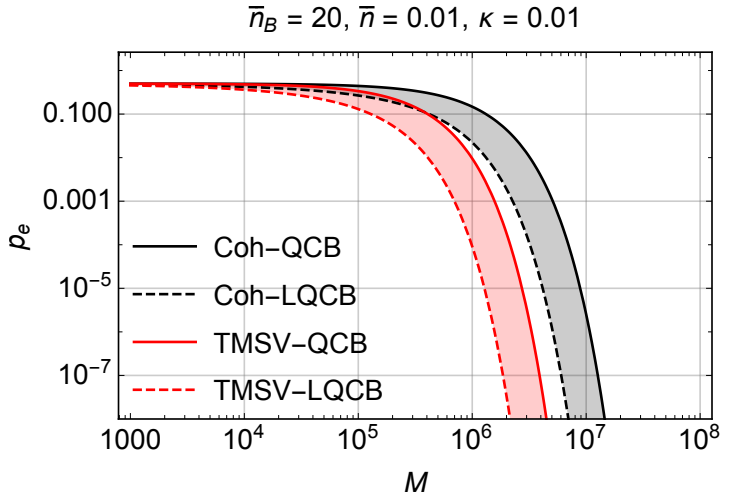

Figure 5.7: Quantum Chernoff bounds in a much lossier scenario using the parameters $\bar{n}_B = 20, \kappa = 0.01$ and $\bar{n} = 0.01$ similar to those in ref. [128]. The error exponents of the upper bounds are $\xi_{Coh} = 1.220 \times 10^{-6}$ and $\xi_{TMSV} = 3.957 \times 10^{-6}$ which indicates an improvement of 5.11dB in the asymptotic limit from using QI. Note that p_e is plotted in a logarithmic scale.

5.2 Quantum Illumination & Detection

5.2.1 Conditional Probabilities of On-Off Detection

The results in the previous section show that for illumination purposes a single-mode coherent state produces the most distinguishable return signal for a given mean photon number, whereas the TMSV does so for two-mode illumination. By including an explicit detection step in the quantum illumination model, the process becomes much more detection-limited and the advantages shown in the previous section are diminished due to losses and the type of detection in consideration. Instead of assuming "optimal detection", this section focusses on incorporating on-off photodetection into the quantum illumination model, where the receiving detector only measures a single-mode state. Quantum illumination will still maintain a distinguishing advantage at low signal energy, however we shall see later for higher signal energy, coherent-state illumination will produce a more distinguishable return signal.

The on-off detector cannot discriminate perfectly between the conditional states $\hat{\rho}_1$ (signal + thermal state) and $\hat{\rho}_0$ (thermal state), because it fires given the existence of any EM field that happens to fall within its detection bandwidth, therefore, both detection outcomes are possible for both conditional states. So there are four conditional probabilities in total to consider for a single on-off detector

$$p(k=1|H_0) \rightarrow \text{false positive}; \quad p(k=1|H_1) \rightarrow \text{true positive};$$
$$p(k=0|H_1) \rightarrow \text{false negative}; \quad p(k=0|H_0) \rightarrow \text{true negative}.$$

The error probabilities are sometimes referred to as "false alarm" for false positive and "miss" for false negative. Click outcomes from returning signals will eventually estimate target presence because there is signal in $\hat{\rho}_1$, compared to $\hat{\rho}_0$, which induces a higher click probability compared to the false alarm probability. For a single shot

$$\frac{p(1|H_1)}{p(1|H_0)} \geq 1. \tag{5.25}$$

For a multiplexed on-off detector, we have

$$p_N(k>0|H_0) \rightarrow \text{false positive}; \quad p_N(k>0|H_1) \rightarrow \text{true positive};$$
$$p_N(k=0|H_1) \rightarrow \text{false negative}; \quad p_N(k=0|H_0) \rightarrow \text{true negative},$$

where the detection outcomes are partitioned into the no-click outcome ($k=0$) separate from the multi-click outcomes ($k>0$).

By using the conditional probabilities, we can then calculate the posterior probability after obtaining a certain number of clicks. For example, target presence after k-clicks would be

$$p(H_1|k) = \frac{p(H_1)p(k|H_1)}{p(H_1)p(k|H_1)+p(H_0)p(k|H_0)}. \tag{5.26}$$

The estimation of prior probabilities $p(H_1)$ and $p(H_0)$ are non-trivial, however obtaining one value would imply the other as $p(H_1)+p(H_0)=1$.

Therefore, clicks (or multiple clicks) will lead us to estimate that the target is present because the no-click probability primarily is dependent on the vacuum population of the hypothesis state's density matrix, which is lower in $\hat{\rho}_0$ compared to that in $\hat{\rho}_1$. We can then increase our confidence in our estimation of target presence/absence by repeating measurements.

5.2.2 Receiving Detector Probabilities

Let the receiving detector be an on-off detector multiplex containing N_s detectors, with quantum efficiency η_s per detector. A state which hits this detector may trigger none, one or multiple clicks, k_s.

False Alarm Clicks

If the probe signal has been lost, or the target is absent, then the detector will measure only the background state $\hat{\rho}_0$. The detector will click with probability

$$p_{N_s}(k_s|H_0) = \binom{N_s}{k_s} \sum_{l_s=0}^{k_s} \frac{\binom{k_s}{l_s}(-1)^{k_s-l_s}}{1+\eta_s \bar{n}_{th}(1-l_s/N_s)}, \tag{5.27}$$

which is the expectation value of $\hat{\Pi}_{N_s,k_s}$ with respect to $\hat{\rho}_0$ that can also be calculated by substitution of the thermal state moments into the multi-click probability

for Gaussian states in eq. (4.32). This is the false alarm click distribution of the receiving detector, valid for all single-mode analysis. In the instance of a single on-off detector, the expression (5.27) becomes

$$p_1(1|H_0) = 1 - \frac{1}{1+\eta_s\bar{n}_{th}}, \tag{5.28}$$

coinciding with eq. (4.12). Substitution of $k_s = 0$ into eq. (5.27) gives the "true negative" probability as

$$p(0|H_0) = \frac{1}{1+\eta_s\bar{n}_{th}}, \tag{5.29}$$

which is independent of the number of detectors. All null hypothesis conditional probabilities are independent of mean photon number from the signal and reflectivity parameters. Ideally $p(0|H_0)$ should be maximised by setting $\bar{n}_{th} = 0$ which in turn minimizes the false alarm probability.

Coherent State Illumination

For the coherent state signal, the reflected state $\hat{\rho}_1$ is a displaced thermal state. The multi-click probability is obtained by substitution of the displaced thermal state moments into eq. (4.32), which gives

$$p_{N_s}(k_s|H_1) = \binom{N_s}{k_s} \sum_{l_s=0}^{k_s} \frac{\binom{k_s}{l_s}(-1)^{k_s-l_s}}{1+\eta_s\bar{n}_{th}(1-l_s/N_s)} e^{-\frac{\kappa\bar{n}\eta_s(1-l_s/N_s)}{1+\eta_s\bar{n}_{th}(1-l_s/N_s)}}. \tag{5.30}$$

This expression maintains an exponential function of $\bar{n}$, characteristic of displacement in the state. The single on-off detector click outcome is

$$p_1(1|H_1) = 1 - \frac{1}{1+\eta_s\bar{n}_{th}} e^{-\frac{\kappa\bar{n}\eta_s}{1+\eta_s\bar{n}_{th}}}, \tag{5.31}$$

and coincides with expression (4.12) when $\bar{n}_{th} = 0, \kappa = 1$. In terms of errors, the miss probability is

$$p(0|H_1) = \frac{1}{1+\eta_s\bar{n}_{th}} e^{-\frac{\kappa\bar{n}\eta_s}{1+\eta_s\bar{n}_{th}}}. \tag{5.32}$$

Quantum Illumination with Multi-Click Heralded TMSV

Optimal detection of two-modes demands that the detection occurs simultaneously, which is impractical because the idler mode needs to be stored coherently

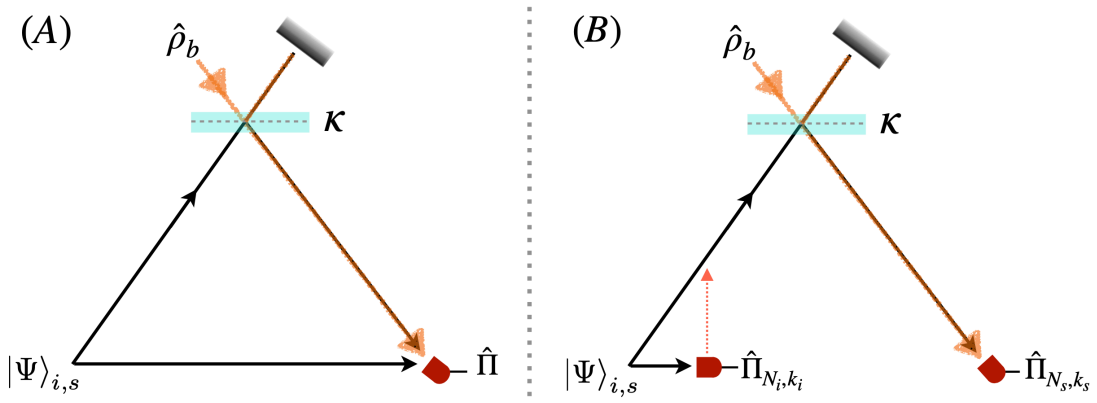

Figure 5.8: Two-mode QI illumination methods with target presence. The state $|\Psi\rangle_{i,s}$ is a TMSV. (A) Simultaneous measurement: both modes are measured together after signal mode is reflected. (B) Non-simultaneous measurement, with on-off detector multiplexes: the idler mode is measured first via $\hat{\Pi}_{N_i,k_i}$, which conditions the remaining signal mode to be reflected off the target, then measured by $\hat{\Pi}_{N_s,k_s}$. Correlations in measurement outcomes between the heralding and receiving detector remain, even under losses, thanks to entanglement.

in order to try and perform a time-correlated measurement with the returning signal. Instead, a much simpler scheme which can boost signal strength is to perform a heralding detection on the idler mode first, which sends out a signal with higher mean photon number that eventually leads to a more distinguishable return signal. This is a direct implementation of the state engineering technique stated in Section 4.3 shown in Figure 5.8, and is more of a "staggered" detection approach which show the change in statistics due to different detection times.

The multi-click heralded TMSV is therefore the single-mode probe state and the explicit expression for $\hat{\rho}_1$ is derived as follows: let N_i, k_i and η_i be the parameters of the heralding on-off detector multiplex, such that $\hat{\rho}_{N_i,k_i}$ is the sent multi-click heralded state. As $\hat{\rho}_{N_i,k_i}$ is a weighted summation of thermal states, it is easier to transform a single constituent thermal state $\hat{\varrho}[\bar{m}_{N_i,l_i}]$ using eq. 5.5 and then use linearity to construct the overall state $\hat{\rho}_1$.

The transformation in eq. (5.5) on a single thermal state is $\hat{\varrho}[\bar{m}_{N_i,l_i}]$, is

$$\mathrm{tr}_e\left(\hat{U}_\kappa \hat{\varrho}[\bar{m}_{N_i,l_i}] \otimes \hat{\varrho}[\bar{n}_{th}/(1-\kappa)]\hat{U}_\kappa^\dagger\right) = \hat{\varrho}[\kappa\bar{m}_{N_i,l_i} + \bar{n}_{th}], \tag{5.33}$$

which is just another thermal mode with mean photon number $\kappa\bar{m}_{N_i,l_i} + \bar{n}_{th}$. Then, as summations are linear, the binomial sum and normalisation constants of $\hat{\rho}_{N_i,k_i}$ (c.f. eqn. (4.44)) gives

$$\hat{\rho}_1 = \mathcal{N}_{N_i,k_i} \sum_{l_i=0}^{k_i} \binom{k_i}{l_i} (-1)^{k_i-l_i} (1+\bar{m}_{N_i,l_i}) \hat{\varrho} \left[\kappa\bar{m}_{N_i,l_i} + \bar{n}_{th}\right], \tag{5.34}$$

which is the density matrix of the signal mode reflected by the target. At the receiving detector, the click probabilities are derived by taking the expectation value of the $\hat{\Pi}_{N_s,k_s}$ with respect to $\hat{\rho}_1$

$$p_{N_s}(k_s|H_1) = \mathcal{N}_{N_i,k_i} \binom{N_s}{k_s} \sum_{l_i=0}^{k_i} \sum_{l_s=0}^{k_s} \frac{\binom{k_i}{l_i}\binom{k_s}{l_s}(-1)^{k_i+k_s-l_i-l_s} \left(\frac{1+\bar{m}_{N_i,l_i}}{1+\kappa\bar{m}_{N_i,l_i}+\bar{n}_{th}}\right)}{1-\left(\frac{\kappa\bar{m}_{N_i,l_i}+\bar{n}_{th}}{1+\kappa\bar{m}_{N_i,l_i}+\bar{n}_{th}}\right)(1-\eta_s(1-l_s/N_s))}, \tag{5.35}$$

which is essentially a coincidence probability of the heralding and receiving detector clicks after the signal mode has undergone losses by interacting with a thermal state. This is the general equation for the "true positive" probability from using click detector multiplexes for QI. Substation of $N_s = 1, k_s = 1$ into eq. (5.35) shows that a single receiving detector will click with probability

$$p_1(1|H_1) = 1 - \mathcal{N}_{N_i,k_i} \sum_{l_i=0}^{k_i} \frac{(-1)^{k_i-l_i}\left(\frac{1+\bar{m}_{N_i,l_i}}{1+\kappa\bar{m}_{N_i,l_i}+\bar{n}_{th}}\right)}{1-\left(\frac{\kappa\bar{m}_{N_i,l_i}+\bar{n}_{th}}{1+\kappa\bar{m}_{N_i,l_i}+\bar{n}_{th}}\right)(1-\eta_s)}, \tag{5.36}$$

where by using $p_1(1|H_1) = 1 - p(0|H_0)$, the latter terms show the no-click probability as a function of mean photon number and heralding clicks, which can be reduced by multiple heralding clicks.

5.2.3 Results

Click Probability Curves

The single receiving detector click probability $p_1(1|H_1)$ for both CI and QI are shown in Figure 5.9, as well as the posterior probability. The advantage of QI compared to CI, the likelihood of triggering a detector click given target presence, is apparent for low $\bar{n}$ due to the relative gain in energy to the signal mode via heralding. However, this eventually diminishes for higher $\bar{n}$ values, as for a highly

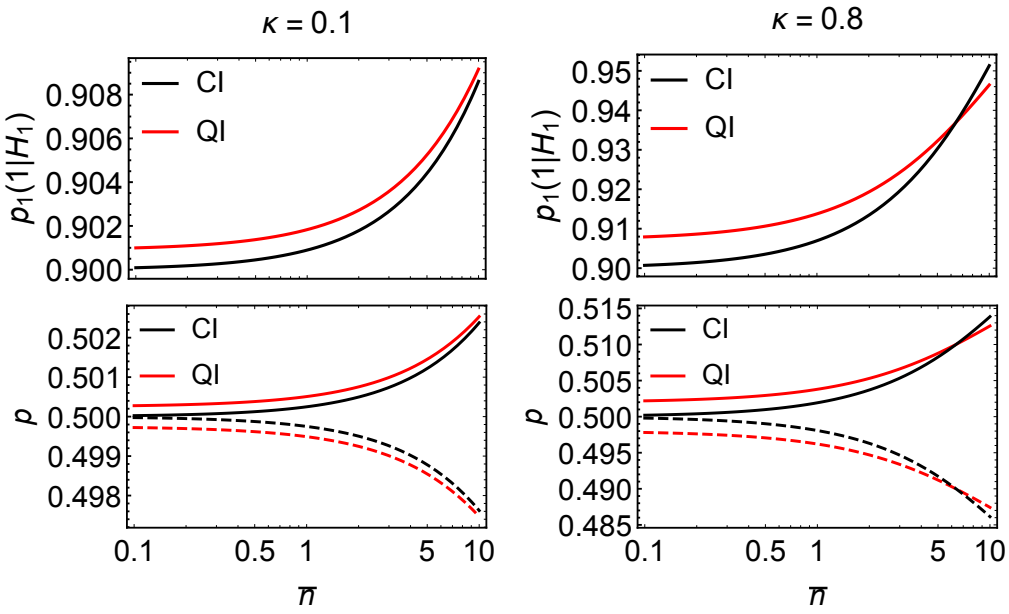

Figure 5.9: Top Row: single receiving detector click probability, under target presence scenario, with reflectivities of $\kappa = 0.1$ and $\kappa = 0.8$ against mean photon number of the (unconditioned) signal mode. Bottom Row: corresponding posterior probabilities. Solid cuves show $p_1(H_1|1)$. Dashed curves represent $p_1(H_0|1)$, which correctly decreases from $p = 1/2$ under object presence. CI and QI are compared. Parameters: $\bar{n}_{th} = 10$, $\eta_s = 0.9$. The quantum probe signal is a single detector heralded TMSV $\hat{\rho}_{1,1}$, which triggers a higher detection probability at low mean photon numbers $\bar{n} < 5$.

reflective target, CI surpasses in this probability for mean photon number values greater than 5.

The loss of advantage for QI past the crossover point, where CI is more likely to produce a distinguishable return signal, is due to the differences in the photon number distribution of a coherent state vs. click heralded TMSV at high mean photon numbers. The higher harmonic oscillator levels are more likely to trigger a click outcome – the coherent state which has a Poissonian photon number distribution occupies such higher harmonic oscillator levels for greater $\bar{n}$ values – whereas the single click heralded TMSV does not because its distribution appears thermal (see Figure 5.10). These differences in the photon number distribution are picked up by the click outcome POVM, because it relies on parts of the

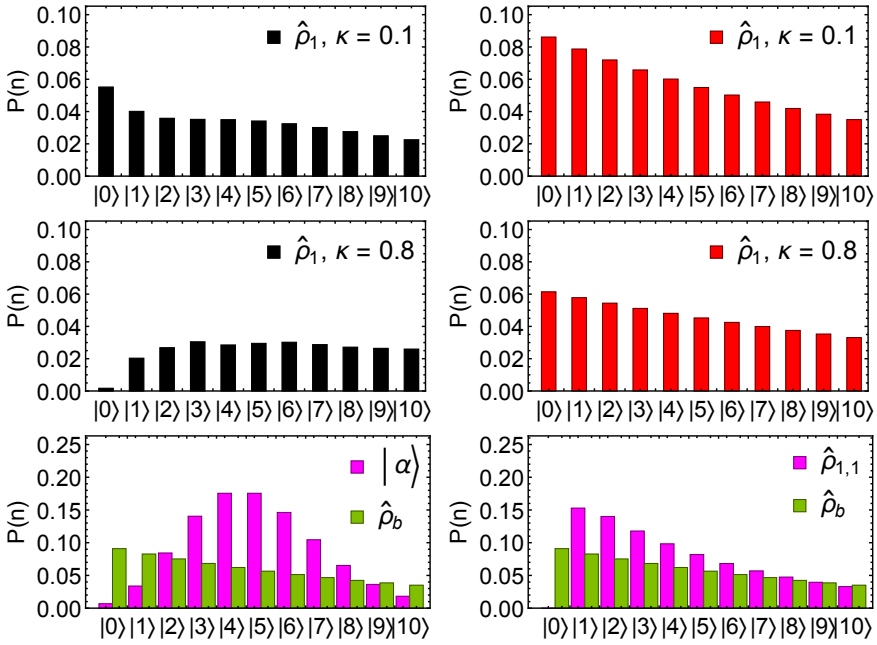

Figure 5.10: Photon number distributions of states involved in CI and QI up to ten photons. Top two rows show $P(n)$ for the reflected state $\hat{\rho}_1$, with reflectivities $\kappa = 0.1$ and $\kappa = 0.8$. The signal and thermal background mean photon numbers are $\bar{n} = 5$ and $\bar{n}_{th} = 10$. Bottom row shows $P(n)$ for both signal and background before object interaction. The reflected state $\hat{\rho}_1$ is a mixed state which interpolates between $P(n)$ of the signal and background modes depending on the amount of mixing facilitated by the beamsplitter-modelled target. $P(n)$ of the displaced thermal state was obtained from the analytical results in ref. [129].

photon number distribution not in the vacuum state. The returning state $\hat{\rho}_1$ has a mixture distribution due to the interaction of signal and thermal modes, in which the coherent state contributes to large occupation at higher harmonic oscillator levels, compared to $\hat{\rho}_{1,1}$. Also, the heralding boost to signal mean photon number becomes less significant for large $\bar{n}$ (see Figure 4.9), hence the state $\hat{\rho}_1$ would not contain as large a portion of non-vacuum compared to that produced from a high energy coherent state.

Extension to using multi-click heralded states for QI produces a similar advantage to single click heralded states at low signal energy. Due to the greater relative gain to $\bar{n}$ in the signal mode cause by simultaneous multi-click measure-

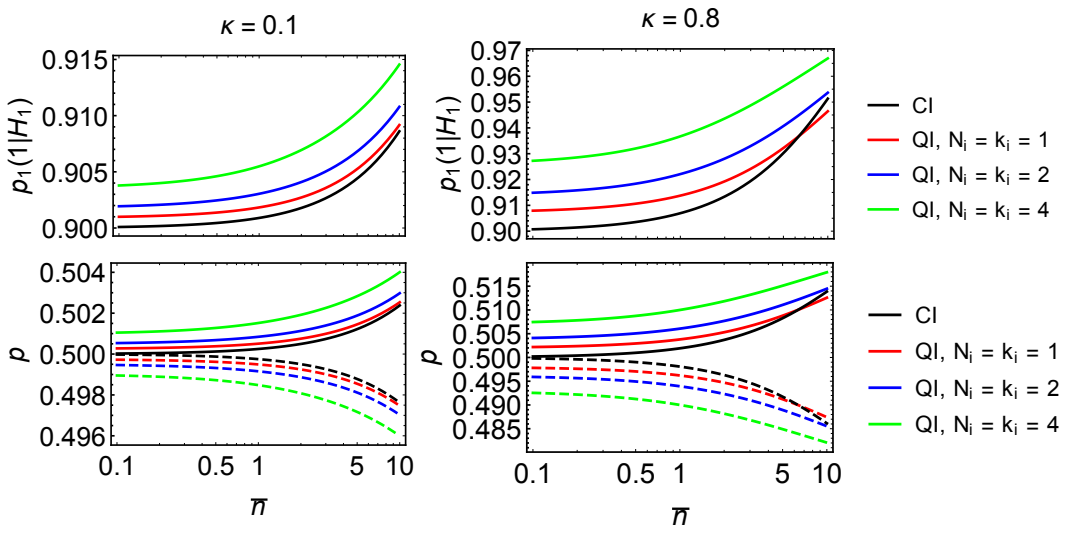

Figure 5.11: Top Row: single receiving detector click probability for multi-click heralded TMSV signals, against mean photon number of the (unconditioned) signal mode. These examples include states heralded by all detectors clicking in the idler multiplex $N_i = k_i$. Parameters: $\bar{n}_{th} = 10$, $\eta_s = 0.9$. Bottom Row: corresponding posterior probabilities. Coherent state signals require higher $\bar{n}$ values to beat performance of multi-click heralded TMSV states.

ment on the idler mode, the return state $\hat{\rho}_1$ is even more likely to trigger a single click of the receiving detector, and covers greater $\bar{n}$ values where it performs better than the coherent state.

Figure 5.11 shows the single detector click probability along with respective posterior probability of target presence given an occurrence of a single click, as a function of $\bar{n}$. These probabilities are calculated via Bayes' Law with no prior knowledge of the presence of the target so that $pr(H_1) = p(H_0) = 1/2$ – a click at the detector therefore increases our estimate that the target is present, and decreases if it is absent due to the lower click probability from the background noise. Again, for low mean photon number there is a persisting enhancement to estimation using QI, alongside advantages for CI at high $\bar{n}$ in the form of crossover points.

Under this non-optimal measurement scheme, multi-click heralded TMSV illumination is not always better than coherent state illumination under condi-

tions where target reflectivity is high and signal energy is high. But in very lossy conditions with low signal energy, high background noise and low target reflectivity, QI will provide a slight advantage in triggering a receiver click. Each detection result then provides more information with regards to target presence or absence if quantum states were used instead of coherent states thanks to the photon number correlations of the TMSV.

ROC Curves

The receiver-operating characteristic (ROC) curve is a common method used to visualise the performance of a binary classifier [85, 104]. Usually it is a phase space plot of the true positive probability against the false positive probability for a single classifier. The ideal binary ROC would have a curve tracing the right angle of the top left corner in this instance (all detection outcomes are characterised as true positives). A random classifier is simply a diagonal bisector from the bottom left corner to the top right corner.

The ROC curves for the single receiving detector are shown by Figures 5.13 and 5.12. The curves produced by plotting eqs. (5.28) against eqs. (5.31) and (5.36), showing how the detector responds to different signal states used in the illumination process. Some assumptions have been made in order to increase the distinguishability of the ROC curves, compared to parameters a very lossy scenario as the curves will appear very compacted (see Figure 5.13).

I have substituted reflectivity $\kappa = 0.8$ which leads to a higher portion of the signal being returned, this is to increase the distinguishability of the ROC curves. An increase to signal energy generally causes the curves to collectively shift towards the top left corner, however to obtain all the points on the ROC curve, the plots are parameterised in terms of the quantum efficiency of the receiving detector, which will truncate the ROC (see Figure 5.12 if the value is low. The background noise will also truncate the ROC because the click probability is a function of the background noise. In the limit of $\bar{n}_{th} \to \infty$, all points of the ROC will converge on the top right corner however this also causes the curves to pull towards the random classifier line.

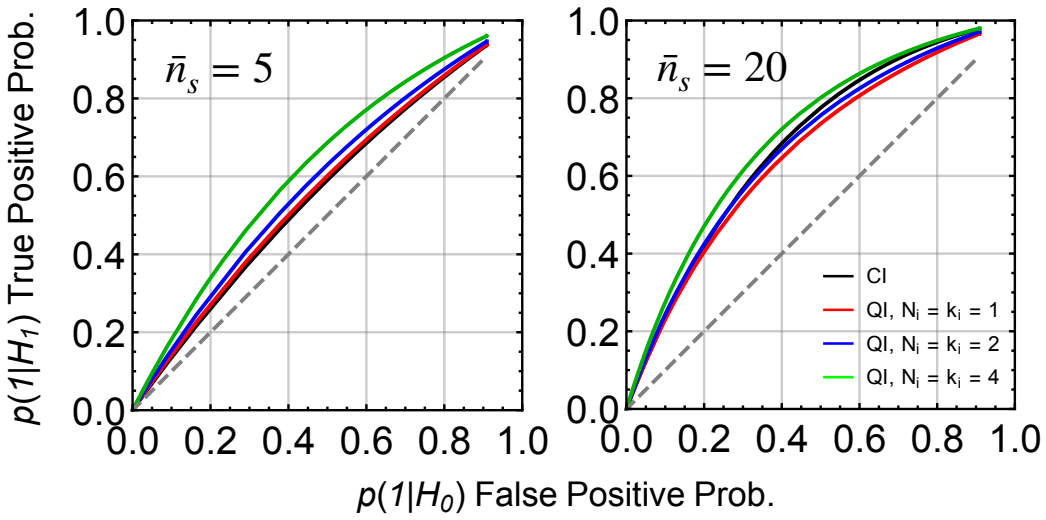

Figure 5.12: ROC curves of the single click detector used in classical illumination (CI) vs. quantum illumination (QI). Parameters: $\bar{n}_{th} = 10, \kappa = 0.8, \eta_i = 0.9$.

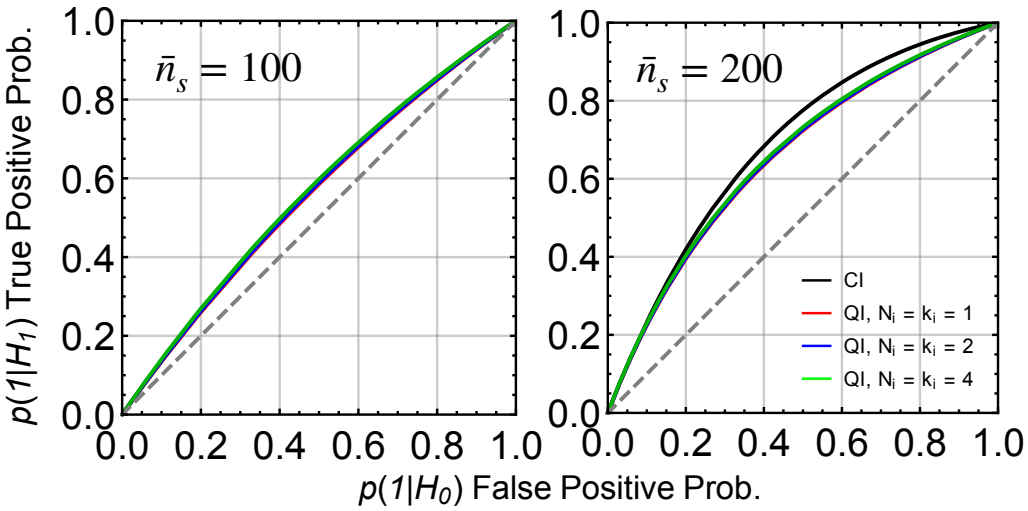

Figure 5.13: ROC curves of the single click detector used in classical illumination (CI) vs. quantum illumination (QI) in a high signal, high noise scenario. Parameters: $\bar{n}_{th} = 100, \kappa = 0.8, \eta_i = 0.9$. Curves are no longer truncated however the noise diminishes the difference in performance from different illumination strategies.

For the plots on the left of the figures, the ROC suggests that QI again would perform better for when the signal energy is low compared to the background noise as it maintains a higher probability of true positive compared to the coherent

state. Similarly, higher number of simultaneous heralding clicks will increase this probability due to the boost heralding provides to the mean photon number of the signal. But as signal energy becomes greater than the background noise, the crossover behaviour of the coherent state illumination, where it outperforms quantum illumination, start to appear on the ROCs, again suggesting that CI is more suited for illumination where the signal is greater than the background noise.

5.3 Simulation of Sequential Detection

The analytical results in the previous section allow calculation of conditional probability of single-shot outcomes. The posterior probability plots in Figures 5.9 and 5.11 show that after each detection outcome there results in a small increase/decrease to estimating target presence. To increase the robustness of this estimation, we must consider multiple, sequential detection events as if our detector was firing every so often.

5.3.1 Main Method

A multi-shot detection process is a sequence of M measurement trials, or "shots". After each detection, the estimated probabilities of target presence and absence are updated using Bayes' Law. For example, starting with the zeroth trial, denoted by superscript (0) , we simply have the prior probabilities:

$$p^{(0)}(H_1) = P, \tag{5.37a}$$

$$p^{(0)}(H_0) = 1 - P, \tag{5.37b}$$

where P is some pre-estimated probability of target presence. After the first measurement outcome (of k-clicks), the target present/absent probabilities are

then updated like so

$$p^{(1)}(H_1|k) = \frac{p^{(0)}(H_1)\,\mathrm{tr}\Big(\hat{\rho}_1\hat{\Pi}_{N,k}\Big)}{p_N^{(0)}(k)}, \tag{5.38a}$$

$$p^{(1)}(H_0|k) = \frac{p^{(0)}(H_0)\,\mathrm{tr}\Big(\hat{\rho}_0\hat{\Pi}_{N,k}\Big)}{p_N^{(0)}(k)}. \tag{5.38b}$$

The above equations are simply the posterior probabilities that are based on the probability of the detection outcome of k-clicks (on a multiplex of N-detectors). The normalisation is

$$p_N^{(0)}(k) = p^{(0)}(H_0)\,\mathrm{tr}\Big(\hat{\rho}_0\hat{\Pi}_{N,k}\Big) + p^{(0)}(H_1)\,\mathrm{tr}\Big(\hat{\rho}_1\hat{\Pi}_{N,k}\Big), \tag{5.39}$$

which is the click probability that is a weighted sum of the conditional click probabilities. The measurement operator $\hat{\Pi}_{N,k}$ is indicative of how many clicks occurred in this trial (including no-click, $k = 0$). Then, in the next measurement trial $M = 2$, we will use the previous posterior probability as new target present/absent probabilities

$$p^{(2)}(H_1|k) = \frac{p^{(1)}(H_1)\,\mathrm{tr}\Big(\hat{\rho}_1\hat{\Pi}_{N,k}\Big)}{p_N^{(1)}(k)}, \tag{5.40a}$$

$$p^{(2)}(H_0|k) = \frac{p^{(1)}(H_0)\,\mathrm{tr}\Big(\hat{\rho}_0\hat{\Pi}_{N,k}\Big)}{p_N^{(1)}(k)}. \tag{5.40b}$$

The "new" prior probabilities are assigned the posterior probabilities

$$p^{(1)}(H_1) := p^{(1)}(H_1|k), \tag{5.41a}$$

$$p^{(1)}(H_0) := p^{(1)}(H_0|k), \tag{5.41b}$$

feeding also into the normalisation $p_N^{(1)}(k)$.

Thus in general, the outcomes are estimated recursively via

$$p^{(M+1)}(H_i|k) = f[p^{(M)}(H_i) := p^{(M)}(H_i|k)], \tag{5.42}$$

where f is the posterior probability equation, which uses the posterior probability from the previous measurement trial as the "new" prior probability.

After each shot, both target present/absent probabilities deviate a little from their previous value as new information is continuously attained through detection. By tracking this change in, e.g. in $p(H_1)$ per shot, the trajectory will

represent the performance of a signal with a *particular* photon statistic in the illumination and detection process – the performance of different signal states at the same energy can then be compared to see which converges or reaches the largest value $p(H_1)$ in the least amount of shots.

5.3.2 Simulating Detector Clicks

From the previous chapter, we saw that a multiplex detector can produce k-clicks based on the photon statistics of the signal hitting it. The detector statics, then, must also be considered and incorporated stochastically into the simulation of a sequential detection process.

To model this inherent randomness in detection, during *each shot* the following steps are performed before the calculating the posterior probability

1. Calculate the click probability distribution of the receiving detector, with respect to a state it is measuring ($\hat{\rho}_1$ or $\hat{\rho}_0$) that is, the probability of every k-clicks result possible $\{p_N(0), p_N(1) \dots p_N(k = N)\}$.

2. Generate a new random number, that represents a probability, and bin it into a probability value corresponding to the click probability, using the detector cumulative distribution to find out how many clicks occurred this shot, then use the projector $\hat{\Pi}_{N,k}$ to calculate conditional probabilities.

3. If using quantum illumination, do the previous two steps to simulate a heralding detection outcome. The heralding detector probabilities have to be calculated using the partially traced TMSV state, before subsequently evaluating the receiving detector result using state $\hat{\rho}_{N_i,k_i}$. This ensures that the signal state heralded is produced probabilistically.

In Step 2, the number of clicks is determined probabilistically an inverse transform sampling method [130]. By using a (pseudo)random number, $R \in [0, 1)$, this is treated as a probability and binned according to the cumulative click distribution of the detector (see Figure 4.3). The cumulative click distribution

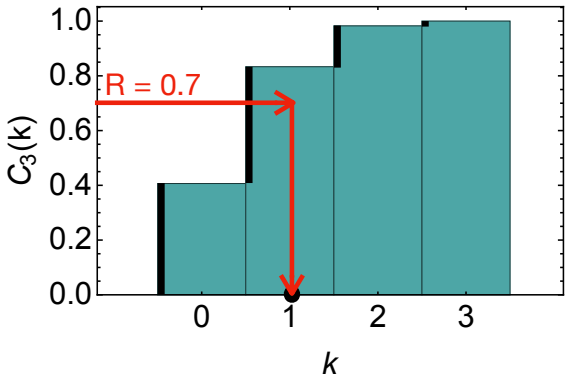

Figure 5.14: The cumulative click distribution $C_N(k)$: clicks are selected via a pseudorandom number R: this example shows cumulative click distribution for an $N = 3$ detector multiplex measuring a coherent state, with $\eta = 0.9$ and $\bar{n} = 1$. Solid black edges represent $p_N(k)$. The random number here is $R = 0.7$, hence $k_M = 1$ is selected because it falls within the interval covered by $p_{N=3}(k = 1)$.

function $C_N(k)$ is used to determine this

$$C_N(k) = \sum_{k'=0}^{k} p_N(k'), \tag{5.43}$$

calculated via summation of click probabilities from 0 to k (keeping N fixed); for $k = N$ this value is 1. The task is to determine which k_M caused the detector to fire with probability R, which can be found by simply checking which interval R falls in-between, demonstrated in Figure 5.14, where $R = 0.7$ is in between the interval $[C_3(0), C_3(1))$ and takes the upper limit value $k_M = 1$. This selection process must be applied for every detector in the model, using independently generated random numbers.

For the modelling of QI, generation of a multi-click heralded TMSV *per shot* must be probabilistic, conditioned by the heralding probability. A separate random number R is therefore required to select from $C_N(k)$ of the heralding click distribution, leading to a potentially different probe state $\hat{\rho}_{N_i,k_i=k_M}$ per shot for target detection. This scenario is more realistic as for low $\bar{n}$, single photon states will be generated with higher probability compared to states generated by multiple clicks. After establishing the number of clicks, the conditional probabilities associated with the number of clicks are calculated from Bayes' Law in the steps

stated in the main method.

Due to H_0 and H_1 being two different physical situations, target presence and absence must have separate trajectories, as $\hat{\rho}_0$ and $\hat{\rho}_1$ produce different click distributions and different detection outcomes. For example, signal detector clicks with target present are denoted as k_{M1}, selected using the cumulative click distribution that includes $\hat{\rho}_1$

$$C_N(k) = \sum_{k'=0}^{k} p_N(H_1|k'), \tag{5.44}$$

so that the probabilities are updated via

$$p^{(M+1)}(H_1) = p^{(M)}\left(H_1|k_s = k_{M1}\right), \tag{5.45a}$$

$$p^{(M+1)}(H_0) = p^{(M)}\left(H_0|k_s = k_{M1}\right). \tag{5.45b}$$

There are two probabilities here because both are required to calculate the denominator in Bayes' Law. For a large number of measurements, assuming that the signal is reflected, it is expected that $p(H_1) \to 1$ and $p(H_0) \to 0$.

Conversely, if target is absent, then the signal detector clicks are denoted as k_{M0}, selected using the cumulative click distribution including $\hat{\rho}_0$

$$C_N(k) = \sum_{k'=0}^{k} p_N(H_0|k'), \tag{5.46}$$

so that the probabilities are updated via

$$p^{(M+1)}(H_1) = p^{(M)}\left(H_1|k_s = k_{M0}\right), \tag{5.47a}$$

$$p^{(M+1)}(H_0) = p^{(M)}\left(H_0|k_s = k_{M0}\right), \tag{5.47b}$$

then for a large number of measurements $p(H_1) \to 0$ and $p(H_0) \to 1$, because the signal has been lost.

5.3.3 Results

Varying Shots and Averaging Trials

Trajectories comparing that of a coherent state and a single-click heralded TMSV are shown in the following figures. In Fig. 5.15, examples of CI and QI trajectories

using single click detectors are shown with varying number of shots (M) and averages (T).

The fluctuations of single trajectories are averaged out for many runs which give a clearer indication of the trend a trajectory will follow. All plots show estimated target presence for a present target. Higher number of shots lead to a clearer indication as the probability values eventually converge to 1, as detection of reflected signal boosts $p(H_1)$ and eventually converges. By using QI, estimating

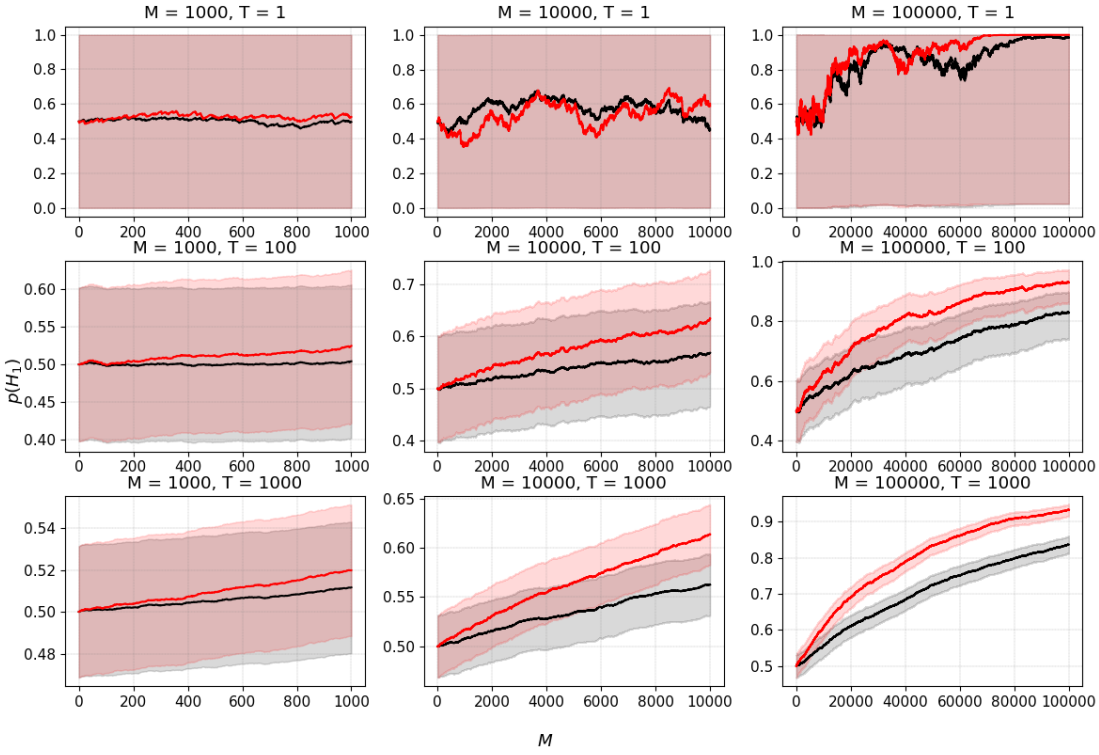

Figure 5.15: Trajectories estimating target presence using the sequential detection model, using a single heralding detector and a single receiving detector. Black and red represent CI and QI respectively alongside their shaded confidence intervals. Parameters: $\bar{n} = 1$, $\bar{n}_{th} = 5$, $\kappa = 0.1$ and $\eta_s = \eta_i = 0.9$. Left to right plots indicate increase in overall number of shots (M) whereas for top to bottom shows increase in number of trajectories averaged over (T). The shaded region represents estimated 95% confidence using the Clopper-Pearson interval. We can see that by increasing the number of shots we obtain convergence towards $p(H_1) = 1$ and that averaging reduced fluctuations and narrows the confidence interval.

target presence requires less number of shots compared to classical illumination, which translates to faster detection. In the simulation with 1000 shots, the cumulative effects of sequential detection is not readily apparent, because the difference in conditional probabilities with respect to detection are small

$$\text{CI}: \quad p_1(1|H_1) = 0.821133 \rightarrow p_1(H_1|1) = 0.5009, \tag{5.48}$$

$$\text{QI (no heralding click)}: \quad p_1(1|H_1) = 0.818338 \rightarrow p_1(H_1|1) = 0.500048, \tag{5.49}$$

$$\text{QI (heralding click)}: \quad p_1(1|H_1) = 0.824188 \rightarrow p_1(H_1|1) = 0.501828. \tag{5.50}$$

Each click that contains the reflected probe signal will increase the estimation of target presence – in this particular example, QI with single click heralded state approximately doubles the increase to $p_1(H_1|1)$ (from 0.5) caused by CI with coherent states; if no heralding clicks occur in the idler mode then QI will generate approximately half such increase compared to CI.

The trajectories in Figure 5.15 factors in all such possible results for a realistic comparison because a successful heralding click does not occur every single shot: single click heralding probability for TMSV with $\bar{n} = 1, \eta_i = 0.9$ is 0.474 hence roughly 47% of the shots include click heralded TMSV states, whereas coherent states are assumed similar for every shot. Click heralding increases the mean photon number of the signal mode from 1 to 2.05, which eventually leads to the higher detection probability of QI compared to CI.

Confidence Intervals

The 95% confidence intervals shown on the figures in this section have been generated for each point in the trajectory using the Clopper-Pearson method [131, 132]. As the probability lies between 0 and 1, the distribution which the mean represents is assumed to be binomial. We cannot use the normal approximation to estimate binomial bounds as this will lead to overshoot if the probability is close to 0 or 1.

The Clopper-Pearson bounds are calculated using the beta distribution [133]

$$B(z; u, v) = \frac{\Gamma(u, v)}{\Gamma(u)\Gamma(v)} z^{u-1}(1-x)^{v-1}, \tag{5.51}$$

with $\Gamma(u)$ being the Gamma function. The upper and lower Clopper-Pearson bounds can be calculated using the quantiles of the Beta distribution [132] like so

$$B\left(\tfrac{\alpha}{2}; x, n-x+1\right) < p < B\left(1-\tfrac{\alpha}{2}; x+1, n-x\right). \tag{5.52}$$

Given that the trajectories are averaged over T runs, the parameters are: $\alpha = 0.05$ or 95% confidence, with $x = \mu T$ and $n = T$, μ indicating the average.

Varying Heralding Detectors

We see that in the previous chapter that varying the number of heralding detectors can lead to a higher gain in signal energy if there are multiple heralding clicks.

For QI which uses multiple heralding detectors to general multi-click heralded TMSV probe signals – the averaged results are shown in Figure. 5.16, which gives an average of 3×10^3 trajectories for 5×10^4 consecutive shots. The heralded

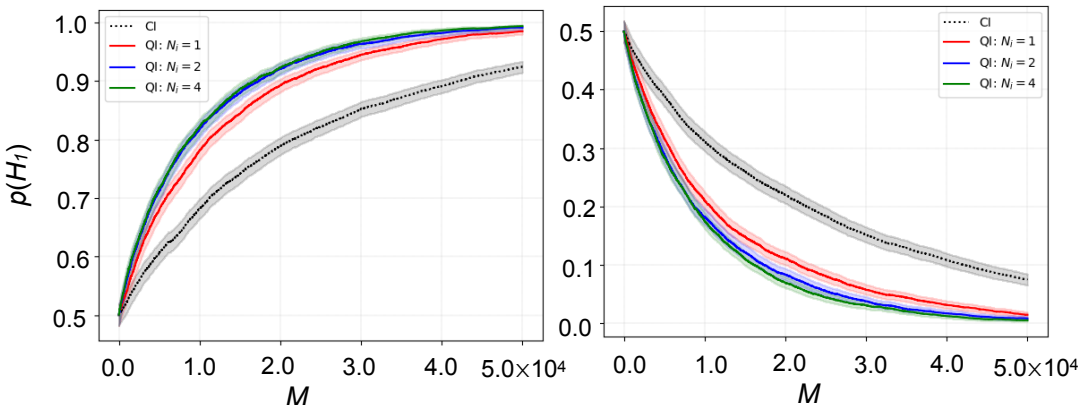

Figure 5.16: Trajectories of estimated target presence $p(H_1)$ from single receiving detector clicks, using CI and QI with multi-click heralded TMSV states, averaged over 3×10^3 trajectories. Each contains $M = 5 \times 10^4$ shots in order to show convergence of trajectories. Parameters: $\bar{n} = 1$, $\kappa = 0.1$ and $\bar{n}_{th} = 3$, heralding and receiving detectors have $\eta_i = \eta_s = 0.9$. Left and right plots demonstrates target presence probability for a present vs. absent target respective – quantum illumination correctly estimates state presence faster compared to coherent state illumination. 95% confidence intervals are shown also to be narrower compared with those in Figure 5.15.

quantum signals significantly outperform the classical in this respect, as they reach higher probabilities of target presence after a significantly lower number of experimental shots. A single idler detector heralded quantum source reaches a target present probability of 0.8 after $\sim 1.1\times10^4$ shots; two detectors $\sim 0.9\times10^4$; four detectors $\sim 0.88\times10^4$, whereas for the coherent state this is reached for 2.2×10^4 shots. In Figure. 5.16, the target absent scenario is also shown, obviously $p(H_1)\rightarrow 0$ in this instance. Although there is no requirement for symmetry around the 0.5 value the schemes appear to be equally as good at detecting a target when it is present as they are at ruling one out when it is absent.

5.4 Discussion

This chapter compared the theoretical predictions of quantum illumination with optimal detection vs. a non-optimal photon-counting based detection. In the optimal detection regime predicted solely through state discrimination, QI with entangled TMSV is shown to perform better compared to CI with coherent state, which models a single-mode laser operating at the quantum shot-noise limit. The performance is quantified by the error probability which tells us how fast the error probability decays given an exponential number of observation. To achieve this type of idealised measurement, optimal quantum receiver schemes and lossless idler mode storage are required. Two examples of quantum illumination receivers are proposed by ref. [32]: the OPA receiver and the phase-conjugate receiver, both can achieve 3dB error exponent gain using the parameters stated in Figure 5.7 and ref. [30] ($\bar{n}_B = 20, \kappa = 0.01$ and $\bar{n} = 0.01$). Both methods require ideal photocounting, amplification and simultaneous measurements.

In reality, detector imperfections would be impossible to avoid, therefore an analysis comparing CI and QI in the context of non-optimal measurement, is necessary. Hence on-off detection analysis from the previous Chapter 4 was incorporated into the illumination model as a final step. On-off measurement is a direct phase-insensitive measurement hence it can only access the photon number distribution of the state, which at times require discrete basis expansions in

analysis. Imperfections are modelled as thermal background noise and quantum efficiency, which are incorporated via a beamsplitter in front of a perfect on-off detector that couples the incoming field with a separate thermal mode modelling dark noise. The signal loss applied to the beamsplitter is similar in technique for calculation of the reflected signal in eqn. (5.5), except that reflectivity is modelled as transmissivity.

The results of this chapter show that the simultaneous measurement requirement is not strictly necessary in order to bring about the advantages from QI. Use of on-off detection enables a heralding-type measurement on the idler mode of TMSV to boost the energy of the signal mode. The increase in mean photon number is what provides the advantage in receiver click probability ergo the QI advantage. However in doing so, the quantum advantage is diminished as this is only suitable for boosting click probability in a low mean photon number regime, because the reflected coherent state signals will more likely cause the detector to fire for a higher mean photon number (the crossover points in Figures 5.9 and 5.11). This can be offset by relying on a higher number of multi-clicks to provide a greater boost to the mean photon number of the signal.

Lastly, a sequential detection process was outlined using the conditional probability of click results for CI and QI. As the conditional probabilities represent detection results for a single shot, a simulation of a multi-shot scenario was made by repeatedly updating a target present probability $p(H_1)$ using the posterior probabilities calculated after each shot. The click outcomes for both heralding and receiving detectors were selected at random via an inverse sampling method using the cumulative click distributions. Heralded states are generated, per shot, by this method also, to provide a completely fair comparison with the coherent state, in that a heralded state is used no matter what the outcome of the idler detection – even in this instance it was shown that QI can outperform CI.

Conclusions

Quantum illumination is an application of quantum radiation primarily for ranging and target detection applications. Despite experimental challenges, entanglement based protocols have shown that imaging with TMSV increases the SNR of the detection for low signal powers, even in noisy environments, compared to imaging with classical thermal states or coherent states of the same energy [39, 41]. No experiment so far has performed full microwave quantum illumination with optimal receivers that compare TMSV to coherent state illumination.

In this thesis I have investigated the theory of quantum illumination with Gaussian states and implemented a detection step into the general model. It has been shown by the results in Chapter. V, that QI using TMSV generates higher target detection probabilities, at low signal energy, compared with coherent state CI when measuring using on-off photodetectors – the results indicate the same level of target present probability is reached using QI in lesser number of shots compared to CI. Unlike simultaneous optimal detection, click detection of the idler mode heralds a gain in signal energy, due to the intensity correlations of TMSV, which ultimately contributes to the increase in receiver detector click probabilities. Using a multiplexed click detector setup allows larger gain to the signal mode if simultaneous click outcomes occur, however this cannot occur for every single entangled pulse of TMSV because heralding is a probabilistic process.

As mean signal energy increases, this relative gain diminishes compared to using a coherent state signal, due to predominance of the Poissonian photon number distribution of the coherent state, which more likely triggers a detection outcome compared to the thermal like photon number distribution of the TMSV. The statistics of the radiation matters to the detection results, because

for the same mean signal energy, two statistically different quantum states produce different results. QI produces better results at low signal energy whereas CI is better for higher signal energy. The statistics of the radiation states involved in the hypothesis testing process are modelled in continuous-variable formalism, which relates directly to the mean photon number and allows a fair comparison between states with different photon statistics. The target reflectivity has been modelled using a beamsplitter, which may be too simplistic as it only models specular reflection due to a flat plane.

A practical quantum radar is ultimately limited in range by the low power of the quantum signal. Another limiting factor is the relative low rates of TMSV production from down-conversion, which happens probabilistically. Nevertheless, potential applications remain likely in short-range applications in environments with high background noise, or well-established technology which benefits by assistance from quantum effects, rather than technology that is fully quantum. A fully efficient entangled source must be available in order to maximise the chances of enhanced signal gain through heralding.

Bibliography

[1] M. I. Skolnik, *Introduction to Radar Systems*, 2nd (McGraw-Hill Book Company, Singapore, 1981).

[2] S. Lloyd, "Enhanced Sensitivity of Photodetection via Quantum Illumination", Science **321**, 1463 (2008).

[3] V. Giovannetti, S. Lloyd, and L. Maccone, "Quantum-enhanced measurements: beating the standard quantum limit", **306**, 1330 (2004).

[4] M. A. Nielsen and I. L. Chuang, *Quantum Computation and Quantum Information*, 10th (Cambridge University Press, Cambridge, 2011).

[5] R. Horodecki, P. Horodecki, M. Horodecki, and K. Horodecki, "Quantum entanglement", Rev. Mod. Phys. **81**, 865 (2009).

[6] A. Einstein, B. Podolsky, and N. Rosen, "Can Quantum-Mechanical Description of Physical Reality Be Considered Complete?", Phys. Rev. **47**, 777 (1935).

[7] J. S. Bell, "On the Einstein Pololsky Rosen Paradox", Phys. Phys. Fiz. **1**, 195 (1964).

[8] C. H. Bennett and S. J. Wiesner, "Communication via One- and Two-Particle Operators on Einstein-Podolsky-Rosen States", Phys. Rev. Lett. **69**, 2881 (1992).

[9] T. Schaetz, M. D. Barrett, D. Leibfried, J. Chiaverini, J. Britton, W. M. Itano, J. D. Jost, C. Langer, and D. J. Wineland, "Quantum Dense Coding with Atomic Qubits", Phys. Rev. Lett. **93**, 1 (2004).

[10] C. H. Bennett, G. Brassard, C. Crépeau, R. Jozsa, A. Peres, and W. K. Wootters, "Teleporting an Unknown Quantum State via Dual Classical and Einstein-Podolsky-Rosen Channels", Phys. Rev. Lett. **70**, 1895 (1993).

[11] A. Furusawa, J. L. Sørensen, S. L. Braunstein, C. A. Fuchs, H. J. Kimble, and E. S. Polzik, "Unconditional Quantum Teleportation", Science **282**, 706 (1998).

[12] D. Bouwmeester, J. W. Pan, K. Mattle, M. Eibl, H. Weinfurter, and A. Zeilinger, "Experimental Quantum Teleportation", Nat. Phys. **390**, 575 (1997).

[13] D. Boschi, S. Branca, F. De Martini, L. Hardy, and S. Popescu, "Experimental Realization of Teleporting an Unknown Pure Quantum State via Dual Classical and Einstein-Podolsky-Rosen Channels", Phys. Rev. Lett. **80**, 1121 (1998).

[14] J. G. Ren, P. Xu, H. L. Yong, L. Zhang, S. K. Liao, J. Yin, W. Y. Liu, W. Q. Cai, M. Yang, L. Li, K. X. Yang, X. Han, Y. Q. Yao, J. Li, H. Y. Wu, S. Wan, L. Liu, D. Q. Liu, Y. W. Kuang, Z. P. He, P. Shang, C. Guo, R. H. Zheng, K. Tian, Z. C. Zhu, N. L. Liu, C. Y. Lu, R. Shu, Y. A. Chen, C. Z. Peng, J. Y. Wang, and J. W. Pan, "Ground-to-satellite quantum teleportation", Nature **549**, 70 (2017).

[15] C. K. Hong, Z. Y. Ou, and L. Mandel, "Measurement of Subpicosecond Time Intervals between Two Photons by Interference", Phys. Rev. Lett. **59**, 2044 (1987).

[16] P. Grangier, M. J. Potasek, and B. Yurke, "Probing the Phase Coherence of Parametrically Generated Photon Pairs: A New Test of Bell's Inequalities", Phys. Rev. A **38**, 3132 (1988).

[17] Z. Y. Ou, S. F. Pereira, H. J. Kimble, and K. C. Peng, "Realization of the Einstein-Podolsky-Rosen Paradox for Continuous Variables", Phys. Rev. Lett. **68**, 3663 (1992).

[18] D. Buono, G. Nocerino, V. D'Auria, A. Porzio, S. Olivares, and M. G. Paris, "Characterization of bipartite Gaussian states from OPO", J. Opt. Soc. Am. B **27**, 110 (2010).

[19] C. Emary, B. Trauzettel, and C. W. Beenakker, "Emission of Polarization-Entangled Microwave Photons from a Pair of Quantum Dots", Phys. Rev. Lett. **95**, 1 (2005).

[20] S. Dambach, B. Kubala, and J. Ankerhold, "Generating entangled quantum microwaves in a Josephson-photonics device", New J. Phys. **19**, 023027 (2017).

[21] L. Arndt and F. Hassler, "Statistics of radiation due to nondegenerate Josephson parametric down-conversion", Phys. Rev. B **100**, 1 (2019).

[22] S. M. Barnett and S. Croke, "Quantum state discrimination", Adv. At. Mol. Opt. Phys. **1**, 238 (2009).

[23] G. Grynberg, A. Aspect, C. Fabre, and C. Cohen-Tannoudji, *Introduction to Quantum Optics: From the Semi-classical Approach to Quantized Light* (Cambridge University Press, Cambridge, 2010).

[24] A. I. Lvovsky, "Squeezed Light", Photonics Sci. Found. Technol. Appl. **1**, 121 (2015).

[25] C. W. Chang, A. M. Vadiraj, J. Bourassa, B. Balaji, and C. M. Wilson, "Quantum-enhanced noise radar", Appl. Phys. Lett. **114**, 1 (2019).

[26] Z. Zhang, M. Tengner, T. Zhong, F. N. C. Wong, and J. H. Shapiro, "Entanglement's Benefit Survives an Entanglement-Breaking Channel", Phys. Rev. Lett. **111**, 010501 (2013).

[27] S. Frick, A. McMillan, and J. Rarity, "Quantum Rangefinding", Opt. Express **28**, 37118 (2020).

[28] M. F. Sacchi, "Optimal discrimination of quantum operations", Phys. Rev. A **71**, 1 (2005).

[29] S. Lloyd, "Supporting Online Material for Enhanced Sensitivity of Photodetection via Quantum Illumination", Science **321**, 1463 (2008).

[30] S. H. Tan, B. I. Erkmen, V. Giovannetti, S. Guha, S. Lloyd, L. Maccone, S. Pirandola, and J. H. Shapiro, "Quantum Illumination with Gaussian States", Phys. Rev. Lett. **101**, 253601 (2008).

[31] J. H. Shapiro and S. Lloyd, "Quantum illumination versus coherent-state target detection", New J. Phys. **11**, 063045 (2009).

[32] S. Guha and B. I. Erkmen, "Gaussian-state quantum-illumination receivers for target detection", Phys. Rev. A **80**, 1 (2009).

[33] Q. Zhuang, Z. Zhang, and J. H. Shapiro, "Entanglement-enhanced Neyman-Pearson target detection using quantum illumination", J. Opt. Soc. Am. B **34**, 1567 (2017).

[34] S. Barzanjeh, S. Guha, C. Weedbrook, D. Vitali, J. H. Shapiro, and S. Pirandola, "Microwave Quantum Illumination", Phys. Rev. Lett. **114**, 1 (2015).

[35] S. Bose, "Plancks Gesetz und Lichtquantenhypothese", Zeitschrift für Phys. **26**, 178 (1924).

[36] S. Barzanjeh, D. Vitali, P. Tombesi, and G. J. Milburn, "Entangling optical and microwave cavity modes by means of a nanomechanical resonator", Phys. Rev. A **84**, 1 (2011).

[37] T. A. Palomaki, J. D. Teufel, R. W. Simmonds, and K. W. Lehnert, "Entangling mechanical motion with microwave fields", Science **342**, 710 (2013).

[38] R. W. Andrews, R. W. Peterson, T. P. Purdy, K. Cicak, R. W. Simmonds, C. A. Regal, and K. W. Lehnert, "Bidirectional and efficient conversion between microwave and optical light", Nat. Phys. **10**, 321 (2014).

[39] E. D. Lopaeva, I. Ruo Berchera, I. P. Degiovanni, S. Olivares, G. Brida, and M. Genovese, "Experimental Realization of Quantum Illumination", Phys. Rev. Lett. **110**, 153603 (2013).

[40] Z. Zhang, S. Mouradian, F. N. Wong, and J. H. Shapiro, "Entanglement-Enhanced Sensing in a Lossy and Noisy Environment", Phys. Rev. Lett. **114**, 1 (2015).

[41] D. G. England, B. Balaji, and B. J. Sussman, "Quantum-enhanced standoff detection using correlated photon pairs", Phys. Rev. A **99**, 1 (2019).

[42] S. Barzanjeh, S. Pirandola, D. Vitali, and J. M. Fink, "Microwave quantum illumination using a digital receiver", Sci. Adv. **6**, 1 (2020).

[43] S. Pirandola, "Quantum Reading of a Classical Digital Memory", Phys. Rev. Lett. **106**, 1 (2011).

[44] W. Roga, D. Buono, and F. Illuminati, "Device-independent quantum reading and noise-assisted quantum transmitters", New J. Phys. **17**, 1 (2015).

[45] G. Ortolano, E. Losero, S. Pirandola, M. Genovese, and I. Ruo-Berchera, "Experimental quantum reading with photon counting", Sci. Adv. **7**, 1 (2021).

[46] C. Weedbrook, S. Pirandola, R. García-Patrón, N. J. Cerf, T. C. Ralph, J. H. Shapiro, and S. Lloyd, "Gaussian quantum information", Rev. Mod. Phys. **84**, 621 (2012).

[47] H. Yang, W. Roga, J. Pritchard, and J. Jeffers, "Quantum illumination with simple detection", Proc. SPIE 11347, Quantum Technol. **11347**, 11347I (2020).

[48] H. Yang, W. Roga, J. D. Pritchard, and J. Jeffers, "Gaussian state-based quantum illumination with simple photodetection", Opt. Express **29**, 8199 (2021).

[49] H. Yang, N. Samantaray, and J. Jeffers, "Quantum Illumination with Multiplexed Photodetection", Phys. Rev. Appl. **18**, 1 (2022).

[50] A. Cho, "The short, strange life of quantum radar", Science **369**, 1556 (2020).

[51] J. H. Shapiro, "The Quantum Illumination Story", IEEE Aerosp. Electron. Syst. Mag. **35**, 8 (2020).

[52] R. G. Torromé, N. B. Bekhti-Winkel, and P. Knott, "Introduction to quantum radar", arXiv (2020).

[53] G. Sorelli, N. Treps, F. Grosshans, and F. Boust, "Detecting a Target With Quantum Entanglement", IEEE Aerosp. Electron. Syst. Mag. **37**, 68 (2022).

[54] A. Einstein, "On a Heuristic Point of View about the Creation and Conversion of Light", Ann. Phys. **17**, 132 (1905).

[55] H. Kimble, M. Dagenais, and L. Mandel, *Phonon Antibouncing in Resonance Fluoresence*, 1977.

[56] A. S. Holevo, *Statistical Structure of Quantum Theory* (Springer Berlin, Heidelberg, 2001).

[57] P. A. M. Dirac, *The Principles of Quantum Mechanics*, 4th (Oxford University Press, Oxford, 1958).

[58] M. G. Paris, M. Cola, and R. Bonifacio, "Quantum-state engineering assisted by entanglement", Phys. Rev. A **67**, 10 (2003).

[59] A. Ferraro, S. Olivares, and M. G. A. Paris, *Gaussian states in continuous variable quantum information* (Bibliopolis, Napoli, Italy, 2005).

[60] T. J. Bartley, G. Donati, J. B. Spring, X. M. Jin, M. Barbieri, A. Datta, B. J. Smith, and I. A. Walmsley, "Multiphoton state engineering by heralded interference between single photons and coherent states", Phys. Rev. A **86**, 1 (2012).

[61] J. Sperling, W. Vogel, and G. S. Agarwal, "Quantum state engineering by click counting", Phys. Rev. A **89**, 043829 (2014).

[62] D. K. Cheng, *Field and Wave Electromagnetics*, 2nd (Pearson, London, 2013).

[63] J. E. Moyal, "Quantum mechanics as a statistical theory", Math. Proc. Cambridge Philos. Soc. **45**, 99 (1949).

[64] E. Wigner, "On the Quantum Correction for Thermodynamic Equilibrium", Phys. Rev. **40**, 749 (1932).

[65] S. L. Braunstein and P. Van Loock, "Quantum information with continuous variables", Rev. Mod. Phys. **77**, 513 (2005).

[66] A. Ferraro, L. Aolita, D. Cavalcanti, F. M. Cucchietti, and A. Acín, "Almost all quantum states have nonclassical correlations", Phys. Rev. A **81**, 1 (2010).

[67] G. Adesso, S. Ragy, and A. R. Lee, "Continuous variable quantum information: Gaussian states and beyond", Open Syst. Inf. Dyn. **21**, 1440001 (2014).

[68] A. Serafini, *Quantum Continuous Variables* (CRC Press, Boca Raton, 2017).

[69] R. Simon, E. C. G. Sudarshan, and N. Mukunda, "Gaussian-Wigner distributions in quantum mechanics and optics", Phys. Rev. A **36**, 3868 (1987).

[70] S. Barnett and P. Radmore, *Methods in Theoretical Quantum Optics*, 1st (Oxford University Press, Oxford, 1997).

[71] S. Gasiorowicz, *Quantum Physics*, 3rd (Wiley, Chichester, 2003).

[72] R. Loudon, *The Quantum Theory of Light*, 3rd (Oxford University Press, Oxford, 2000).

[73] W. P. Schleich, *Quantum Optics in Phase Space*, 1st (Wiley-VCH, Berlin, 2005).

[74] S. Pirandola and S. Lloyd, "Computable bounds for the discrimination of Gaussian states", Phys. Rev. A **78**, 1 (2008).

[75] R. J. Glauber, "Coherent and Incoherent States of the Radiation Field", Phys. Rev. **131**, 2766 (1963).

[76] G. Breitenbach, S. Schiller, and J. Mlynek, "Measurment of the Quantum States of Quantum States of Squeezed Light", Nat. Phys. **387**, 471 (1997).

[77] M. S. Kim, F. A. De Oliveira, and P. L. Knight, "Properties of squeezed number states and squeezed thermal states", Phys. Rev. A **40**, 2494 (1989).

[78] R. Loudon and P. L. Knight, "Squeezed light", J. Mod. Opt. **34**, 709 (1987).

[79] S. M. Barnett and P. L. Knight, "Squeezing in Correlated Quantum Systems", J. Mod. Opt. **34**, 841 (1987).

[80] G. Adesso and F. Illuminati, "Entanglement in continuous-variable systems: Recent advances and current perspectives", J. Phys. A Math. Theor. **40**, 7821 (2007).

[81] J. Eisert, S. Scheel, and M. B. Plenio, "Distilling Gaussian States with Gaussian Operations is Impossible", Phys. Rev. Lett. **89** (2002).

[82] A. K. Ekert and P. L. Knight, "Correlations and squeezing of two-mode oscillations", Am. J. Phys. **57**, 692 (1989).

[83] M. D. Reid, "Demonstration of the Einstein-Podolsky-Rosen paradox using nondegenerate parametric amplification", Phys. Rev. A **40**, 913 (1989).

[84] V. D'Auria, S. Fornaro, A. Porzio, S. Solimeno, S. Olivares, and M. G. Paris, "Full Characterization of Gaussian Bipartite Entangled States by a Single Homodyne Detector", Phys. Rev. Lett. **102**, 1 (2009).

[85] H. Kobayashi, B. L. Mark, and W. Turin, *Probability, Random Processes, and Statistical Analysis: Applications to Communications, Signal Processing, Queueing Theory and Mathematical Finance* (Cambridge University Press, Cambridge, 2011).

[86] A. Kenfack and K. Zyczkowski, "Negativity of the Wigner function as an indicator of non-classicality", J. Opt. B **6**, 396 (2004).

[87] A. I. Lvovsky, H. Hansen, T. Aichele, O. Benson, J. Mlynek, and S. Schiller, "Quantum State Reconstruction of the Single-Photon Fock State", Phys. Rev. Lett. **87**, 050402 (2001).

[88] M. S. Kim, E. Park, P. L. Knight, and H. Jeong, "Nonclassicality of a photon-subtracted Gaussian field", Phys. Rev. A **71**, 1 (2005).

[89] E. C. Sudarshan, "Equivalence of Semiclassical and Quantum Mechanical Descriptions of Statistical Light Beams", Phys. Rev. Lett. **10**, 277 (1963).

[90] K. Husimi, "Some Formal Properties of the Density Matrix", Proc. Phys. Math. Soc. Jpn. **22**, 264 (1940).

[91] Y. Kano, "A New Phase-Space Distribution Function in the Statistical Theory of the Electromagnetic Field", J. Math. Phys. **6**, 1913 (1965).

[92] L. Zhang, H. Coldenstrodt-Ronge, A. Datta, and I. A. Walmsley, *Quantum Detector Tomography*, Vol. 45 (Elsevier Inc., 2013), pp. 283–313.

[93] J. S. Lundeen, A. Feito, K. L. Pregnell, C. Silberhorn, and T. C. Ralph, "Tomography of quantum detectors", Nat. Phys. **5**, 27 (2008).

[94] A. Serafini, F. Illuminati, and S. De Siena, "Symplectic invariants, entropic measures and correlations of Gaussian states", J. Phys. B **37**, L21 (2004).

[95] J. Williamson, "On the Algebraic Problem Concerning the Normal Forms of Linear Dynamical Systems", Am. J. Math. **58**, 141 (1936).

[96] Arvind, B. Dutta, N. Mukunda, and R. Simon, "The real symplectic groups in quantum mechanics and optics", Pramana **45**, 471 (1995).

[97] K. Banaszek and K. Wódkiewicz, "Testing Quantum Nonlocality in Phase Space", Phys. Rev. Lett. **82**, 2009 (1999).

[98] A. Kuzmich, I. A. Walmsley, and L. Mandel, "Violation of Bell's Inequality by a Generalized Einstein-Podolsky-Rosen State Using Homodyne Detection", Phys. Rev. Lett. **85**, 1349 (2000).

[99] C. W. Helstrom, "Quantum detection and estimation theory", J. Stat. Phys. **1**, 231 (1969).

[100] R. Jozsa, "Fidelity for mixed quantum states", J. Mod. Opt. **41**, 2315 (1994).

[101] C. A. Fuchs and C. M. Caves, "Mathematical Techniques for Quantum Communication Theory", Open Syst. Inf. Dyn. **3**, 345 (1995).

[102] S. Pirandola, B. R. Bardhan, T. Gehring, C. Weedbrook, and S. Lloyd, "Advances in photonic quantum sensing", Nat. Photonics **12**, 724 (2018).

[103] A. R. Usha Devi and A. K. Rajagopal, "Quantum target detection using entangled photons", Phys. Rev. A **79**, 062320 (2009).

[104] H. L. Van Trees, *Detection, Estimation, and Modulation Theory, Part I* (2001).

[105] K. M. R. Audenaert, J. Calsamiglia, R. Munoz-Tapia, E. Bagan, L. Masanes, A. Acin, and F. Verstraete, "Discriminating States: The Quantum Chernoff Bound", Phys. Rev. Lett. **98**, 160501 (2007).

[106] C. A. Fuchs and J. V. D. Graaf, "Cryptographic Distinguishability Measures", IEEE Trans. Inf. Theory **45**, 1216 (1999).

[107] S. M. Barnett and E. Riis, "Experimental demonstration of polarization discrimination at the Helstrom bound", J. Mod. Opt. **44**, 1061 (1997).

[108] M. Sasaki and O. Hirota, "Two examples of measurement processes illustrating Helstrom's optimum decision bound", Phys. Lett. A **210**, 21 (1996).

[109] S. J. Dolinar, "An optimum receiver for the binary coherent state quantum channel", MIT Res. Lab. Electron. Q. Prog. Rep. **111**, 115 (1973).

[110] R. L. Cook, P. J. Martin, and J. M. Geremia, "Optical coherent state discrimination using a closed-loop quantum measurement", Nature **446**, 774 (2007).

[111] A. Uhlmann, "The "Transition Probability" in the State Space of A *-Algebra", Reports Math. Phys. **9** (1976).

[112] K. M. Audenaert, M. Nussbaum, A. Szkoła, and F. Verstraete, "Asymptotic error rates in quantum hypothesis testing", Commun. Math. Phys. **279**, 251 (2008).

[113] J. Calsamiglia, R. Munoz-Tapia, L. Masanes, A. Acin, and E. Bagan, "Quantum Chernoff bound as a measure of distinguishability between density matrices: Application to qubit and Gaussian states", Phys. Rev. A **77**, 1 (2008).

[114] H. Chernoff, "A Measure of Asymptotic Efficiency for Tests of a Hypothesis Based on the sum of Observations", Ann. Math. Stat. **23**, 493 (1952).

[115] P. Marian and T. A. Marian, "Uhlmann fidelity between two-mode Gaussian states", Phys. Rev. A **86**, 022340 (2012).

[116] L. Banchi, S. L. Braunstein, and S. Pirandola, "Quantum Fidelity for Arbitrary Gaussian States", Phys. Rev. Lett. **115**, 1 (2015).

[117] M. J. Stevens, *Photon Statistics, Measurements, and Measurements Tools*, Vol. 45 (Elsevier Inc., 2013), pp. 25–68.

[118] U. Leonhardt, M. Munroe, T. Kiss, T. Richter, and M. G. Raymer, "Sampling of photon statistics and density matrix using homodyne detection", Opt. Commun. **127**, 144 (1996).

[119] M. J. Collett, R. Loudon, and C. W. Gardiner, "Quantum theory of optical homodyne and heterodyne detection", J. Mod. Opt. **34**, 881 (1987).

[120] A. I. Lvovsky and M. G. Raymer, "Continuous-variable optical quantum-state tomography", Rev. Mod. Phys. **81**, 299 (2009).

[121] D. Achilles, C. Silberhorn, C. Sliwa, K. Banaszek, A. Walmsley, M. J. Fitch, B. C. Jacobs, T. B. Pittman, D. James, D. Achilles, C. Silberhorn, C. Sliwa, and K. Banaszek, "Photon-number-resolving detection using time-multiplexing", J. Mod. Opt. **51**, 1499 (2004).

[122] G. Brida, M. Genovese, M. Gramegna, A. Meda, F. Piacentini, P. Traina, E. Predazzi, S. Olivares, and M. G. Paris, "Quantum state reconstruction using binary data from on/off photodetection", Adv. Sci. Lett. **4**, 1 (2011).

[123] J. Sperling and W. Vogel, "True photocounting statistics of multiple on-off detectors", Phys. Rev. A **85**, 023820 (2012).

[124] L. Mandel and E. Wolf, "Coherence properties of optical fields", Rev. Mod. Phys. **37**, 231 (1965).

[125] P. L. Kelley and W. H. Kleiner, "Theory of Electromagnetic Field Measurement and Photoelectron", Phys. Rev. **136** (1964).

[126] P. P. Rohde and T. C. Ralph, "Modelling photo-detectors in quantum optics", J. Mod. Opt. **53**, 1589 (2006).

[127] U. Leonhardt, *Essential Quantum Optics: From Quantum Measurements to Black Holes* (Cambridge University Press, Cambridge, 2010).

[128] S. H. Tan, "Quantum State Discrimination with Bosonic Channels and Gaussian States", PhD thesis (MIT, 2010).

[129] F. A. De Oliveira, M. S. Kim, P. L. Knight, and V. Bužek, "Properties of displaced number states", Phys. Rev. A **41** (1990).

[130] G. Fishman, *Monte Carlo: concepts, algorithms, and applications* (Springer New York, New York, 2013).

[131] C. J. Clopper and E. S. Pearson, "The Use of Confidence or Fiducial Limits Illustrated in the Case of the Binomial", Biometrika **26**, 404 (1934).

[132] M. Thulin, "The cost of using exact confidence intervals for a binomial proportion", Electron. J. Stat. **8**, 817 (2014).

[133] N. L. Johnson, S. Kotz, and N. Balakrishnan, *Continuous univariate distributions, volume 2*, 2nd, Vol. 289 (John Wiley & Sons, 1995).